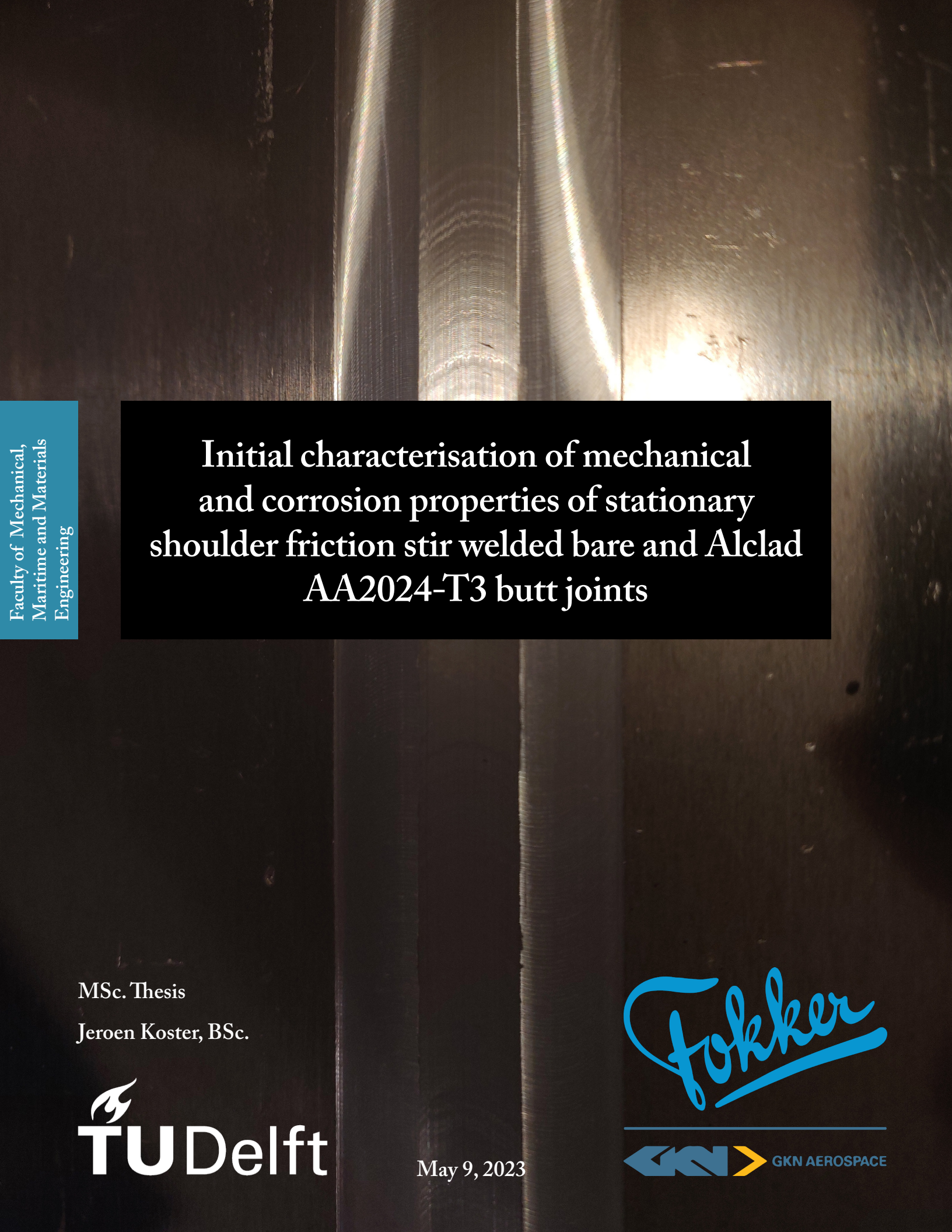

Initial characterisation of mechanical and corrosion properties of stationary shoulder friction stir welded bare and Alclad AA2024-T3 butt joints

Faculty of Mechanical, Maritime and Materials Engineering

MSc. Thesis

Jeroen Koster, BSc.

TU Delft

May 9, 2023

Fokker

GKN AEROSPACE

Initial characterisation of mechanical and corrosion properties of stationary shoulder friction stir welded bare and Alclad AA2024-T3 butt joints

MSc. Thesis

by

Jeroen Koster

in partial fulfilment of the requirements for the degree of

Master of Science

in Materials Science and Engineering

at the Delft University of Technology

to be defended publicly on Monday, 15 May 2023, at 13:00

Student number:	4135318	
Project duration:	April 19, 2021 – May 15, 2023	
Daily supervisor:	Dr. D. Danciu,	GKN Fokker Aerostructures
Thesis committee:	Prof. dr. J. M. C. Mol,	TU Delft, chair
	Dr. V. A. Popovich,	TU Delft
	Dr. P. Taheri,	TU Delft
	Dr. A. J. Den Bakker,	GKN Fokker Aerostructures

ABSTRACT

Aluminium alloy AA2024-T3 is a lightweight and damage tolerant material, and is therefore often used in aerospace applications. However, this alloy is difficult to weld using conventional fusion welding techniques due to defects caused by the meld pool.

Friction stir welding (FSW) was developed by The Welding Institute (TWI) in 1991 in order to overcome welding difficulties associated with the conventional fusion welding of difficult to fusion weld materials such as AA2024-T3. Since then, efforts have been made to improve the process parameters. One such improvement was the development of a stationary shoulder tool, which reduces heat input by 30% and enables stronger welds with smaller heat affected zones (HAZ). However, since AA2024-T3 is susceptible to pitting corrosion, intergranular corrosion (IGC) and stress corrosion cracking (SCC), the welds need to be protected in order for any product to function in the long term. AA1050 is an often applied clad layer, which acts as a sacrificial anode with respect to the cathodic substrate. The microstructure and corresponding corrosion mechanisms are known for unwelded and FSW'd AA2024-T3, however, little research exists on the corrosion behaviour of stationary shoulder friction stir welded (SSFSW'd) bare and Alclad AA2024-T3 butt welds. Therefore, the main focus of this project is to investigate the mechanical and corrosion properties of SSFSW'd bare and Alclad AA2024-T3. This was done by performing optical microscopy, microhardness tests, open circuit potential measurements, linear polarisation resistance tests and potentiodynamic polarisation tests on the cross-sections of three type of weld configurations and thicknesses: 1.6 mm bare, 1.6 mm Alclad and 3.2 mm Alclad AA2024-T3 sheets. Simultaneously, tensile tests and immersion tests were also performed using dedicated tensile test and immersion specimens.

Analysis shows that the 1.6 mm bare weld is the strongest weld but also the most susceptible to pitting corrosion, compared to the Alclad welds. Cladding provides sufficient corrosion protection, even to an exposed section of the weld and when mixed into the weld. However, cladding lowers the tensile strength overall, and cladding mixed into the weld reduces the ductility of the weld compared to the bare weld. Furthermore, possible material flow issues at the root of the Alclad welds may cause voids, which lowers ductility and enables pitting at these locations. Nevertheless, even though specimens were immersed in 3.5% NaCl solution for 24 hours and small to severe pitting was visible on the specimens, the ultimate tensile strength was not affected compared to uncorroded weld specimens. However, a reduction of the maximum elongation of the bare specimen was observed after immersion. Similar to conventional FSW, the HAZ/TMAZ was the most susceptible to corrosion, due to the most active corrosion potential at this zone. Based on literature, this was deemed to be due the formation of S-phase precipitates along the grain boundaries in this zone. In all, stationary shoulder friction stir welded bare AA2024-T3 provide the best welds regarding mechanical properties, and should be protected against corrosion after welding instead of using preclad sheets, to avoid issues with the macrostructure and corresponding mechanical properties.

Keywords Microstructure · Corrosion behaviour · Friction stir welding · Stationary shoulder · AA2024-T3 · Cladding · Accelerated corrosion testing · Pitting · Intergranular corrosion · Aerospace applications

Contents

Nomenclature

Glossary

θ-phase	Secondary phase in AA2024-T3, hardening precipitate with Al_2Cu stoichiometry
AA2024-T3	Aluminum Association 2024 aluminium alloy in T3 temper
Centre	Mid-thickness of a weld cross-section
Face	The exposed surface of a weld on the side from which welding was done
Flash	Raised material on the edges of the weld face caused by the tool shoulder
Pit	Surface defect caused by local corrosion. Also called corrosion pit
Root	The interface of the weld and base metal at the "bottom" of the weld, opposite the face
S-phase	Secondary phase in AA2024-T3, hardening precipitate with Al_2CuMg stoichiometry
Void	Weld defect caused by insufficient heating during welding

Abbreviations

AS	Advancing Side (where the rotational motion and linear motion of the pin are in the same direction)
BM	Base Material (unwelded or parent material)
CF	Corrosion Fatigue
DSC	Differential Scanning Calorimetry
EDS/EDX	Energy-Dispersive X-ray Spectroscopy
EIS	Electrochemical Impedance Spectroscopy
EXCO	Exfoliation Corrosion
FSW/FSW'd	Friction Stir Welding/Friction Stir Welded
GP	Guinier-Preston zone (cluster of aluminium and copper atoms)
GPB	Guinier-Preston-Bagaryatsky zone (cluster of aluminium, copper and magnesium atoms)
HAZ	Heat Affected Zone
IGC	Intergranular Corrosion
IMP/IMPs	Intermetallic Particle/Intermetallic Particles
LPR	Linear Polarisation Resistance (see also R_p)
LT	Long Transverse (direction perpendicular to rolling direction)
NZ	Nugget Zone (recrystallised zone in the centre of a weld, see also SZ)
OCP	Open Circuit Potential (see also E_{ocp})
OM	Optical Microscopy
RS	Retreating Side (where the rotational motion and linear motion of the pin are in opposite directions)
SCC	Stress Corrosion Cracking

SCE	Saturated Calomel Electrode
SD	Standard Deviation
SEM	Scanning Electron Microscopy
SSFSW/SSFSW'D	Stationary Shoulder Friction Stir Welding/Stationary Shoulder Friction Stir Welded
SSSS	Supersaturated Solid Solution
ST	Short Transverse (through-thickness direction)
SZ	Stir Zone (recrystallised zone in the centre of a weld, see also NZ)
TEM	Transmission Electron Microscopy
TMAZ	Thermo-Mechanically Affected Zone
TWI	The Welding Institute
WLI	White Light Interferometry

List of symbols

E_{corr}	Corrosion potential	mV
E_{ocp}	Open circuit potential (see also OCP)	mV
E_{pit}	Pitting potential	mV
el	elongation	$\%$
i_{corr}	Corrosion current density	$\mu A/cm^2$
R_p	Polarisation resistance	$\Omega \cdot cm^2$
Sa	Arithmetic mean roughness	μm
Sku	Area texture kurtosis	-
Sp	Maximum peak height	μm
Ssk	Skewness	-
Sv	Maximum valley depth	μm
UTS	Ultimate Tensile Strength	MPa

1 Introduction

In 2021, GKN Aerospace made 2.6 billion GBP (3.1 billion USD) in sales [1], which is 1% of the global aerospace market [2]. With an estimated global fleet of 24 thousand aircraft in 2021 [3], the need for strong and lightweight materials is as high as ever. Since aluminium is a lightweight metal and commonly available in the Earth's crust [4], it has been used in the aerospace industry since the early 1920s [5]. However, pure aluminium lacks the damage tolerance and strength that are needed in lower wing skins and fuselage structures of commercial aircraft [5]. Instead, aluminium alloys such as AA2024-T3 are used, which contain alloying elements such as copper and magnesium, which increase the mechanical properties due to the precipitates they form in the aluminium matrix [6].

However, this alloy is difficult to weld using conventional fusion welding techniques, such as metal inert gas (MIG) and Tungsten inert gas (TIG) welding, due to loss of volatile elements, porosity, hot cracking and other defects caused by the melt pool [7]–[10]. To enable the welding of materials that are difficult to fusion weld, The Welding Institute (TWI) developed a solid state weld technique called friction stir welding (FSW) in 1991 [11]. FSW is a process in which a hard tool consisting of a pin and shoulder is rotated at high speed and plunged into the sheets, traversing along the weld line, heating (but not melting) and plastically deforming the material along the way, resulting in a clean weld. Unfortunately, this weld has lower mechanical properties than the base material itself, due to a weaker thermo-mechanically affected zone (TMAZ) and a large heat-affected zone (HAZ) [12]. TWI has been improving the FSW process, resulting in a newly developed stationary shoulder friction stir welding (SSFSW) process [13]. In SSFSW, the shoulder no longer rotates, resulting in a smaller HAZ and TMAZ, and therefore improving mechanical properties with respect to conventional FSW [14].

Next to being difficult to weld, AA2024-T3 is very susceptible to corrosion phenomena such as pitting, intergranular corrosion (IGC) and stress corrosion cracking (SCC) due to the local galvanic coupling of intermetallic particles (IMPs) with the aluminium matrix [15]–[26]. Friction stir welded (FSW'd) AA2024-T3 becomes even more susceptible to corrosion, due to the formation of continuous lines of s-phase precipitates along grain boundaries in the HAZ, which enhances the possibility for IGC to occur [27]–[32]. In general, several methods are available to protect AA2024-T3 from corrosion, including (sol-gel) coatings, inhibitors, paints, films, and cathodic protection methods [33], [34]. Such a cathodic protection method in the aerospace industry is the application of Alclad (usually 1050 alloy) on both sides of the alloy; the clad layer acts as a sacrificial anode, which corrodes first instead of the cathodic substrate [35], [36]. However, when friction stir welding Alclad AA2024-T3 sheets, the cladding disturbs the material flow and lowers the mechanical properties of the weld [37].

For SSFSW'd AA2024-T3 butt welds, the effect of cladding on the material flow during welding and the effect of a smaller HAZ and TMAZ on the corrosion behaviour are not well researched. This thesis aims to provide insight in the microstructure and corresponding tensile and corrosion behaviour of such welds.

To gain a better understanding of the involved topics in this project, a literature review has been performed, which is elaborated in chapter 2. Based on the research objectives determined at the end of that chapter, a research project has been set up, following the methods described in chapter 3, using the materials mentioned in the same chapter. The resulting findings are presented in chapter 4 and then discussed in the next chapter, leading to a conclusion in chapter 6. Possible recommendations for future projects are then given in the final chapter.

2 Literature review

2.1 Aluminium alloy AA2024-T3

Friedrich Wöhler was the first to produce pure aluminium in 1827, after Sir Humphrey Davy discovered metallic aluminium in 1809 [36]. Then, in 1909, Alfrid Wilm published his findings on the discovery of a stronger, lightweight aluminium alloy which he called Duralumin (Al-3.5Cu-0.5Mg-0.5Mn) [38], [39]. The process of making Duralumin lead to the discovery of precipitation hardening, enabling the creation of new alloying systems such as the 2xxx aluminium alloys [4]. The heat-treatable (age hardenable) wrought alloys in the 2xxx series are a mix of aluminium, copper, magnesium and other minor alloying elements, which increase the mechanical properties by precipitation hardening [36], [40]. Due to their high strength-to-weight ratio and high damage tolerance, the 2xxx aluminium alloys are commonly used in aerospace applications [24], [41].

2.1.1 From Bauxite to AA2024-T3

After extracting alumina (Al_2O_3) from Bauxite using the Bayer process, the alumina is then reduced to pure aluminium using solid Carbon (C) in an electrolytic process called the Hall-Heroult process [42]:

$$2\,Al_2O_3\,(aq)\;+\;3\,C\,(s)\;=\;4\,Al\,(l)\;+\;3\,CO_2\,(g) \tag{1}$$

The pure aluminium is then cast in a direct chill casting process, in which alloying elements are added to the molten aluminium to form an ingot of the desired alloy [43]. To produce AA2024, the composition shown in Table 1 is applied as each element is added to the molten metal, either in pure form or as a master alloy. Extra care is taken to ensure no hydrogen gas is entrapped in the molten metal, since this leads to porosity in the cast ingot. Next, sheet products are then hot-rolled from these ingots, with or without Alclad co-rolled onto them. Hot rolling combined with cold working results in a directional elongated grain structure, as shown in Figure 1, which is parallel to the rolling direction (L). The short transverse (ST) direction is the through-thickness direction[1] and the long transverse (LT) direction is perpendicular to L and ST.

Table 1: *Registered composition of relevant aluminium alloys in weight percent (wt.%), with aluminium as the remainder (Rem.) or minimum value. Entries with a range of values show minima and maxima, single values show a maximum.*

Alloy	Cu	Mg	Mn	Si	Fe	Zn	Cr	Ti	Al	Ref.
1050	0.05	0.05	0.05	0.25	0.40	0.05	-	0.03	99.50	[44]
2014	3.9-5.0	0.20-0.8	0.40-1.2	0.50-1.2	0.7	0.25	0.10	0.15	Rem.	[44], [45]
2024	3.8-4.9	1.2-1.8	0.30-0.9	0.50	0.50	0.25	0.10	0.15	Rem.	[44], [45]
2524	4.0-4.5	1.2-1.6	0.45-0.7	0.06	0.12	0.15	0.05	0.10	Rem.	[44]

[1] The short transverse direction is the most susceptible to corrosion, according to Campbell [35].

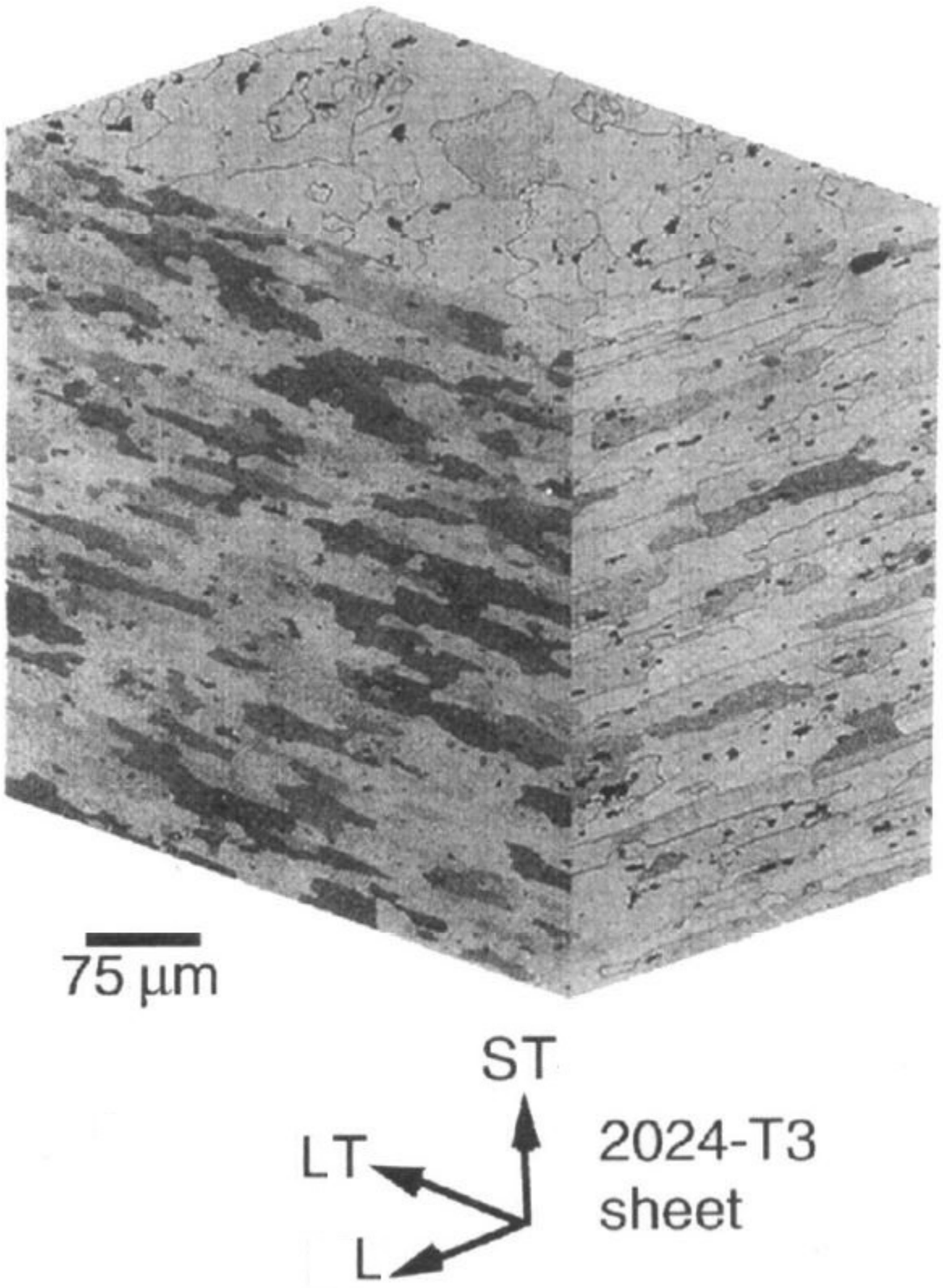

Figure 1: *3D composition of optical micrographs showing the microstructure of hot-rolled AA2024-T3 in longitudinal (L), long transverse (LT) and short transverse (ST) directions. The rolling plane is defined by the L and LT directions. Image adjusted from Buchheit, Grant, Hlava,* et al. *[46].*

After hot-rolling the thin sheet of AA2024, a heat treatment is applied to produce the desired mechanical properties. A selection of treatments is available, which are indicated with the following letters [47]:

- F: As fabricated - No special heat treatment or strain hardening are applied to these products. There are no boundaries set for the mechanical properties for this designation.
- O: Annealed - Annealing lowers the strength and increases the ductility of these products.
- H: Strain hardened - Desired mechanical properties are locked by cold working these products after hot forming or annealing.
- W: Solution heat-treated - These products usually are spontaneous naturally aged after being solution heat-treated and quenched, resulting in an unstable temper.
- T: Thermally treated - Products are first solution heat treated and quenched, then either strain hardened or not, and can be either naturally or artificially aged, which results in a stable temper.

The digits after the letter of the temper indicate the specific treatment steps taken. For AA2024 in T3 temper, the hot-rolled sheet is first solution heat treated at ∼493 °C for a few minutes [35], [48], [49], which enables alloying elements to diffuse into the aluminium matrix as a solid solution. The sheet is then rapidly cooled (quenched) in water at room temperature, which locks the alloying elements in a supersaturated solid solution (SSSS). Next, the sheet is then formed into shape by strain hardening (cold working), which increases the strength but decreases the ductility. Finally, the alloy is naturally aged at room temperature for 4 to 5 days, which results in the precipitation hardening of phases such as Al_2Cu (θ-phase) and Al_2CuMg (S-phase) from the SSSS [35], [36].

2.1.2 Precipitation, phases and microstructural features

To fully understand the complex microstructure of AA2024-T3, it is necessary to have an understanding of the formation of phases and precipitates during casting and heat treatment. However, the full microstructural evolution is out of scope for this project, therefore the reader is directed to relevant literature including the complex phase diagram of the AA2024 alloying system [50]–[58].

In short, secondary phase particles[2] consisting of intermetallic compounds, called intermetallic particles (IMPs), such as coarse constituent and impurity particles (>0.5 μm), dispersoids (100-500 nm) and hardening precipitates (<200 nm) form during different stages in the casting and subsequent heat treatment process [59]–[61]. During primary ingot production, coarse constituents, impurity particles and dispersoids form, which are sheared during hot-rolling but are mostly insoluble. Small hardening precipitates form during heat treatment from coherent clusters of particles, which are either called Guinier-Preston (GP) zones for Al-Cu clusters or Guinier-Preston-Bagaryatsky (GPB) zones for Al-Cu-Mg clusters. Their precipitation sequence follows from metastable coherent particles (") to stable incoherent particles (no prime) and is shown below [18], [40], [59], [60], [62]:

$$SSSS \rightarrow GP\ zone \rightarrow \theta\text{"} \rightarrow \theta' \rightarrow \theta$$
$$\rightarrow GPB\ zone \rightarrow S\text{"} \rightarrow S' \rightarrow S$$

[2] Secondary phase particles are distributed in the first phase, which is the Al-matrix in case of AA2024-T3.

The exact stoichiometry and existence of some of these secondary phase particles is debated in literature [59], however it is certain that at least hardening precipitates such as θ-phase (Al_2Cu) and S-phase (Al_2CuMg) are present in the microstructure of AA2024-T3 [16], [46], [50], [59], [63], [64]. A major dispersoid found in several studies is $Al_{20}Mn_3Cu_2$ (or $Al_{20}Cu_2Mn_3$) [50], [64]–[66], but does not exist in dispersoid-free areas around S-phase particles due to copper depletion [46]. Boag, Hughes, Wilson, *et al.* [67] showed that IMPs can consist of multiple phases, as shown in Figure 2. The existence of multiphase particles was also confirmed by Staszczyk, Sawicki, and Adamczyk-Cieslak [68]. The latter authors showed in the same paper that the formation of impurity particles depends on the amount of Si and Fe in the alloy composition, and that with higher Si and Fe content the formation of θ-phase and S-phase particles is reduced [68]. Fortunately, newer alloys contain less amounts of Si and Fe and therefore contain fewer impurity particles, improving the mechanical properties [69], [70]. Other phases mentioned in literature ([61], [67], [69], [71]) are left out of this review, since these phases are heavily debated and are varying largely per alloy composition [59]. Finally, these secondary phase particles are distributed in the aluminium matrix and form the complex microstructure of AA2024-T3 together with the grain structure. Figure 1 and Figure 2 show the distribution of grains and IMPs in AA2024-T3, respectively.

2.1.3 Mechanical properties

The distribution of hardening precipitates and grain boundaries provides strength and damage tolerance in AA2024-T3, since these precipitates and grain boundaries obstruct dislocations' movement [35]. AA2024-T3 is significantly stronger than pure aluminium, but lacks ductility, as is evident in Table 2. Other mechanical properties of AA2024-T3 are an elastic modulus of 72.4 GPa in tension, 28.0 GPa in shear and 73.8 GPa in compression [48], and a (K_{IC}) fracture toughness of 37 MPa$\sqrt{m}$ (for T351 temper) [72].

Table 2: *Some typical mechanical properties of pure aluminium, AA1050 alloy, and bare and Alclad AA2024-T3 sheet. Minimum mechanical properties for bare and Alclad AA2024-T3 are presented as well.*

Product	Tensile strength (MPa)	Yield strength (0.2% offset) (MPa)	Elongation (%)	Hardness (HB)	Shear strength (MPa)	Fatigue strength (MPa)	Ref.
99.99% Al	45	10	50	-	-	-	[50]
AA1050	76	28	39	-	62	-	[48]
Bare T3 sheet[a]	483	345	17	120	285	140	[48], [50]
Alclad T3 sheet[a]	450	310	18	-	275	-	[48], [50]
Bare T3[b]	435	290	10	-	-	-	[45]
Alclad T3[b]	400	270	10	-	-	-	[45]

[a] Values taken at 24°Celsius.

[b] Minimum values.

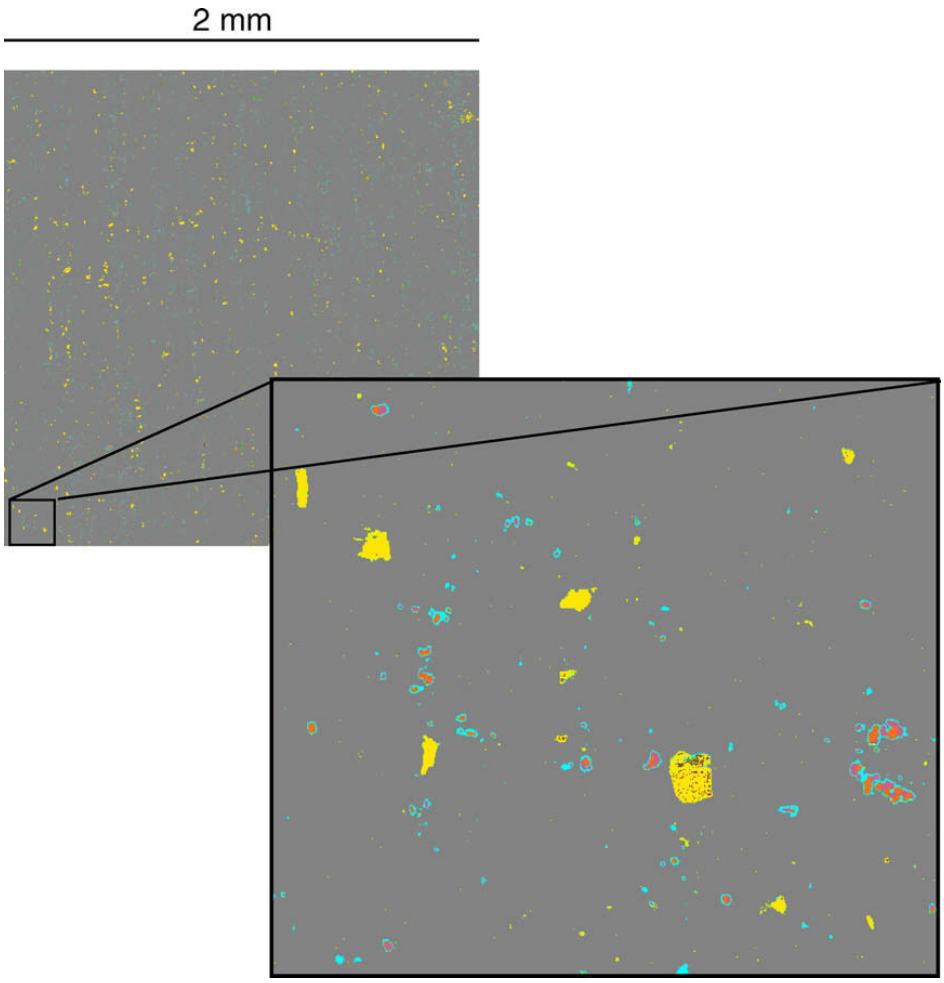

(a)

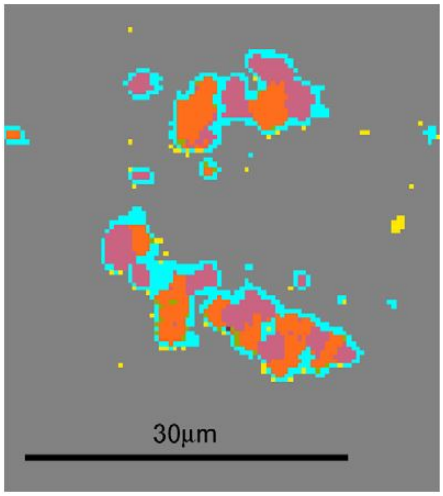

(b)

Figure 2: *Distribution of intermetallic particles (IMPs) in the Al-matrix (grey) found in AA2024-T3, image after Boag, Hughes, Wilson,* et al. *[67]. (a) Section of the 2x2 mm^2 polished surface with zoomed in section. (b) Multiphase IMPs of S-phase (pink) and θ-phase (orange), surrounded by a dispersoid-free area (cyan).*

2.2 Friction stir welding

2.2.1 Introduction to FSW

Friction stir welding (FSW) is the art of solid state welding using rotational friction [11], which means there is no melt pool and thus no phase transition from solid to liquid, although solid to solid phase changes can still occur. This is achieved by forcing a fast rotating tool into the sheets and traversing this tool across the weld-line, as shown in Figure 3 and Figure 4, which creates heat and plastic deformation and forces the material to flow.

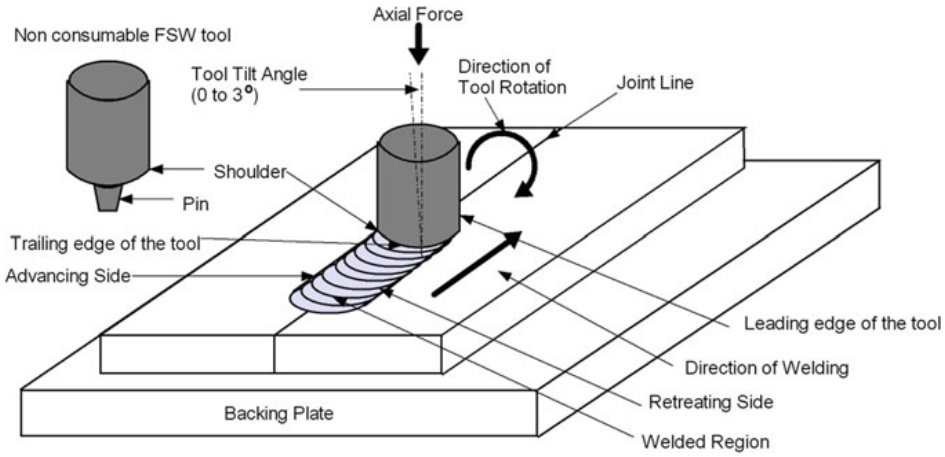

Figure 3: *Schematic showing the setup and some terminology in friction stir welding (FSW). Image after Shettigar and Manjaiah [73].*

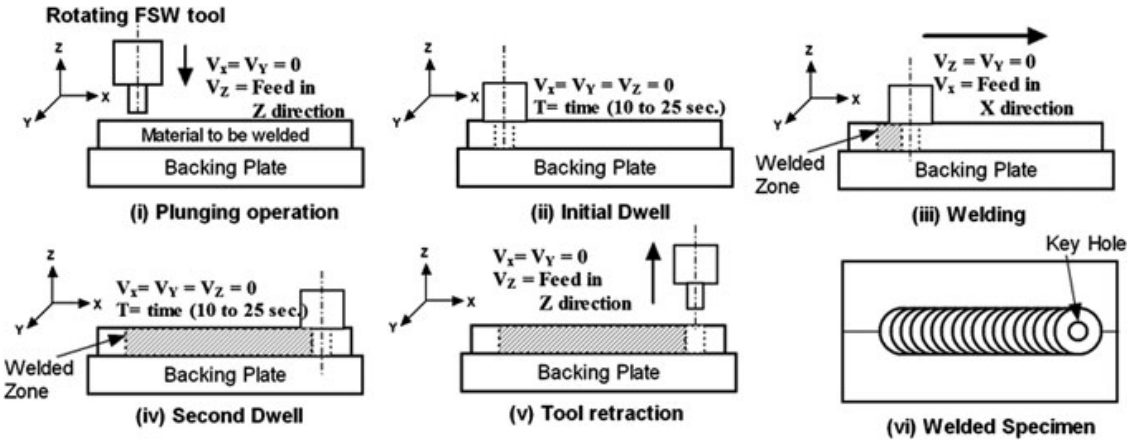

Figure 4: *Schematic showing the process of FSW in six steps. Image after Shettigar and Manjaiah [73].*

The process parameters greatly influence the weld microstructure and corresponding weld zones, therefore it is important to know what these parameters are [40], [41], [73]–[75]: The shoulder diameter, pin diameter and the ratio between these two influence the size of the weld, whereas the pin length is important for weld penetration. The tool is loaded with an axial force and set under a specific tilt angle to make sure the pin penetrates the material properly. The tool rotation speed generates the frictional heat leading to softening of the adjacent material and stirring of the grains of

the two sheets. Next, the welding speed (tool traverse speed) determines the rate at which new material flows into the stirring zone. Finally, the shape and material of the tool are of influence as well [74].

The stirring and travelling motion of the tool along the adjacent edges of the two sheets displaces the material such that a specific type of weld microstructure is created. A typical shape for a butt weld is shown in Figure 5, in which "A" shows the base material (BM), "B" shows the heat affected zone (HAZ), "C" shows the thermo-mechanically affected zone (TMAZ) and "D" shows the nugget zone (NZ). Shettigar and Manjaiah [73], El-Sayed, Shash, Abd-Rabou, *et al.* [76], and Braga, Eslami, and Moreira [77] describe each zone as follows: The BM is the original unwelded material and as such has not experienced a heat cycle nor plastic deformation during welding. In case the same material is used for both sheets, the BM should have similar microstructure in the retreating side (RS) and advancing side (AS) of the weld. The HAZ is affected by a small thermal cycle (up to 250 °C), but not by plastic deformation. This results in either peak-ageing of initially under-aged hardening precipitates or in over-ageing of initially peak-aged hardening precipitates. The over-ageing of the hardening precipitates lowers strength and microhardness, whereas peak-ageing increases the strength and microhardness. Next, the TMAZ experiences some plastic deformation and higher temperatures than the HAZ, due to the rotation and translation of the shoulder. This shears grains, dissolves hardening precipitates near the NZ and coarsens hardening precipitates near the HAZ. However, the grains do not recrystallise due to insufficient deformation strain and temperature, but are elongated and rotated upwards towards the NZ due to the shearing. The dissolving and over-ageing of hardening precipitates leads to even worse mechanical properties than the HAZ. Finally, the NZ experiences the most plastic deformation and the highest heat cycle (up to the solution treatment temperature of 493 °C), due to the material being displaced by the pin. This leads to recrystallisation of grains, which increases the mechanical properties slightly with respect to the TMAZ. A general schematic of the resulting hardness profile across the weld correlated to the microstructural features in 2xxx aluminium alloys with T3 temper is shown in Figure 6.

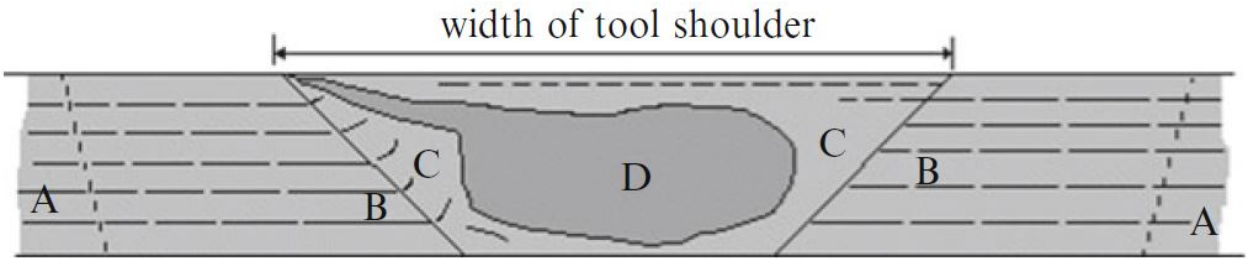

Figure 5: *Schematic representation of a long transverse cross-section of a friction stir welded butt joint as proposed by TWI. "A" shows the base material (BM), "B" shows the heat affected zone (HAZ), "C" shows the thermo-mechanically affected zone (TMAZ) and "D" shows the nugget zone (NZ). Image after Mishra, De, and Kumar [78].*

Models have been developed over the last three decades to optimise the welding parameters in order to decrease the occurrence of defects (such as flash, voids and kissing bonds) and improve the weld microstructure, therefore increasing the mechanical properties of the weld [8], [30], [79]–[88]. However, the discussion of these models is out of scope for this project and will therefore not be included here. Finally, several advantages are achieved over conventional fusion welding techniques with this process, such as: stronger welds are achievable due to the lack of loss of alloying elements; a lower heat input results in less shrinkage, distortion and porosity; the lack of filler material eliminates defects such as slag inclusions; and the ability to weld dissimilar and difficult to fusion weld materials more easily [8], [73], [74],

[77], [78]. However, some disadvantages exist as well, such as the need for rigid clamping of the work pieces and the existence of a keyhole at the end of each weld. Also, high melting point and high strength materials are difficult to weld using FSW, and powerful machines and specials tools are needed to join thick plates [8], [73], [74], [77], [78].

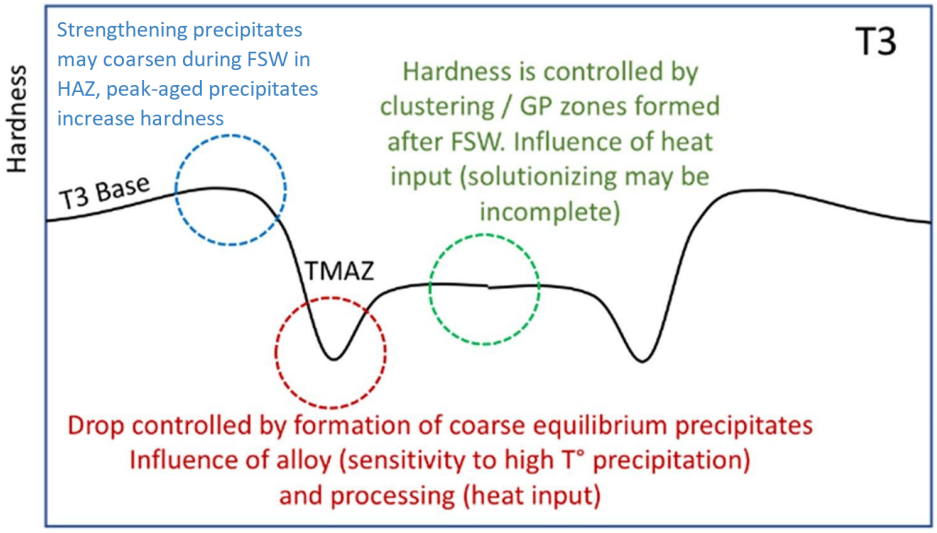

Figure 6: *A general schematic showing the correlation between microstructure and hardness properties across a friction stir weld, common for 2xxx alloys in T3 temper. The centre of the image is the weld centre (the NZ). Image adjusted from Heidarzadeh, Mironov, Kaibyshev,* et al. *[89].*

2.2.2 Microstructure and mechanical properties of FSW'd AA2024-T3

Several authors including Jones, Heurtier, Desrayaud, *et al.* [12], Bousquet, Poulon-Quintin, Puiggali, *et al.* [32], Jacquin and Guillemot [82], Legrand [90], and Li, Xu, Li, *et al.* [91], relate the mechanical properties of FSW'd AA2024 to the local weld microstructure. An understanding of the earlier generally described microstructural evolution is therefore of importance. Bousquet, Poulon-Quintin, Puiggali, *et al.* [32] observed grain length of 100 ± 20 μm in LT-direction and 30 ± 10 μm in ST-direction in the BM and HAZ of AA2024-T3, whereas grains in the TMAZ were of similar size but rotated in ST-direction due to plastic deformation. Legrand [90] reports an average grain diameter of 26 μm for the BM and 2 μm for the NZ. A high concentration of coherent Guinier-Preston-Bagaryatsky (GPB) zones is present in the BM, which inhibits the motion of dislocations, resulting in a microhardness of 135-144 HV [12], [32]. Some of these GPB zones are dissolved in the HAZ near the BM, decreasing the microhardness to $\sim$120 HV. However, in the centre of the HAZ an increase of fine S-phase hardening precipitates along grain boundaries was observed, which increases the microhardness to $\sim$140 HV. But, these S-phase precipitates are over-aged and coarsened near the TMAZ, which in turn lowers the microhardness to $\sim$120 HV as well. In the TMAZ itself the S-phase hardening precipitates are coarsened even more and the microhardness is lowered to a minimum of 109 ± 2 HV. Finally, the NZ has coarsened S-phase precipitates as well, but the presence of recrystallised GPB zones and very fine equiaxed grains of $\sim$5 μm increases the microhardness slightly to $\sim$130 HV [32], [90]. The microhardness evolution and phase fractions of the GPB zones and S-phase across the weld cross-section of FSW'd AA2024-T3 are shown in Figure 7.

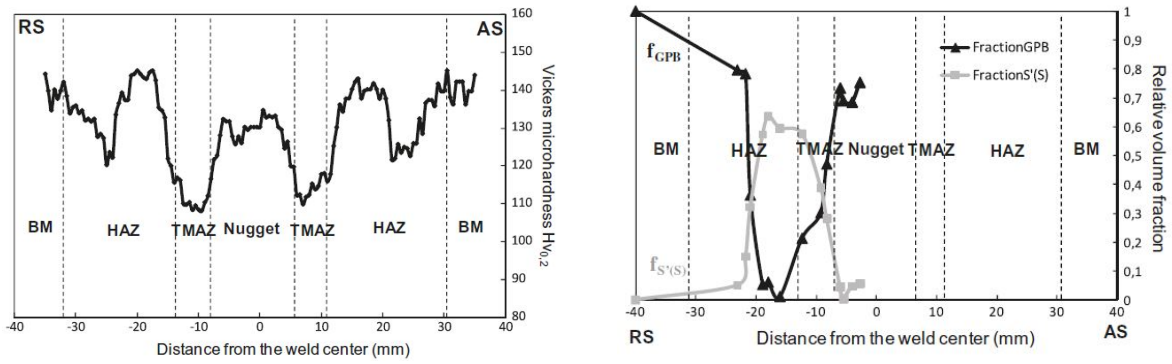

(a) (b)

Figure 7: *(a) Vickers microhardness profile $Hv_{0.2}$ of a cross-section in LT-direction of 12 mm thick FSW'd AA2024-T3 sheets measured with a 0.5 mm step. (b) Phase fractions of GPB zones and S-phase across the same weld section of AA2024-T3, determined by differential scanning calorimetry (DSC) analysis. Images after Bousquet, Poulon-Quintin, Puiggali,* et al. *[32].*

The influence of welding on the tensile properties in LT-direction (perpendicular to the weld direction) is discussed in several papers as well. Most authors primarily focus on the change in ultimate tensile strength (UTS) and elongation (el), some report the change in yield strength (YS) as well. This change is either expressed by their measured value or by the joint efficiency, which is expressed as $UTS_{FSW}/UTS_{BM} \cdot 100\%$ for the ultimate tensile strength and $el_{FSW}/el_{BM} \cdot 100\%$ for the elongation. Radisavljevic, Zivkovic, Radovic, *et al.* [84] reported an UTS of 481 MPa and 18% elongation for the BM of 6.0 mm bare AA2024-T351 sheets and achieved a maximum joint efficiency in terms of UTS and el of 82.3% and 41.7%, respectively. Zhang, Xiao, and Ma [92] reported an UTS of 480 MPa and elongation of 21% for the BM of 5.0 mm bare AA2024-T351 sheets and achieved a maximum joint efficiency of 95.2% for the UTS and 42.9% for the el. Finally, Li, Xu, Li, *et al.* [91] reported an UTS of ∼480 MPa for the BM of 3.2 mm bare AA2024-T3, which dropped to ∼420 MPa after welding, which is a joint efficiency of 87.5%. The elongation dropped from 18.2% before welding to 8.7% after welding, which is a joint efficiency of 47.8%. The fracture locations of the tensile specimens were linked to the zone with the lowest microhardness values. These were mostly either on the RS or the AS of the NZ/TMAZ interface. However, some authors reported a fracture occurring in the HAZ as well [91].

2.2.3 Stationary shoulder FSW

Stationary shoulder friction stir welding (SSFSW) was developed by TWI in order to weld titanium alloys, which have high strength at high temperatures and a low thermal conductivity, making these alloys difficult to weld using FSW [13]. However, since SSFSW offers many advantages over conventional FSW, SSFSW has been used for welding aluminium alloys such as the 2000 series as well [93]. In SSFSW, the weld tool still consists of a shoulder and pin, but the shoulder no longer rotates. The rotation and travel of the pin is now fully responsible for the material flow, heat cycle and resulting microstructure. Since a smaller area is stirred, less material is displaced and heat is spread less across the weld, resulting in a smaller temperature gradient [94]. Wu, Chen, Strong, *et al.* [14] reported a narrower weld with smaller TMAZ and HAZ due to a decrease in heat input of 30% in SSFSW, compared to conventional FSW. The shape and size of the NZ follow that of the pin shape and size, and is no longer affected by the shoulder. Figure 8 shows an example of

the designs of a conventional FSW tool and SSFSW tool. The difference in macrostructure (of an AA6061-T6 butt weld) between FSW and SSFSW is shown in Figure 9. Several advantages of SSFSW over conventional FSW are listed by Meng, Huang, Cao, *et al.* [95]: Less heat generation results in less softening of the (surface) material and less overflow of this material (flash), resulting in a smoother surface and less weld-thinning. This in turn improves fatigue strength and bearable load area, and lowers the need for surface machining after welding. The decreased spread of heat lowers the width of the TMAZ and HAZ and improves the homogeneity of the welded material in thickness direction, which improves the mechanical properties. Finally, T-joints and corner joints are better weldable with SSFSW, as are materials with low thermal conductivities, such as titanium alloys.

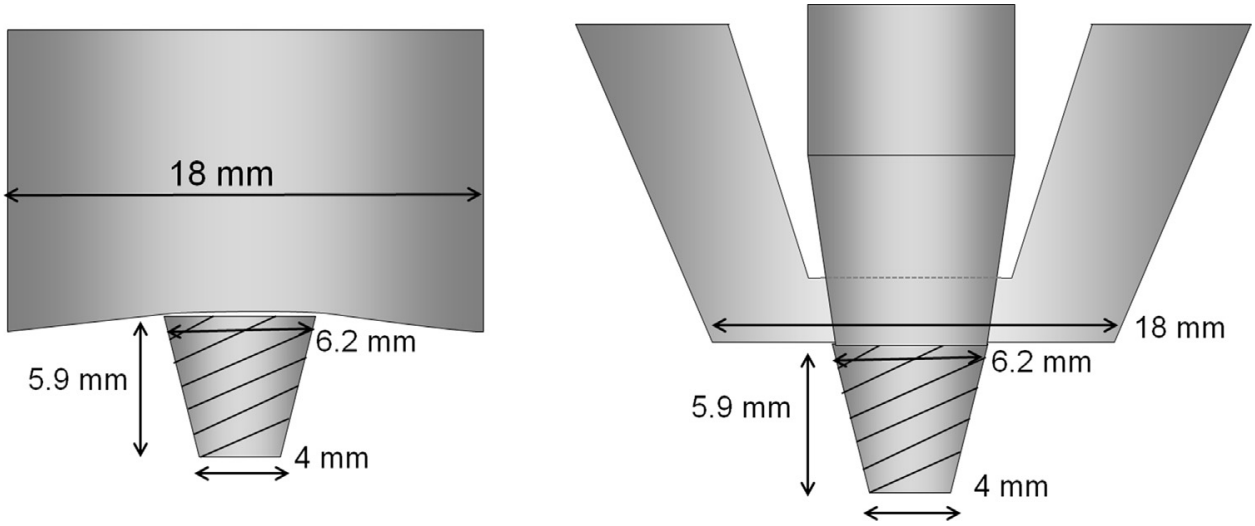

Figure 8: *Schematic diagrams of tools used in FSW (left) and SSFSW (right) with their dimensions. The pins have similar designs, but the stationary shoulder is noticeably more flat than the rotating shoulder, which is concave. Image after Wu, Chen, Strong,* et al. *[14].*

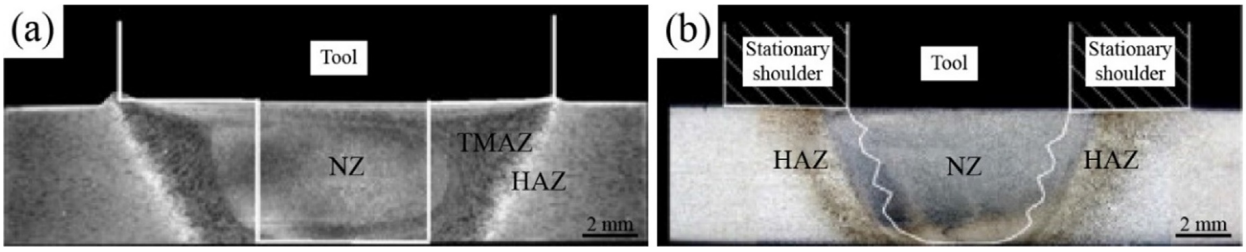

Figure 9: *Transverse cross-sections of a friction stir welded AA6061-T6 butt joint, using (a) conventional rotating shoulder and (b) stationary shoulder. A schematic of the tools applied is showed on top of the cross-section. The figure shows the reduction of the TMAZ and HAZ in SSFSW as compared to FSW. Image adjusted from Meng, Huang, Cao,* et al. *[95].*

2.3 Corrosion mechanisms and test methods

2.3.1 Introduction to corrosion of aluminium

Corrosion is the process of the degradation of a material, most commonly metals, by way of exchanging electrons and ions through an electrochemical circuit [96]. The exchange of electrons and ions happens at two locations simultaneously, oxidation of the metal happens at an anodic site and reduction of oxygen or hydrogen happens at a cathodic site. In general, corrosion is a uniform process, meaning that the surface of the material degrades uniformly. However, several forms of local corrosion exist, such as pitting corrosion, intergranular corrosion (IGC), stress corrosion cracking (SCC), corrosion fatigue (CF), crevice corrosion, exfoliation corrosion (EXCO), filliform corrosion and erosion corrosion [96].

Aluminium usually corrodes uniformly, but a thin oxide (Al_2O_3) layer is formed in neutral conditions (pH 4-9) that protects the substrate from further corroding through re-passivation [36], [50], [97]. However, aluminium is susceptible to pitting corrosion in the presence of open air solutions containing halide ions (halogen atoms with a negative charge, which usually form salts with positive ions) [97]. Chloride ions (Cl^-) in particular interfere with the formation of a stable oxide layer, due to the rapid polarisation of aluminium to its pitting potential in the presence of oxygen [98], [99].

The oxidation (Ox) and reduction (Red) reactions of pure aluminium in aerated neutral aqueous solution are shown below [96]:

$$Ox : 2Al + 3H_2O \rightarrow Al_2O_3 + 6H^+ + 6e^- \tag{2}$$

$$Red : O_2 + 2H_2O + 4e^- \rightarrow 4OH^- \tag{3}$$

In (dearated) acidic solutions such as pit environments, aluminium is dissolved into metal cations and hydrogen is reduced [33]:

$$Ox : Al \rightarrow Al^{3+} + 3e^- \tag{4}$$

$$Red : 2H^+ + 2e^- \rightarrow H_2 \tag{5}$$

The oxidation reaction during corrosion of aluminium in alkaline aqueous environments and corresponding reduction reactions are given in Appendix A.1.

2.3.2 Corrosion of AA2024-T3

Whilst pure aluminium is fairly corrosion resistant due to the formation of the passive oxide layer, the presence of second phase particles in AA2024-T3 increases the susceptibility to localised corrosion and severity of the corrosion attack. Second phase particles such as hardening precipitates increase the mechanical properties, but reduce the corrosion resistance due to local galvanic cells caused by differences in electrochemical potential between the particles and the aluminium matrix [36], [97]. Hughes, Birbilis, Mol, *et al.* [33] discuss the associated corrosion of microstructural features in high strength aluminium alloys, an overview of which is given in Table 3. The formation of hardening precipitates such as S-phase and θ-phase and dispersoids such as $Al_{20}Cu_2Mn_3$ was discussed in section 2.1.1 and section 2.1.2. In short, clusters of IMPs, dispersoids, hardening precipitates and grain boundaries act as targets for corrosive attacks which can eventually lead to pitting, IGC, SCC and EXCO [15], [17]–[26], [36], [64], [100].

Table 3: *Overview of microstructural features and associated corrosion in high strength aluminium alloys. Table after Hughes, Birbilis, Mol,* et al. *[33].*

Microstructural Feature (and when formed)	**Size**	**Associated Corrosion**
Atomic Defects (At any time during processing)	Point Defects: <1 Å, Line defect: tens of nm long dislocations	Grain etchout associated with higher grain stored energy.
Grain Boundaries (At any time during processing)	Tens of nm wide (including the zone of influence such as depleted zones)	Intergranular attack. Some evidence from misorientation angle for preferred corrosion, generally only facilitated by second phase precipitates.
Hardening Precipitates (Ageing after Solution treating)	20 nm x 200 nm	Can facilitate intergranular attack.
Dispersoids (Ageing after Solution treating)	50 nm x 400 nm	Under some conditions undergo preferential attack.[a]
Constituent Particles and Impurity Particles (Primary Ingot Production)	Generally 0.5 μm to 50 μm	Localised attack of particle if anodic w.r.t. the matrix and trenching in surrounding matrix if cathodic to the matrix.
Clusters of particles (Ingot Working)	50 μm to 500 μm	Associated with pitting attack that propagates into the surface.

[a] Preferential attack is the active anodic corrosion of a particle in the right environment.

Pitting corrosion is the localised attack of a surface leading to rapid penetration of this surface in small areas, forming pits. Pits are usually small in surface area and are often covered by corrosion products, with deep voids below these products. Chloride containing solutions help break down the oxide layer and initiate pitting, which occurs when the breakdown potential or pitting potential (E_{pit}) is reached. E_{pit} can be used to measure the resistance to pitting corrosion [96]. The bulk material of AA2024-T3, pure aluminium, and (clusters of) IMPs each have individual breakdown potentials, which are dependent on the corrosion environment (type of electrolyte, pH-value, temperature, availability of oxygen) Guillaumin and Mankowski [16], Hughes, Parvizi, and Forsyth [59], and Li and Dang [101]. The open circuit potential, corrosion potential, pitting potential and corresponding corrosion current density of AA1050 (Alclad), AA2024-T3 and IMPs found in AA2024-T3 are presented in Table 4. A more complete overview is given by Li and Dang [101] and Hughes, Parvizi, and Forsyth [59].

Table 4: *The open circuit potential (E_{ocp}), corrosion potential (E_{corr}), pitting potential (E_{pit}) and corrosion current density (i_{corr}) of relevant alloys and intermetallic particles (IMPs) in several environments.*

Alloy/IMP	**Electrolyte**	**E$_{ocp}$ (mV/SCE)**	**E$_{corr}$ (mV/SCE)**	**E$_{pit}$ (mV/SCE)**	**i$_{corr}$ (μA/cm^2)**	**Ref.**
AA1050	0.1 M Na_2SO_4 + 100 mg/L NaCl	-	-	-	0.89	[102]
AA1050	58.5 g/L NaCl + 9 mL 30% H_2O_2	-770	-	-	-	[36]
AA2024-T3	58.5 g/L NaCl + 9 mL 30% H_2O_2	-600	-	-	-	[59]
AA2024-T351	3.5% NaCl	-610	-	-690	-	[59]
AA2024-T3	0.1 M NaCl	-555	-	-	6.7	[19]
Al_2Cu	0.1 M NaCl	-484	-	-	3.5	[19]
Al_2CuMg	0.1 M NaCl	-830	-	-	11	[19]
Al_2Cu	3.5% NaCl	-	-695	-652	-	[101]
Al_2CuMg	3.5% NaCl	-	-1061	135	-	[101]
$Al_{20}Cu_2Mn_3$	3.5% NaCl	-	-617	-534	-	[101]

Several studies exist on the initiation and propagation of pits in AA2024-T3(51), many of which attribute the initiation of pitting to either selective dissolution of the S-phase caused by dealloying of magnesium and aluminium, or by dissolution of grain boundaries and the aluminium matrix nearby IMPs (trenching) [15]–[19], [25]. Wang, Zhang, Wu, *et al.* [24] discovered that pitting initiation near S-phase precipitates depends on the size of the precipitates; S-phase particles below 10 nm in size do not initiate pits. Instead, pits are formed around $Al_{10}Cu_2Mn_3$ dispersoids. Copper depleted zones and dispersoid free zones around IMPs also alter the effect of pitting initiation [59]. Local galvanic coupling between anodic and cathodic IMPs or IMPs and the aluminium matrix can enhance the localised corrosion attack, leading to stable pitting [20]. Stable pitting is also associated with clusters of IMPs [59]. Stable pitting can lead to intergranular attack or intergranular corrosion (IGC) [21], [22], [26], where the corrosion attack preferentially follows the grain boundary network [23], [103]. Figure 10 shows cross-sectional examples of undercut pits and intergranular corrosion damage in AA2024-T3(51).

2.3.3 Corrosion of FSW'd AA2024-T3

Many factors influence the corrosion susceptibility of FSW'd AA2024, including initial production, heat treatment, residual stresses and weld parameters [8]. The weld parameters have the most influence on corrosion susceptibility, since these parameters influence the heat cycle, grain size and distribution and dissolution of IMPs [8], [10]. When optimal weld parameters are used the corrosion susceptibility is lowered [10]. An overview of observed corrosion behaviour in FSW'd AA2024 is given in Table 5.

Similar to unwelded AA2024-T3, FSW'd AA2024-T3 is susceptible to pitting, IGC and SCC [7], [27]–[31], [104]–[106]. Unwelded AA2024-T3 is susceptible to local corrosion due to the heterogeneous microstructure having local differences

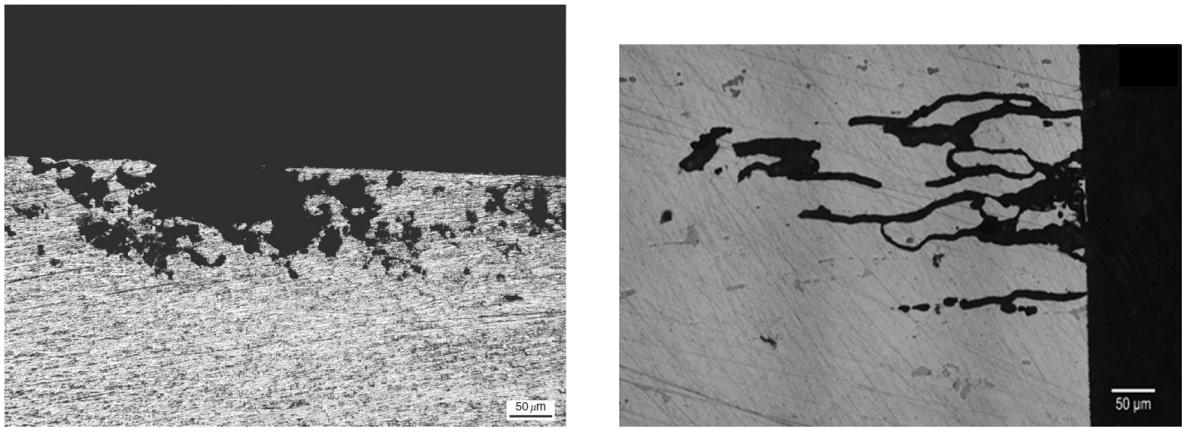

(a) (b)

Figure 10: *Cross-sectional optical micrographs showing (a) undercut pits in the top surface of AA2024-T3 after 8 hours of exposure to EXCO solution (200x mag.), and (b) intergranular corrosion defects in L-direction of AA2024-T351 after 24 hr exposure at E_{corr} in 1 M NaCl solution. Images after (a) Pantelakis, Setsika, Chamos,* et al. *[26], and (b) de Bonfils-Lahovary, Laffont, and Blanc [103].*

Table 5: *Overview of corrosion behaviour for different zones observed in 2024 aluminium alloy. Table adjusted from Threadgill, Leonard, Shercliff,* et al. *[8].*

Corroding zone	**Mechanism**	**Test used**	**Ref.**
TMAZ Nugget	Exfoliation Pitting/blistering	ASTM G34	[27]
Nugget HAZ/parent	Intergranular/pitting (150 μm) Pitting to 150 μm	Immersion (NaCl +H_2O_2)	[27]
HAZ	Intergranular	Immersion (NaCl)	[28], [31]
Nugget and HAZ	Intergranular attack (low rotation speeds in nugget/high speeds predominantly HAZ)	Gel visualisation and Immersion (NaCl+H_2O_2)	[29], [30]
Nugget/HAZ Parent	Passive Pitting	Polarisation curves and electrochemical impedance spectroscopy (EIS) in NaCl	[7]

in breakdown potential (Table 4) due to the presence of (clusters of) IMPs, such as S-phase [59]. Grain boundaries are perfect locations for hardening precipitates to develop during heat treatment or welding. Continuous lines of S-phase precipitates were observed along grain-boundaries in the HAZ of FSW'd AA2024-T3 (Figure 11), which have been found to enhance IGC [31], [32]. Differences in grain size and IMP distribution causes differences in potential between the BM and weld zones (Figure 12), which leads to galvanic coupling between these zones, enhancing corrosion attack in the weld [32]. Pits with a depth of 160 μm (HAZ) [32], 25-225 μm (NZ) and 60-300 μm (HAZ) [30], and 50-300

μm (HAZ) [31] were observed after exposure to IG and EXCO solution for 6-48 hours[3]. Jariyaboon, Davenport, Ambat, *et al.* [30] reported breakdown potentials of -0.58 V to -0.60 V (vs Ag/AgCl) for the BM and -0.65 V to -0.70 V (vs Ag/AgCl) for the nugget and HAZ of AA2024-T351. Bousquet, Poulon-Quintin, Puiggali, *et al.* [32] reported open circuit potentials (OCP) of -630 mV vs SCE in the centre of the weld (NZ/TMAZ/HAZ) and an OCP of -555 mV vs SCE in the BM of AA2024-T3. There were no corrosion current densities reported in either paper.

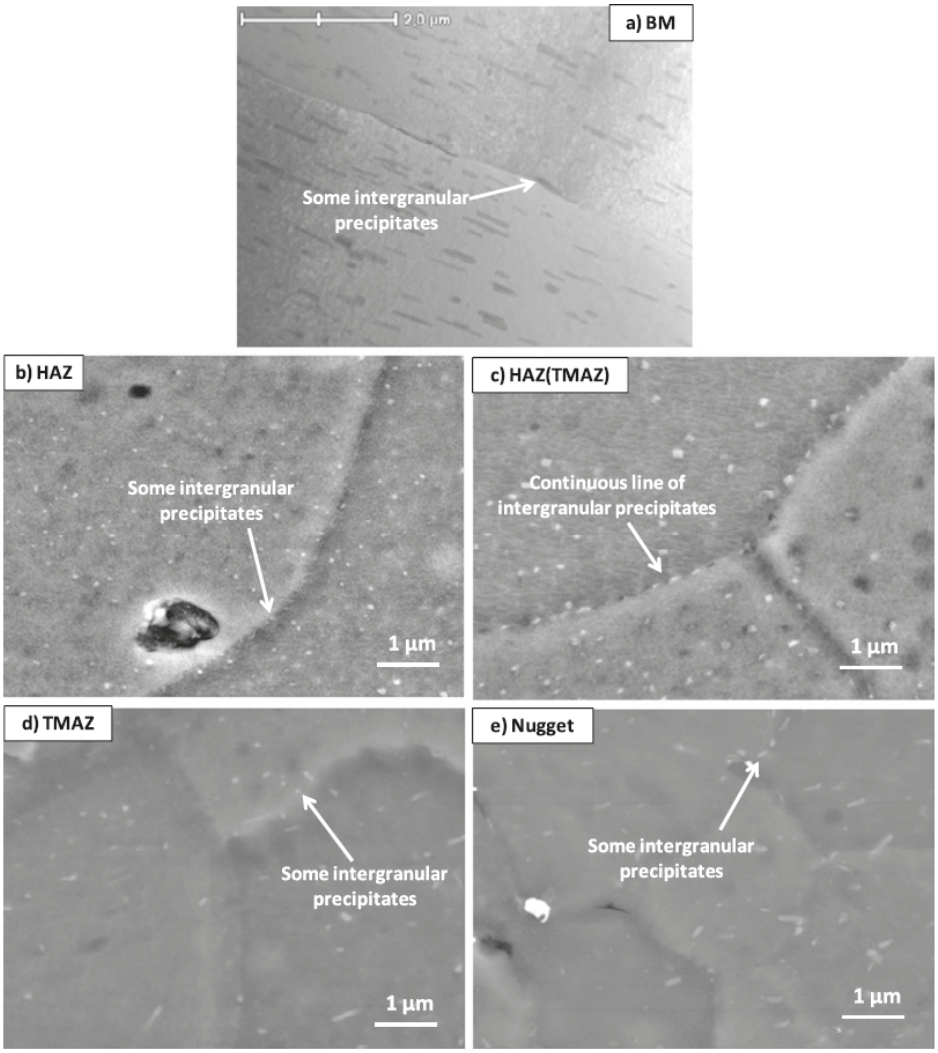

Figure 11: *Microstructure of FSW'd AA2024-T3 showing intergranular precipitates in the (a) BM, (b) HAZ, (c) HAZ near TMAZ, (d) TMAZ, (e) NZ. The continuous lines of intergranular S-phase precipitates in the HAZ (near TMAZ) enable homogeneous IGC. Image after Bousquet, Poulon-Quintin, Puiggali,* et al. *[32].*

[3]IG solution consists of 0.98 M NaCl and 0.09 M H_2O_2 (ASTM-G110) and EXCO solution consists of 4 M NaCl, 0.5 M KNO_3 and 0.1 M HNO_3 (ASTM-G34) [107], [108].

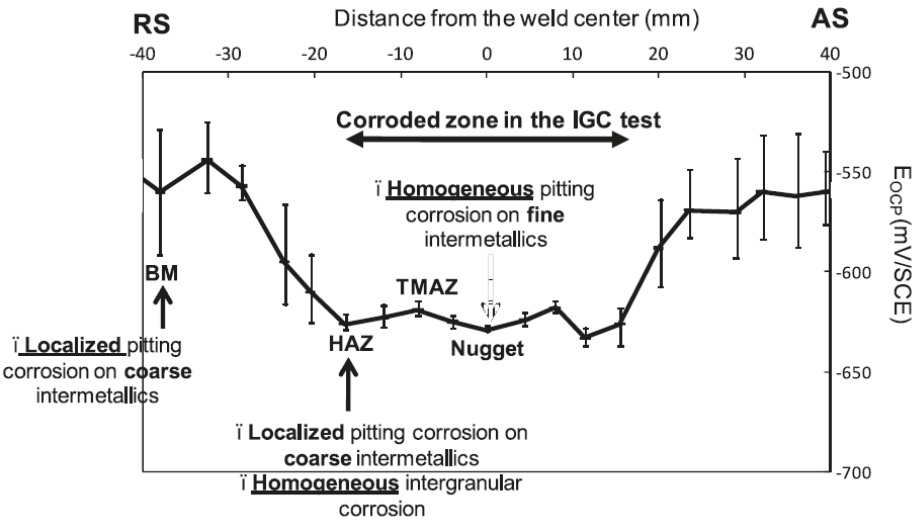

Figure 12: *Open circuit potentials at different locations across the weld of FSW'd AA2024-T3, correlated with different corrosion behaviours per zone. All zones are susceptible to corrosion, but the HAZ is most susceptible due to the presence of both coarse and fine IMPs (GPB-zones and S-phase). Image after Bousquet, Poulon-Quintin, Puiggali,* et al. *[32].*

2.3.4 Corrosion of stationary shoulder FSW'd AA2014

Unfortunately, to the knowledge of the author of this thesis an extensive literature search has shown no open sources on the corrosion behaviour of stationary shoulder friction stir welded (SSFSW'd) AA2024-T3. However, Sinhmar and Dwivedi [109] compared the corrosion behaviour of FSW'd and SSFSW'd AA2014, which should have similar composition as AA2024 (Table 1), although no information about the actual composition of the used sheets was given in this paper. Nonetheless, this paper may provide some insights in the corrosion behaviour of SSFSW'd AA2xxx alloys. Sinhmar and Dwivedi [109] show in their paper that SSFSW produced a smaller HAZ with less grain boundary precipitates than conventional FSW, which they attributed to a decreased heat input from the stationary shoulder. Furthermore, precipitates were reported to be of finer size in SSFSW, which are mostly θ-phase precipitates (lower Mg content means less S-phase precipitates form!). Next, through potentiodynamic polarisation tests in 3.5% NaCl solution it was shown that the NZ and HAZ of the SSFSW'd joint have more noble corrosion potentials (-619 mV and -643 mV vs SCE, respectively) than the NZ and HAZ of the conventional FSW'd joint (-641 mV and -664 mV vs SCE, respectively). However, no information on the corrosion current densities was given. Next, electrochemical impedance spectroscopy (EIS) measurements showed an increase in polarisation resistance in both NZ and HAZ of the SSFSW'd joint with respect to the FSW'd joint: from 3450 $\Omega \cdot cm^2$ for the NZ of the FSW'd joint to 5974 $\Omega \cdot cm^2$ for the NZ of the SSFSW'd joint, and from 2523 $\Omega \cdot cm^2$ for the HAZ of the FSW'd joint to 3165 $\Omega \cdot cm^2$ for the HAZ of the SSFSW'd joint. Furthermore, it was stated (not shown!) that less pitting occurred in the NZ of the SSFSW'd joint than the NZ and HAZ of the FSW'd joint, which showed severe pitting. Finally, it was concluded that the finer and fewer amount of grain boundary precipitates in the HAZ and smaller size of the HAZ due to the lower heat input resulted in a higher corrosion resistance in the SSFSW'd joint as compared to the FSW'd joint, which is summarised in Figure 13.

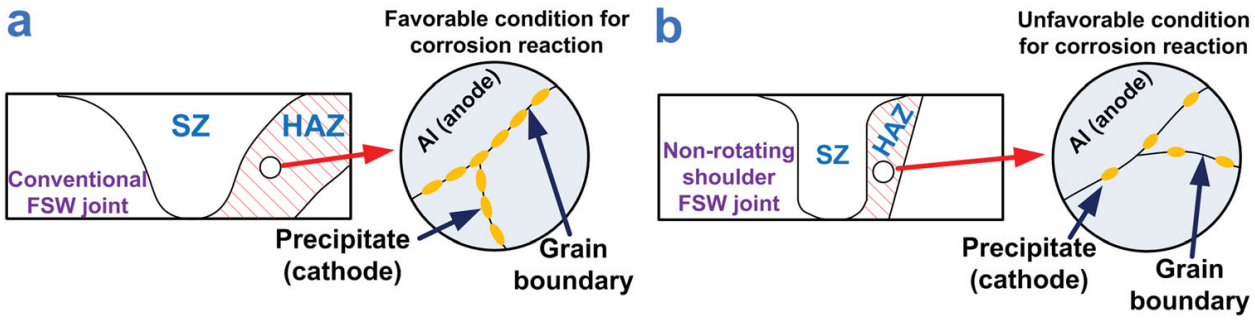

Figure 13: *Schematic showing the Al_2Cu (θ-phase) precipitates along the grain boundary of HAZ of (a) conventional FSW'd joint and, (b) SSFSW'd joint, showing the favourable and unfavourable conditions for corrosion attack in AA2014, respectively. Image after Sinhmar and Dwivedi [109].*

To the knowledge of the author of this thesis, no studies exist on the corrosion behaviour of SSFSW'd AA2024. Only a few papers exists on the effect of weld parameters on the mechanical properties of SSFSW'd AA2024 lap joints. Since the lack of rotating shoulder alters the heat cycle and plastic deformation of the weld, and therefore alters the microstructure and resulting mechanical and corrosion properties, it is suggested to perform a study on the microstructure and resulting properties of SSFSW'd AA2024-T3, using similar test methods conventionally performed for friction stir welds.

2.3.5 Cladding as a form of corrosion protection

Cladding is a form of cathodic protection frequently used in aerospace industry, in which a more anodic surface layer is applied on the top and/or bottom surfaces of a more cathodic substrate. A commercially pure aluminium alloy called Alclad (AA1050, Table 1) is used for the cathodic protection of AA2024-T3, which is hot co-rolled on ingots of AA2024 during sheet production [36]. Since the clad layer of AA1050 has a more negative open circuit potential (-770 mV vs SCE) than AA2024 (-610 mV vs SCE)[4], the clad layer is preferentially attacked, protecting the substrate from pitting and exfoliation corrosion, even when local defects of up to several centimetres wide exist in the clad layer [36], [99]. Petroyiannis, Pantelakis, and Haidemenopoulos [111] have shown that covering at least 30% of the surface of AA2024 with Alclad is sufficient for corrosion protection. The average clad thickness is 2% to 5% per face as compared to the overall thickness of the sheet [36], which is shown in Figure 14. Unfortunately, the use of cladding lowers the fatigue strength of AA2024-T3 up to 50%, since AA1050 has lower mechanical properties. Therefore, it is advised to carefully consider using Alclad as a protection method for structures exposed to fatigue cycles [99].

[4] in 58.5 g/L NaCl solution with 9 mL 30% H_2O_2 (ASTM-G69) [110].

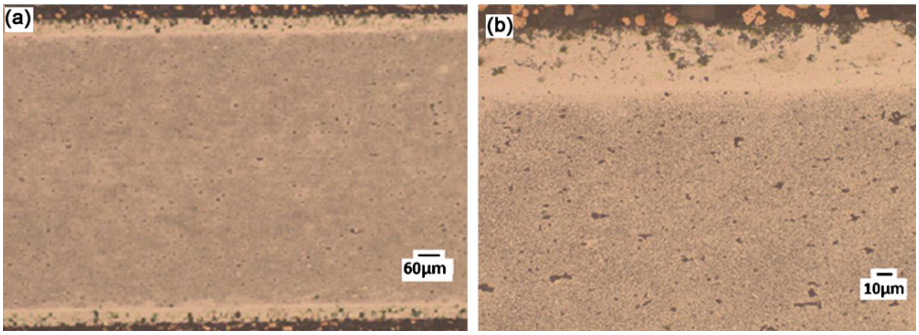

Figure 14: *Optical micrographs of a cross-section of 1.2 mm thick Alclad AA2024-T3 sheet, showing the 50 µm thick clad layer on both sides of the substrate in different magnifications: (a) 50x and (b) 200x (top layer). Image after Lakshmi, Yoganandan, Kavya,* et al. *[112].*

While the effect of cladding on the mechanical and corrosion properties of unwelded AA2024-T3 has been well established, little literature exists on the effect of cladding on the mechanical and corrosion properties of FSW'd AA2024-T3. However, Zhang, Xiao, Wang, *et al.* [37] studied the effect of cladding on the material flow and defect formation in FSW'd AA2024-T351. In short, mixing of cladding into the weld should be avoided, as Zhang, Xiao, Wang, *et al.* [37] refer to an older paper stating that "*cladding mixed into the NZ/TMAZ reduces the mechanical properties of the weld*". Mixing of cladding into the weld can be avoided when optimal weld parameters are used, which are a low traverse speed and/or high rotational speed, with small plunge depth of the shoulder and a proper pin length. Similar observations are made by El-Morsy, Ghanem, and Bahaitham [88]. Examples of weld defects and mixing of cladding into the NZ are shown in Figure 15. Three papers by Li, Yue, Ji, *et al.* [113], Xu, Li, Lv, *et al.* [94], and Ji, Li, Zhou, *et al.* [93] show similar conclusions for SSFSW'd Alclad AA2024-T4 lap joints. Dong, Yang, Ren, *et al.* [114] measured a decrease in top surface roughness from 125.5 μm for FSW'd lap joints to 58.9 μm for SSFSW'd lap joints of 0.8 mm thick Alclad AA2024 sheets when optimal weld parameters were used. A decrease in flash and an increase in mechanical properties were also reported. Unfortunately, no studies have been performed on the corrosion behaviour of SSFSW'd Alclad AA2024-T3.

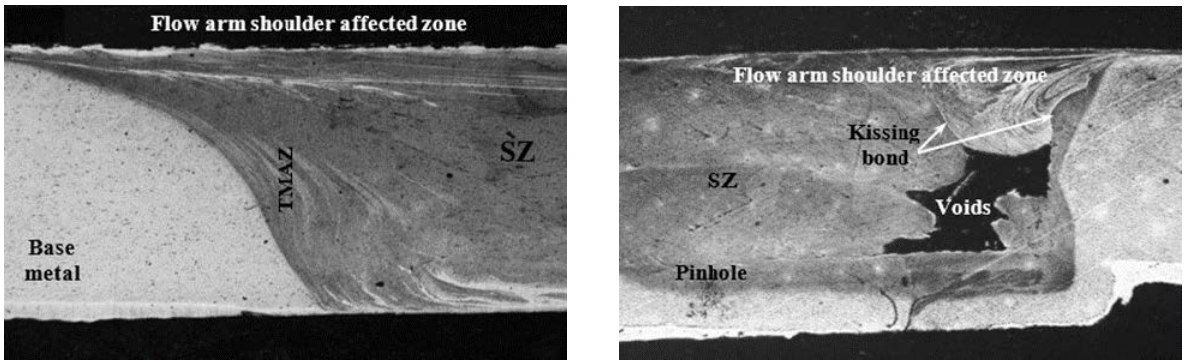

(a) (b)

Figure 15: *Micrographs of friction stir welds of Alclad AA2024-T4 sheets showing defects when improper process parameters are used. (a) Mixing of the cladding (light grey colour) into the SZ and TMAZ (dark grey colour). (b) Kissing bond, void defect and mixing of cladding in the TMAZ. Image after El-Morsy, Ghanem, and Bahaitham [88].*

2.3.6 Testing for corrosion behaviour

Testing for corrosion behaviour can be done by determining the susceptibility or resistance to certain corrosion mechanisms, and/or by determining the kinetics (thermodynamics)) of the corrosion reaction. Ghali [115] suggests to test aluminium alloys for susceptibility to intergranular corrosion (IGC), stress corrosion cracking (SCC) and corrosion fatigue (CF). Plenty of studies have done so for IGC and SCC of unwelded ([16], [20]–[23], [26], [100], [103], [116], [117]) and friction stir welded ([7], [8], [10], [27]–[32], [104]–[106], [109]) AA2024-T3. However, pitting initiation and propagation in unwelded AA2024-T3 has been studied plenty as well ([15]–[19], [24], [25], [65], [66], [100]). Most of these studies have used immersion tests together with microstructural observations and electrochemical techniques to characterise the corrosion behaviour. Microstructural observations were mostly done with optical microscopy (OM) and scanning electron microscopy (SEM) or transmission electron microscopy (TEM), with or without energy dispersive x-ray spectroscopy (EDS). For the immersion and electrochemical tests, most often a solution of NaCl (with or without H_2O_2) with varying molarity was used, although Hughes, Parvizi, and Forsyth [59] mention that Na_2SO_4 solution has been used as well (sulphate slows down the corrosion reaction).

In this thesis, electrochemical tests and immersion tests have been used for determining the corrosion kinetics and susceptibility to pitting corrosion in SSFSW'd AA2024-T3 butt welds. Details regarding the immersion tests are discussed in section 3.5.2 and are based on guidelines from ASTM standards G31 and G46 [118], [119]. Testing for corrosion kinetics is done with an electrochemical cell, in which three electrodes are immersed in a test solution for which the kinetics are being measured, shown in Figure 16. The three electrodes consist of the working electrode, which is the material to be tested, an inert counter electrode (usually platinum, graphite or a stainless steel) and a reference electrode with a stable electrode potential. These electrodes are then connected to a potentiostat which can measure potential or current when the other is applied [120]. The applied electrochemical tests will be discussed briefly hereafter, which are open circuit potential (OCP), linear polarisation resistance (LPR) and potentiodynamic polarisation.

First, the potential of the working electrode versus the reference electrode is measured over time in an open circuit setting, meaning no current or potential is applied to the circuit. Once this measured potential stabilises (usually between

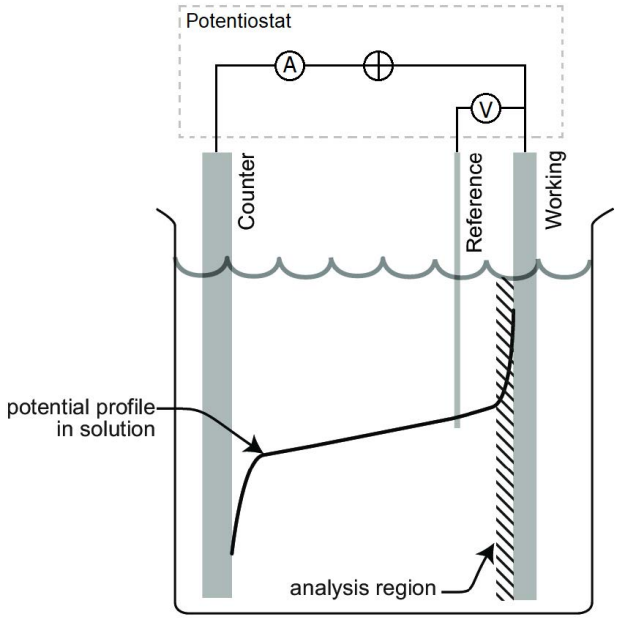

Figure 16: *Schematic of an electrochemical cell with counter, reference and working electrodes immersed in a test solution and connected to a potentiostat. Image after Franklin [121].*

30-60 minutes), the value of the potential is noted down as the open circuit potential, which is the equilibrium potential or corrosion potential in case of corrosion. This potential can be used as an indicator for resistance against corrosion, however this is only when the system is in a steady-state reaction and is not useful for kinetics on its own [120].

Next, the LPR technique is used for measuring resistance against corrosion at steady-state. Polarisation resistance (R_p) limits the charge transfer at the electrolyte-surface interface. In LPR tests, the system is polarised by applying a small potential near the OCP ($\pm$ 10 mV) and measuring the resulting current. Both anodic and cathodic reactions take place simultaneously, and the relationship between the resulting potential and current (normalised to current density) determines the resistance against these reactions. When plotted on a potential versus current density graph using linear scales (Figure 17), the slope of the curve near OCP determines the corrosion resistance (Rp in Equation 6), expressed in $\Omega \cdot cm^2$. Both the OCP and LPR tests are non-destructive, meaning that the surface of the substrate is not drastically altered [120].

$$R_p = \left(\frac{dE}{di}\right)_{E_{corr}} \tag{6}$$

Similarly, a potentiodynamic polarisation technique can be applied after determining the OCP as well. Potentiodynamic polarisation is done by varying the potential at a constant scan rate (typically 600 mV/h) and measuring the resultant current, which is normalised to current density. Usually, the potential range is chosen from -250 mV vs OCP to 250 mV vs OCP, but these ranges can be changed depending on what type of information is sought trough this technique. For example, polarising to +1 V vs OCP can give qualitative insights in passivation and pitting behaviour. Typically, mostly qualitative data can be extracted from the resulting tafel plots, however, some quantitative data on the corrosion kinetics can be extracted as well [120]. This is done with the following equations:

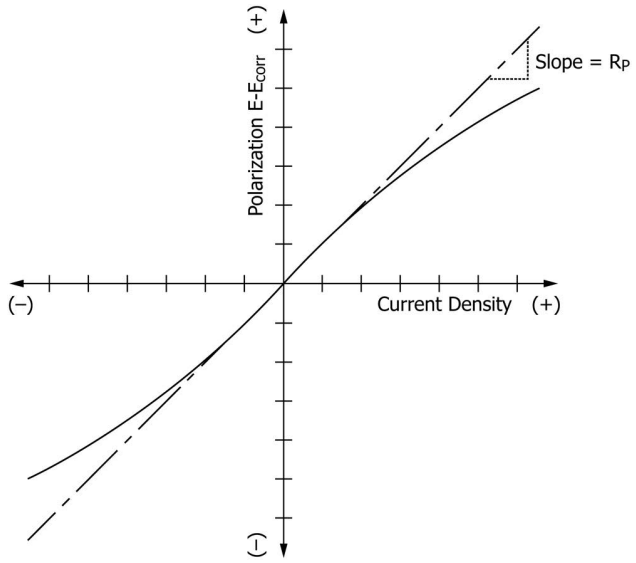

Figure 17: *Theoretical linear polarization plot with linear axes. The cathodic reaction is drawn in the bottom left corner, whereas the anodic reaction is drawn in the top right corner. Image after ASTM International [122].*

$$E_{appl} = E_{corr} - \beta_c log(i/i_{corr}) \tag{7}$$

$$E_{appl} = E_{corr} + \beta_a log(i/i_{corr}) \tag{8}$$

which are the cathodic and anodic potential curves on a potential vs log current density graph (Figure 18), respectively. E_{appl} is the applied potential, E_{corr} is the corrosion potential or open circuit potential, β_c is the cathodic tafel slope, β_a is the anodic tafel slope, i is the measured current per area ($i = I/A$), and i_{corr} is the corrosion current density. The corrosion current density (i_{corr}) can also be extracted from the intersection of the extrapolated linear parts of these slopes, which is called the tafel extrapolation method. The corrosion current density is inversely related to the corrosion resistance (R_p) by the following equation [120]:

$$R_p = \frac{B}{i_{corr}} \tag{9}$$

in which $B = \beta_c\beta_a/(2.303(\beta_c + \beta_a))$ [122]. The derivation of Equation 9, which is called the Stern-Geary equation, is explained thoroughly by Jones [96]. From the corrosion current density, the uniform corrosion rate can be determined using Faraday's law, however this is not applicable to localised forms of corrosion [120]. Finally, E_{pit} can be extracted from the potential versus log current density graph as well, since this is the potential at which a large increase in current density is visible after passing the open circuit potential [120].

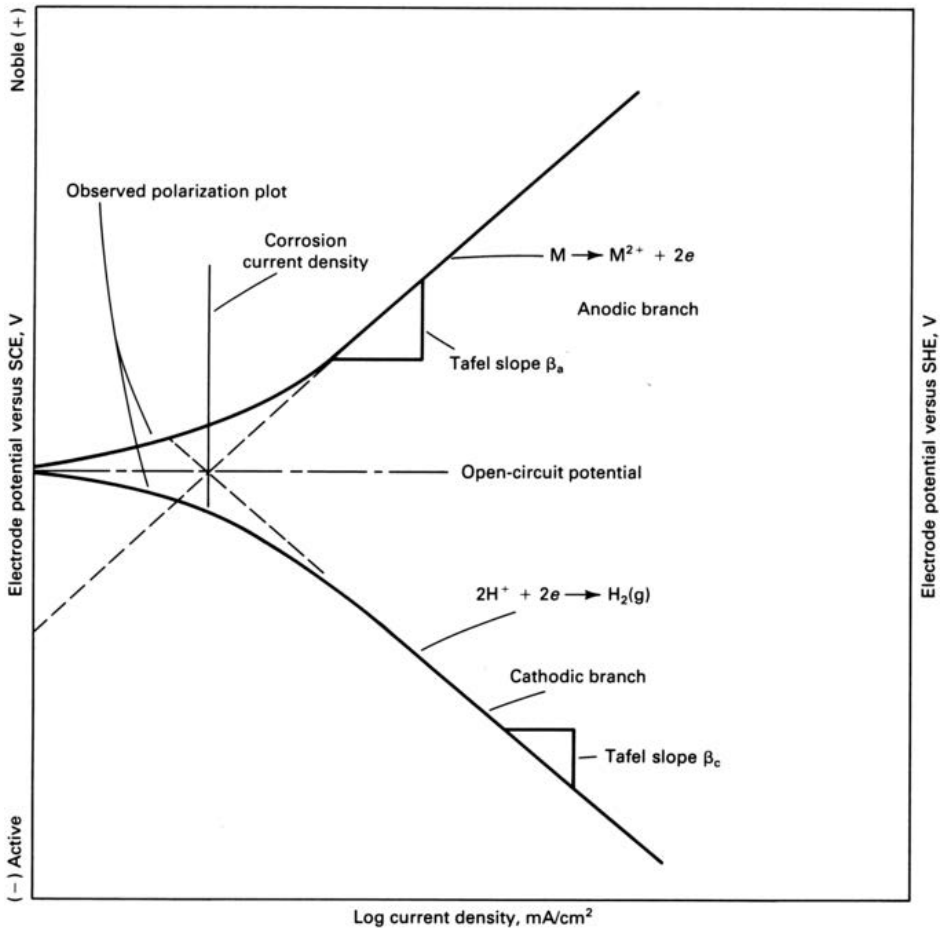

Figure 18: *Tafel extrapolation method as illustrated by theoretical tafel plots. Image after Mansfeld [120].*

2.4 Summary of literature review

Several conclusions can be drawn from this literature study:

1) Due to the heterogeneous microstructure of bare and Alclad AA2024-T3 and its welded equivalent very localised corrosion occurs: IMPs such as coarse consituents, dispersoids and hardening precipitates have different corrosion potentials with respect to each other and the aluminium matrix, which leads to pitting, IGC and SCC. Trenching around and dealloying of these IMPs due to local galvanic corrosion are the precursor for severe corrosion of both unwelded and FSW'd AA2024-T3. Grain boundaries are also locations of corrosion attack, mostly susceptible to IGC.

2) The HAZ is the most susceptible to local corrosion due to the formation of continuous lines S-phase precipitates along grain boundaries, which enhances IGC. The aluminium matrix, clad layer and NZ mainly show pitting corrosion.

3) An Alclad layer provides cathodic protection in unwelded AA2024. No publicly available studies exist on the corrosion performance of FSW'd Alclad AA2024, however studies have shown that cladding should not be mixed into the weld as this leads to lessening of mechanical properties.

4) SSFSW'd AA2014-T3 showed improved corrosion resistance with respect to conventionally FSW'd AA2014-T3, due to a lower presence of S-phase precipitates along the grain boundaries in the smaller HAZ of the SSFSW'd joint.
5) The mechanical behaviour of Alclad AA2024-T4 lap joints was improved with SSFSW over conventional FSW when optimal process parameters were used. Mixing of cladding was avoided as well.
6) There is not much, if any, publicly available literature on the microstructure and resulting mechanical and corrosion properties of SSFSW'd bare and Alclad AA2024-T3 butt joints. Therefore, the microstructure of these welds should be investigated using OM and SEM(-EDS), and electrochemical measurements together with immersion tests should be performed to determine the corrosion behaviour. 3.5% NaCl solution is an often used solution in corrosion studies of AA2024-T3 and is therefore recommended.

2.5 Research objectives

The main objective of this research project, based on the knowledge gaps presented in previous sections, is to characterise the microstructure and resulting mechanical and corrosion properties of SSFSW'd bare and Alclad AA2024-T3 butt welds. Particularly, mechanical properties such as microhardness, ultimate tensile strength and elongation, and corrosion properties such as susceptibility to and severity of pitting corrosion are to be determined. For this purpose, three weld configurations are made available, which are 1.6 mm thick bare, 1.6 mm thick Alclad and 3.2 mm thick Alclad sheets. Subsequently, several sub-objectives or research questions were defined:

1) What are the dimensions of macrostructural features and surface appearance of the SSFSW'd joints, in terms of weld zone size, grain size, surface roughness, weld thinning, and flash?
2) Is there a relationship between the macrostructural features, microhardness, tensile properties and fracture locations of the welds?
3) Which weld zones are the most susceptible to pitting corrosion in terms of pit dimensions and effect on tensile properties, and is there a relationship with the macrostructure and local electrochemical properties??
4) How effective is Alclad as a corrosion protection method for SSFSW'd joints, and is Alclad feasible in terms of impact on mechanical properties and macrostructural features?
5) Which weld configuration (1.6 mm bare, 1.6 mm Alclad, 3.2 mm Alclad) performs best with respect to the mechanical and corrosion properties?
6) How do the SSFSW'd joints compare to FSW'd joints from literature, with respect to macrostructural features, mechanical properties and corrosion behaviour?

3 Materials and Methods

3.1 Materials

3.1.1 Raw and welded materials

Bare and Alclad aluminium alloy AA2024-T3 sheets (125 mm x 500 mm) with nominal thicknesses of 1.6 mm and 3.2 mm were provided by Constellium (CONS), AMAG rolling GmbH (AMAG) and Kaiser Aluminum (Kaiser). For Alclad sheets, cladding in the form of AA1050 was applied on both top and bottom surfaces. Their chemical composition is shown in Table 6 as given by the suppliers based on X-ray fluorescence and optical emission spectrometry for CONS, optical emission spectrometry for AMAG, and spark atomic emission spectrometry for Kaiser. Reported tensile properties of the delivered sheets in LT-direction are as follows: The 1.6 mm bare sheets have an ultimate tensile strength (UTS) of 473 $\pm$ 3 MPa and an elongation (el) of 24 $\pm$ 1 %. The 1.6 mm Alclad sheets have a UTS of 438 $\pm$ 1 MPa and an el of 17 $\pm$ 1 %. Finally, the 3.2 mm Alclad sheets have a UTS of $\sim$454 MPa and an el of $\sim$19.5 %.

Table 6: *Composition of supplied AA2024-T3 sheets in weight percent (wt.%), with aluminium as the remainder (Rem.) or actual value. The clad layer applied is AA1050.*

Sheet	Cu	Mg	Mn	Si	Fe	Zn	Cr	Ti	Al	Prod.
1.6 mm bare	4.2	1.4	0.48	0.07	0.14	0.12	0.01	0.02	Rem.	CONS
1.6 mm Alclad	4.4	1.5	0.49	0.08	0.11	0.11	0.03	0.04	Rem.	AMAG
$\hookrightarrow$ Clad layer	0.00	0.00	0.00	0.11	0.28	0.00	-	0.02	99.58	AMAG
3.2 mm Alclad[1]	4.8	1.4	0.59	0.06	0.15	0.17	0.01	0.03	Rem.	Kaiser

[1] No chemical composition for the clad layer was specified.

Before welding, the cladding was removed from the face (topside) of the 1.6 mm Alclad and 3.2 mm Alclad sheets along the edges of the future butt weld. For clad removal, the 1.6 mm Alclad sheet was abraded by hand and the 3.2 mm Alclad sheet was machined. All sheets were then friction stir welded using a stationary shoulder in a square butt joint configuration by The Welding Institute (TWI) along their long side, which is parallel with the rolling direction. This was a force-controlled process with constant pin length. Two different pin geometries were used for the welding of the 1.6 mm and 3.2 mm thick sheets. Details of the welding parameters and pin geometries are confidential and are available upon request by the thesis committee only. In total 3 SSFSW'd sheets with final dimensions of 250 mm x 500 mm were used for testing, shown in Figure 19.

3.1.2 Specimens

DEMO TU-Delft produced the following specimens from each of the 3 welded sheets using water jet cutting: 6x sheet-type tensile specimens with the weld in the middle, 3x subsize type tensile specimens from the BM only, and 2x rectangular specimens (50 mm x 20 mm) with the weld in the middle (1 for metallurgical observations, microhardness testing and electrochemical tests, 1 for immersion/accelerated corrosion tests). All specimens were oriented in the long transverse direction, which is perpendicular to the rolling and weld direction, as shown in Figure 20. The dimensions of

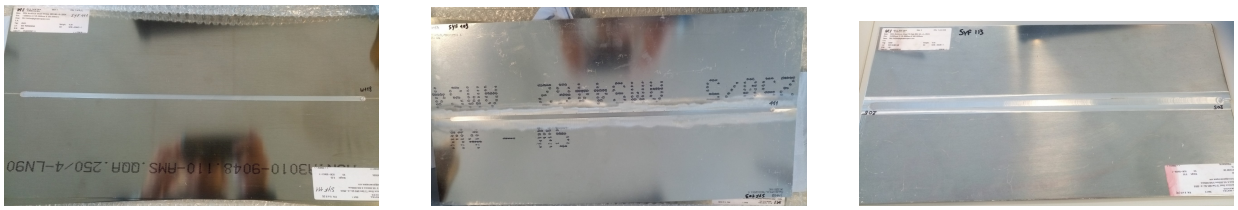

(a) (b) (c)

Figure 19: *Welded sheets (250 mm x 500 mm) used for testing. (a) Bare 1.6 mm sheet. (b) Alclad 1.6 mm sheet with cladding removed from face (topside). (c) Alclad 3.2 mm sheet with cladding removed from face (topside).*

the tensile specimens is shown in Appendix A.2, which were produced according to ASTM-E8/E8M [123]. The weld surfaces of all specimens were kept in as welded condition, meaning that no post-weld surface treatment was applied.

3.2 Overview of experimental approach

In this work, the corrosion behaviours of three configurations of stationary shoulder friction stir welded butt joints were studied using 1.6 mm bare AA2024-T3, 1.6 mm Alclad AA2024-T3 and 3.2 mm Alclad AA2024-T3 sheets. To achieve this, cross-sections of the welds on the long transverse (LT) and short transverse (ST) plane were examined using several techniques. First, the microstructure of the welds was determined by optical microscopy. In order to create the optical micrographs, per welded sheet one of the two rectangular specimens (section 3.1.2) was cold-mounted in epoxy after which the surface in the LT-ST plane was sanded, polished and etched. After microscopy, the microhardness profile across the weld was determined at several positions in ST-direction, namely the face (top), centre and root (bottom) of the weld. The microhardness profiles together with optical micrographs help to identify the location and dimensions of each weld zone (BM, HAZ, TMAZ, NZ) and provide an indication of the strength properties of the zones.

Second, tensile tests were performed on uncorroded and corroded tensile specimens (section 3.1.2) to quantify the effect of corrosion on the tensile properties of the weld. This was done by tensile testing uncorroded specimens taken from the BM, uncorroded specimens with the weld in the middle and corroded specimens with the weld in the middle. The BM specimens were used as a baseline for the tensile properties and checked with the properties provided by the sheets' suppliers, while the weld specimens were compared to one another. Corroding of the tensile specimens was done by continuous immersion in open air aerated 3.5% (0.6 M) NaCl for 24 hours. Together with the tensile specimens, the three remaining rectangular specimens were also immersed in this solution for 24 hours. The rectangular specimens were weighed before and after immersion to determine their mass loss and scanned using white light interferometry (WLI) to quantify the corrosion damage. WLI scans were also used to determine the surface roughness of the weld surfaces and to determine dimensions of weld-defects prior to immersion.

Next, electrochemical measurements were performed on the in epoxy mounted rectangular specimens. Since the microhardness tests were performed on these surfaces previously, these surfaces had to be sanded and polished again. The following tests were done on each weld zone using an electrochemical cell and 3.5% NaCl solution: First, the open circuit potential (OCP) was determined, after which the non-destructive linear polarisation test was performed. Then, a potentiodynamic polarisation test was performed to help create tafel plots, which give insight in the cathodic and anodic behaviour of the weld zone. This data is related to the microstructure and compared to the earlier performed tensile tests

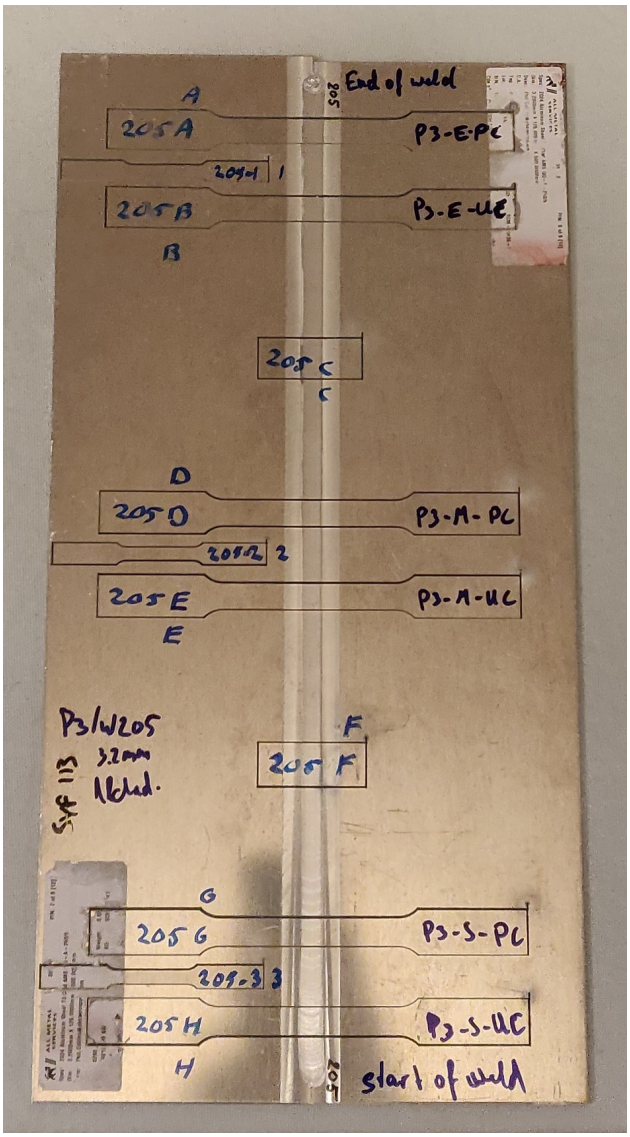

Figure 20: *Representative overview of specimens as cut from the welded 3.2 mm Alclad sheet, showing 6 sheet-type tensile specimens, with 3 subsize tensile specimens and 2 rectangular specimens in between them.*

and immersion tests, in order to match the observed corrosion phenomena and quantitative data. Finally, the observed corrosion behaviour of these SSFSW'd butt joints is compared to corrosion behaviour of FSW'd AA2024-T3 thin sheet found in literature, to see which welding process (FSW or SSFSW) leads to better corrosion properties. The details of each experiment is given in the subsequent sections.

3.3 Sample preparation

3.3.1 Optical microscopy

Three of the six 50 mm by 20 mm rectangular specimens were each cold-mounted (embedded) individually in epoxy resin using Clarocit Liquid and Powder in a 1 to 2 ratio with their cross-sectional area (in LT-ST plane) on the bottom. The specimens were clamped with an inert plastic clamp (MultiClip) such that the specimens would stay upright during pouring. After pouring the specimens were placed in a pressure cooker, where they were kept in an environment with a pressure of 2 Bar for at least an hour, such that any bubbles in the resin could escape and the resin could cure faster. Before embedding, the specimens were cut to size using a Struers watercooled cutting machine to decrease the length of the specimens from 50 mm to +- 25 mm. After embedding, the bottom surface of each specimen was wet ground using Struers Silicon Carbide Grinding Paper starting from grit 80, followed by grits 180, 320, 800, 1200, 2000 up to 4000 on a Struers LaboPol-21 grinding machine. After wet grinding the embedded specimens were cleaned with isopropanol and placed in an ultrasonic bath for 5 minutes. The specimens were then polished on a Struers LaboPol-5 polishing machine, using Struers DiaDuo-2, 3 μm Blue diamond suspension on an MD Mol cloth, followed by a polishing with Struers DiaDuo-2, 1 μm White diamond suspension on an MD Nap cloth. Polishing was done by pressing the specimen onto the doused cloth and rotating the specimen clockwise for a few minutes while the cloth was spinning counter-clockwise with a rotational speed of 50-150 rpm, finished with holding the specimen in the center of the cloth for one minute. The specimens were rinsed with isopropanol in between and after polishing sessions to ensure a clean surface. The surface was polished until mirror surface with minor scratches in random orientation, which was checked with a microscope on 10x magnification. After polishing the specimens were then etched by rinsing the surface with Keller's reagent[5] for 10 seconds per specimen. Etching was done at Fokker Aerostructures BV in Papendrecht, the Netherlands. After etching, the specimens were rinsed with warm water to make sure no etchant was left on the specimens.

3.3.2 Microhardness measurements

Microhardness measurements were done on the same surface of the specimens used for optical microscopy. Before measurements were taken, the surface was wet ground again such that the etched surface was ground down, and then polished to a mirror surface again using 3 μm and 1 μm suspensions and techniques described above.

3.3.3 Tensile tests

Tensile specimens were marked with a waterproof marker to show the gauge length on both sides. Tensile specimens that were corroded were prepared in the same manner as the rectangular specimens before immersion:

3.3.4 Immersion tests

The rectangular specimens were first marked with an unsolvable pencil to be able to identify the specimens after immersion, then they were degreased for 20 minutes in an ultrasonic bath with isopropanol, after which the specimens were rinsed thoroughly with distilled water and hot air dried. The specimens were then stored in a desiccator until

[5] Keller's reagent consists of 1% hydrofluoric acid (HF), 1.5% hydrochloric acid (HCl), 2.5% nitric acid (HNO_3) and 95% distilled water (H_2O) [124].

immersion. Before immersion, the dimensions of the specimens were measured with 3 significant figures and weighed to 5 significant figures.

3.3.5 Electrochemical measurements

For the electrochemical tests the same embedded rectangular specimens were used as for the optical microscopy and microhardness measurements. Since the surfaces of these specimens were indented after the microhardness tests, these surfaces were wet ground again such that the indentations were ground down. The same polishing procedures as for the microhardness measurements were applied up to 3 μm for the electrochemical measurements. After each set of electrochemical measurements on a location was finished, the whole surface was cleaned with distilled water and Isopropanol and then polished to 3 μm again, before the next set of electrochemical measurements was performed on another location. When necessary, the surface was wet ground with grit 2000 and 4000 before polishing.

3.4 Microstructural characterisation

3.4.1 Optical microscopy

The microstructure of the welds was characterised using optical microscopy. After sanding, polishing and etching the specimens according to the procedures in section 3.3.1, micrographs were taken of the etched surfaces using a Keyence VHX-5000 Digital Microscope at the TU Delft and a Union Versamet 3 microscope running on Olympus Stream software at Fokker Aerostructures BV. The Keyence was used to stitch multiple images together to create an overview of the weld zones for each of the three weld specimens. Using this overview, the width of the weld zones was determined by the measuring tool of the Keyence software. The Union Versamet 3 was used to make detailed images of individual weld zones. These images were then analysed using Fiji (ImageJ) software in order to determine the average grain size per weld zone. This was done by overlaying a square grid of at least 5x5 lines on top of the image and counting the intersections of each line with a grain boundary. For images at 50x magnification, the grid size was set to 10000 μm^2, whereas the grid size was set to 1000 μm^2 for images at 200x magnification. Then, the length of the line (determined by using the scale of the image) was divided by the amount of intersections, resulting in an average grain size in that direction for that line. Next, these averages were added together and divided by the amount of lines in that direction to determine the average grain size in that direction for the whole image. This was done for LT and ST directions.

3.4.2 Microhardness measurements

Microhardness measurements were performed using a Struers Durascan Automatic Hardness tester. Three lines of indentations were made with Vickers 0.2 kgf ($HV_{0.2}$): one at the face, centre and root of the cross-section of the welds. Starting from the top left of the LT-ST surface at 0.4 mm away from the edges, indentations were made from left to right at 0.4 mm away from another, then went down one row for the centre line, where indentations were made from right to left. The final row at the root was then made from left to right again. For the 1.6 mm specimens, the distance between rows was 0.4 mm, whereas the distance between rows for the 3.2 mm specimen was 1.2 mm, to ensure the face and root lines were still 0.4 mm away from the edges of the surface. Indentations were then automatically photographed at 10x magnification, from which the microhardness was automatically calculated using Ecos workflow software. Finally,

contour maps with corresponding microhardness profiles per weld were made with Origin software. These contour maps and profiles were then compared to the optical micrographs of the overview of the welds, to help identify the location of each weld zone. Figure 21 shows the grid pattern of the indentations for the 1.6 mm Alclad weld.

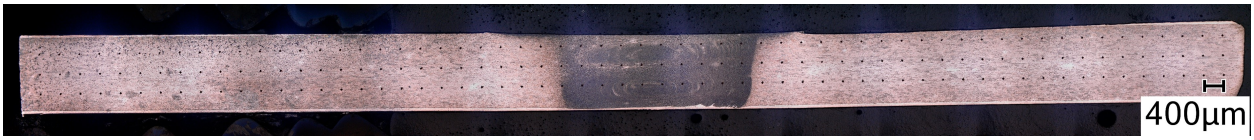

Figure 21: *Microhardness indentations along the LT-ST weld cross-section of the embedded 1.6 mm Alclad specimen. The RS is on the left and the AS is on the right.*

3.5 Tensile and corrosion testing

3.5.1 Tensile tests

Tensile testing was done using an Instron 5500 R with 5000 kgf wedge grips and a 100 kN loadcell. Three configurations per welded sheet were tested:

1) Uncorroded subsize specimen with only base material
2) Uncorroded sheet-type specimen with weld in the middle of the gauge length
3) Corroded sheet-type specimen with weld in the middle of the gauge length

Three specimens were tested per configuration in order to take averages. Specimens were gripped upright and centred by hand, after which an extensometer with a gauge length of 10 mm was placed in the middle of the reduced parallel section using rubber bands (O-rings). Welded specimens were placed with the weld perpendicular to the test direction and the retreating side pointing upwards. Two extensometers with a gauge length of 10 mm were placed on the specimen, one across the weld itself and one on the base material of the advancing side within the reduced parallel section, shown in Figure 22a. The specimens' dimensions were measured prior to testing using a Manutan calliper and entered in the software of the Instron 5500 R, named Bluehill 3. Before the tests started, a pretest was run in which 500 N was applied to the welded specimens and 250 N to the base material specimens. All specimens were tested with a crosshead speed of 1 mm/min until fracture occurred. The extensometer on the weld was taken off after 1% strain was measured across the weld. Tensile stress and strain data were recorded digitally. The marked gauge lengths of the specimens were measured using a Manutan calliper before and after fracture to determine the elongation (el), which is expressed in max strain %. The ultimate tensile strength (UTS) was calculated automatically in Bluehill 3 and confirmed in Excel. Then, the averaged UTS and el of the uncorroded BM specimens were compared to the UTS provided by the suppliers to validate the test method, after which the former were compared to UTS and el of the uncorroded weld specimens to determine the effect of welding on the mechanical properties. Finally, the averaged UTS and el of the corroded weld specimens were compared to those of the uncorroded weld specimens to determine the influence of corrosion damage on the mechanical properties.

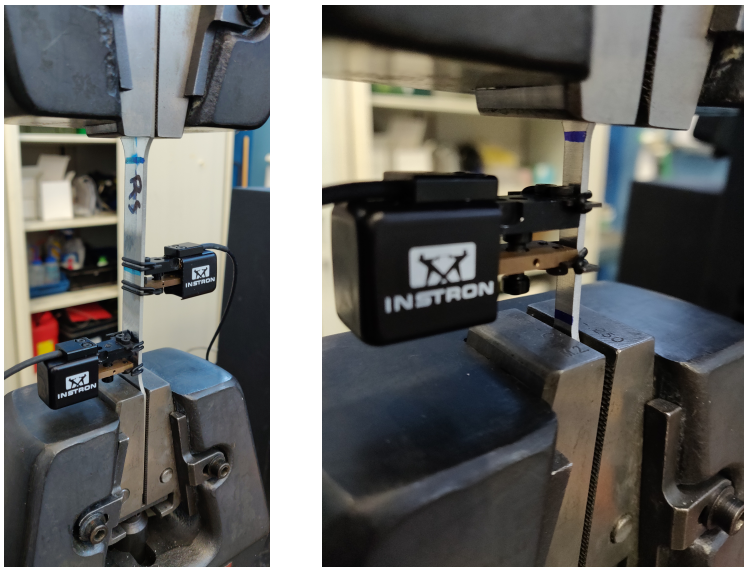

(a) (b)

Figure 22: *Setup for tensile tests. (a) Weld specimens (with RS on top). (b) Base material only specimens.*

3.5.2 Immersion tests

Per welded sheet, three tensile test specimens and one rectangular specimen were fully immersed vertically for 24 hours in open air aerated 3.5% (0.6 M) NaCl solution (T=17.6 °C) with a pH of 5.42 using inert plastic clamps (Struers MultiClips) to hold them upright, shown in Figure 23. The solution was made by solving 158 gram NaCl in 4.5 L distilled water (Milli-Q) in a 5 L beaker. Before immersion, the tensile test specimens were only rinsed with isopropanol to keep the markings on the gauge length, however the rectangular specimens were also cleaned in an ultrasonic bath for 5 minutes. The specimens' dimensions were measured up to 4 significant digits using a Manutan calliper and were weighed up to 5 significant digits using a Sartorius Practum 124-1s Analytical Balance with a readability of $\pm$ 0.1 mg. After 24 hours of immersion, all specimens were taken out of the solution, rinsed with distilled water and then rinsed with isopropanol. The specimens were measured and weighed again, after which only the three rectangular specimens were put in an ultrasonic bath for 20 minutes. These three specimens were then weighed again, after which this process was repeated three more times. This was done in order to determine the mass loss due to corrosion damage.

The nine tensile test specimens were used in tensile tests to compare the ultimate tensile strength and elongation with those of uncorroded specimens, those procedures are described in section 3.5.1. The weld face and root of the three rectangular specimens were scanned before and after immersion using white light interferometry (WLI) on a Bruker ContourX-100 Optical Profilometer to determine the dimensions of pre-existing weld defects (flash height and void depth and size), the surface roughness, and the dimensions and density of corrosion pits. The WLI mode was set to vertical scanning interferometry and scans were made 15 μm above the focus level down to 160 μm below the focus level, with a threshold of 1 % at 5x speed before immersion and 3x speed after immersion for better accuracy. Each scan was performed 3 times for average values. Green light was used, which was set on auto intensity. The full length (20 mm) and width (6-12 mm) of the visible weld area on both the face and root of the rectangular specimens were scanned at 2.5x magnification. These full length scans were used to determine the dimensions of pre-existing weld

defects (flash height and void depth and size), the surface roughness and density of corrosion pits. Smaller areas of variable sizes were also scanned on both flash and root at 20x to 50x magnification, to help scan the size and depths of smaller pre-existing voids and corrosion pits. Gwyddion 2.60 SPM data analysis software was used to process and analyse the data.

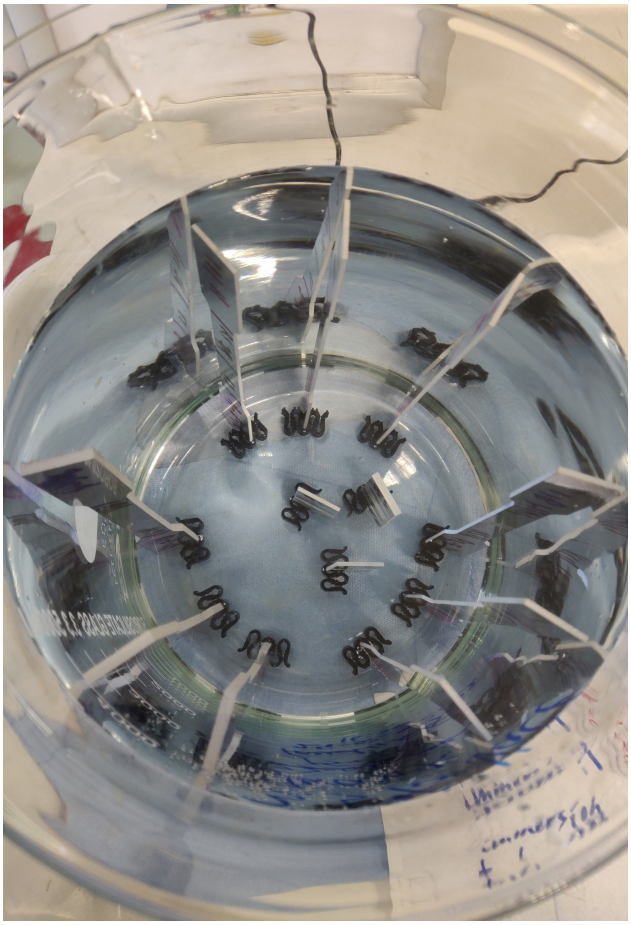

Figure 23: *Setup for continuous immersion of the tensile test specimens and the rectangular specimens. Specimens were immersed for 24 hours in 3.5% NaCl solution.*

3.5.3 Electrochemical measurements

Electrochemical measurements were performed on the embedded rectangular specimens, which were used earlier for optical microscopy and microhardness tests. Before testing, the exposed surface of each specimen (containing the weld cross-section) was prepared according to the procedures mentioned in section 3.3.5. Next, the bottom of the embedded specimens were wet ground in order to expose the bottom part of the weld cross-section, to which a copper tape was adhered, to make an electrical circuit with the embedded specimen possible. Then, green tape was adhered to the top part of the weld cross-section, from which a circular area with a diameter of 1 mm was cut, such that only this small area would be exposed to the test solution. Tests were performed at several locations on the top part of the weld cross-section, such that each weld zone was tested at least once. The locations of these weld zones were based on the

microstructural characterisation performed earlier. Figure 24 shows a schematic of the prepared specimen and the test locations.

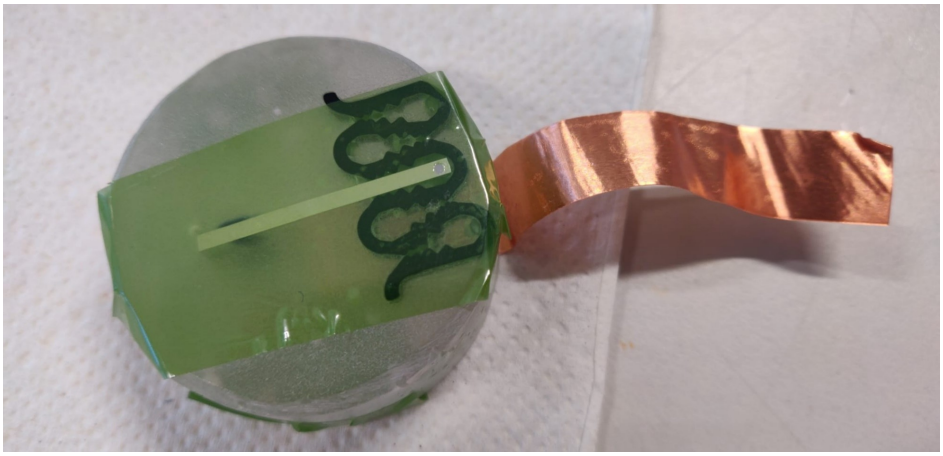

(a)

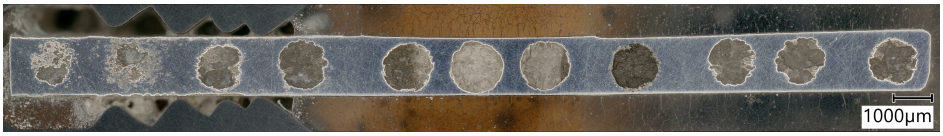

(b)

Figure 24: *(a) A prepared sample of an embedded rectangular specimen to which green tape (with a 1 mm extruded hole) and copper tape are adhered. The top surface is the LT-ST cross-section of the weld. (b) Test locations on the weld cross-section, with the RS on the left and the AS on the right of the image.*

The prepared samples were mounted individually inside a custom electrochemical cell, which was then filled with 100 mL 3.5% NaCl solution. A stainless steel mesh counter electrode and Standard Calomel Electrode (SCE) reference electrode were placed inside the solution and connected to a Biologic VSP-300 potentiostat using clamps and cables. The electrical circuit was closed by connecting the copper tape to the potentiostat, such that the specimens were the working electrode. The setup of this electrochemical cell is shown in Figure 25. Three cells were used simultaneously; one for the 1.6 mm bare specimen, one for the 1.6 mm Alclad specimen and one for the 3.2 mm Alclad specimen.

Testing began once the electrochemical cells were set up. Four measurements were done back-to-back per location: First, the open circuit potential (OCP) was measured every second for 1 hour. Then, the linear polarisation resistance (LPR) was measured from -30 mV to +30 mV with respect to OCP at a rate of 10 mV/min, after which OCP was measured again for 5 minutes to stabilise the test. Finally, potentiodynamic polarisation was applied from -250 mV to +1V with respect to OCP at a rate of 0.5 mV/s.

After the tests were finished on one location (Figure 24b), the electrochemical cells were emptied and rinsed with distilled water, and the green tape was removed from the top surface of the samples. These surfaces were then rinsed with distilled water and wet ground such that tape residue was removed but corrosion damage was still visible. Then, the specimens were masked again with the green tape, such that the exposed area was placed on the next location. The samples were then mounted again in the electrochemical cell. The solution was refreshed and with the electrodes

reconnected the next cycle of tests were run. After testing all locations on a specimen, an optical micrograph was made of the top surface using a Keyence (resulting in Figure 24b). Then, the surface was wet ground and polished such that all corrosion damage was removed and a smooth surface was available. The tests were then repeated again, starting from the first location to the last. This cycle of testing was performed three times in total to determine the repeatability of the results.

Figure 25: *Setup of the electrochemical cell, in which the red wire is connected to the working electrode via the copper tape, the white wire is connected to the SCE reference electrode and the blue wire is connected to the stainless steel counter electrode. The solution consists of 3.5 gram NaCl solved in 100 mL distilled water, and the exposed surface area is a circle with a 1 mm diameter.*

The data was collected and analysed with EC-lab V11.36 software. OCP values were determined per round by averaging the measured potential at 50, 55 and 60 minutes. These values were then averaged again for the three repeated tests to determine the OCP value per test location per weld. The corrosion resistance or polarisation resistance (R_p) was determined by taking the slope of the LPR data around the equilibrium potential (OCP), as shown in Figure 17. The R_p values were then also averaged per location over the three rounds of tests performed. Finally, tafel plots were created from the poteniodynamic polarisation tests, from which tafel slopes were placed on the cathodic and anodic polarisation curves near the equilibrium potential. The X and Y coordinates of the point of intersection of these tafel slopes were used to determine the corrosion current density (i_{corr}) and corrosion potential (E_{corr}), respectively. The pitting potential (E_{pit}) was determined by the potential at which the current density increased immensely (almost horizontal line). The i_{corr}, E_{corr} and E_{pit} values were also averaged per location over the three rounds of test performed.

4 Results

4.1 Microstructural characterisation

4.1.1 Macrostructure of weld cross-section

Figure 26: *Stitched optical micrographs at 200x magnification showing the macrostructure of the weld cross-sections in LT-ST plane. The NZ, TMAZ and HAZ are indicated accordingly, the BM is outside of these images. (a) 1.6 mm bare sheet. (b) 1.6 mm Alclad sheet with cladding hand abraded from face. (c) 3.2 mm Alclad sheet with cladding machined from face.*

Figure 26 shows the macrostructure of the weld cross-sections. In all three specimens there is a clear distinction between the NZ and the TMAZ and HAZ on the advancing side (AS), whereas there is a more gradual transition of the microstructure on the retreating side (RS). The welds are very symmetric along the long transverse direction for the 1.6 mm specimens. However, the transition of the weld zones on the RS is more gradual in the 3.2 mm specimen, which reduces symmetry. Next, onion rings are visible in the NZ of all specimens: Double stacked elliptical shaped rings are

present in the 1.6 mm specimens, whereas triple stacked distorted rings are present in the 3.2 mm specimen. The NZ of both 1.6 mm specimens is 6.4 mm wide at the top and 3.4-3.5 mm wide at the bottom.The 3.2 mm specimen has a NZ which is 9.5 mm wide at the top and 2.9 mm wide at the bottom of the weld.The TMAZ of the 1.6 mm bare specimen is 163 μm wide on the RS and 146 μm on the AS, whereas the TMAZ of the 1.6 mm Alclad specimen is 132 μm and 110 μm wide on the RS and AS, respectively. The TMAZ of the 3.2 mm Alclad specimen is larger than those of the 1.6 mm specimens, namely 356 μm wide on the RS and 148 μm to 1.19 mm wide on the AS. The width of the HAZ was determined by the microhardness measurements in section 4.2, which are 7 mm and 6 mm for the RS and AS of the 1.6 mm bare specimen, respectively. The HAZ of the 1.6 mm Alclad specimen is 6 mm wide on both sides of the weld, and the HAZ of the 3.2 mm Aclad specimen is 8 mm wide on both sides of the weld. Finally, weld thinning of 0.04 mm, 0.02 mm and 0.02 mm was observed in the 1.6 mm bare, 1.6 mm Alclad and 3.2 mm Alclad specimens, respectively.

4.1.2 Microstructure details

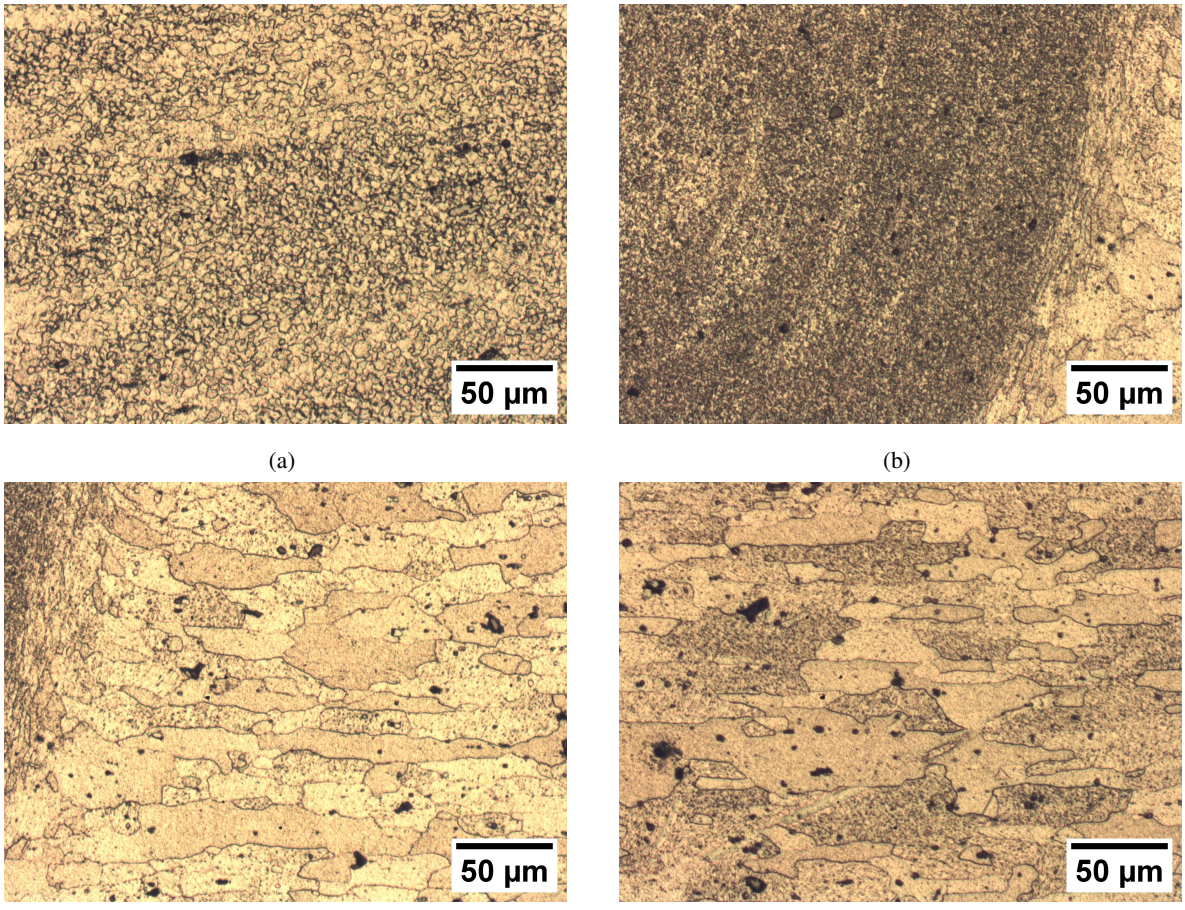

(a) (b)

(c) (d)

Figure 27: *Optical micrographs at 200x magnification in LT-ST plane on the advancing side, showing the grain structure of the (a) nugget zone (NZ), (b) thermo-mechanically affected zone (TMAZ) in between the NZ and the HAZ, (c) heat affected zone (HAZ), and (d) base material (BM).*

Representative close-ups of each weld zone are shown in Figure 27. The average grain size dimensions are presented per weld zone in Table 7. Grains in the BM and the HAZ are elongated in long transverse (LT) direction, whereas the smaller grains in the TMAZ are rotated upwards towards the NZ in short transverse (ST) direction. A gradient in rotation of the grains is visible between the HAZ and TMAZ on the RS and AS of all specimens. The NZ consists of rounded, fine equiaxed grains, with a length of 5±1 μm in both ST- and LT-directions. The length of the grains in the BM of the 1.6 mm bare and 3.2 mm Alclad specimens are 18±3 μm in ST-direction and 42±10 μm in LT-direction. The size of the grains in the BM of the 1.6 mm Alclad specimen seemed inconsistent with the other specimens, as these grains are twice the size in both directions: 34±5 μm in ST-direction and 82±28 μm in LT-direction. The length of the grains in the HAZ are 18±3 μm in ST-direction for both the 1.6 mm bare and 3.2 mm Alclad specimens, and 37±9 μm and 48±18 μm in LT-direction. The length of the grains in the HAZ of the 1.6 mm Alclad specimen is 26±5 μm and 50±11 μm in ST- and LT-directions respectively. The length of the grains in the TMAZ are 15±3 μm in ST-direction and 13±3 μm in LT-direction for the 1.6 mm bare specimen, 14±2 μm in ST-direction and 16±4 μm in LT-direction for the 1.6 mm Alclad specimen and 10±1 μm in ST-direction and 20±5 μm in LT-direction for the 3.2 mm Alclad specimen.

Table 7: *Average grain size and standard deviation (SD) in short transverse (ST) and long transverse (LT) directions in the weld zones of the three specimens.*

		Zones													
		BM-RS		**HAZ-RS**		**TMAZ-RS**		**NZ**		**TMAZ-AS**		**HAZ-AS**		**BM-AS**	
Specimen	**Direction**	**Mean (μm)**	**SD (μm)**	**Mean (μm)**	**SD (μm)**	**Mean (μm)**	**SD (μm)**	**Mean (μm)**	**SD (μm)**	**Mean (μm)**	**SD (μm)**	**Mean (μm)**	**SD (μm)**	**Mean (μm)**	**SD (μm)**
1.6 mm	ST	17	2	17	3	15	3	-	-	15	1	19	2	19	3
bare	LT	36	4	33	4	15	3	-	-	10	1	39	10	49	9
1.6 mm	ST	32	6	24	1	14	2	-	-	-	-	27	6	36	5
Alclad	LT	69	19	50	9	16	4	-	-	-	-	51	12	95	30
3.2 mm	ST	17	2	19	1	-	-	5	1	10	1	16	1	16	2
Alclad	LT	41	5	63	13	-	-	5	1	20	5	33	7	44	8

Figure 28 shows several micrographs of defects located in the welds. On all three specimens a flash is visible on both sides of the weld, the average height of the flash is reported in section 4.4. The thickness of the cladding on the bottom of the Alclad specimens is 47 μm and 66 μm in the BM of the 1.6 mm and 3.2 mm specimens respectively. The thickness of cladding has decreased in the NZ of both specimens. Several flow arms of cladding are visible, with a maximum length of 114 μm and 339 μm in ST-direction for the 1.6 mm and 3.2 mm specimens, respectively. Several small grains with a similar colour as the cladding are distributed in the NZ of the Alclad specimens. Black spots in Figure 28a may indicate etched out IMPs, similar spots are also visible in Figure 27c and Figure 27d.

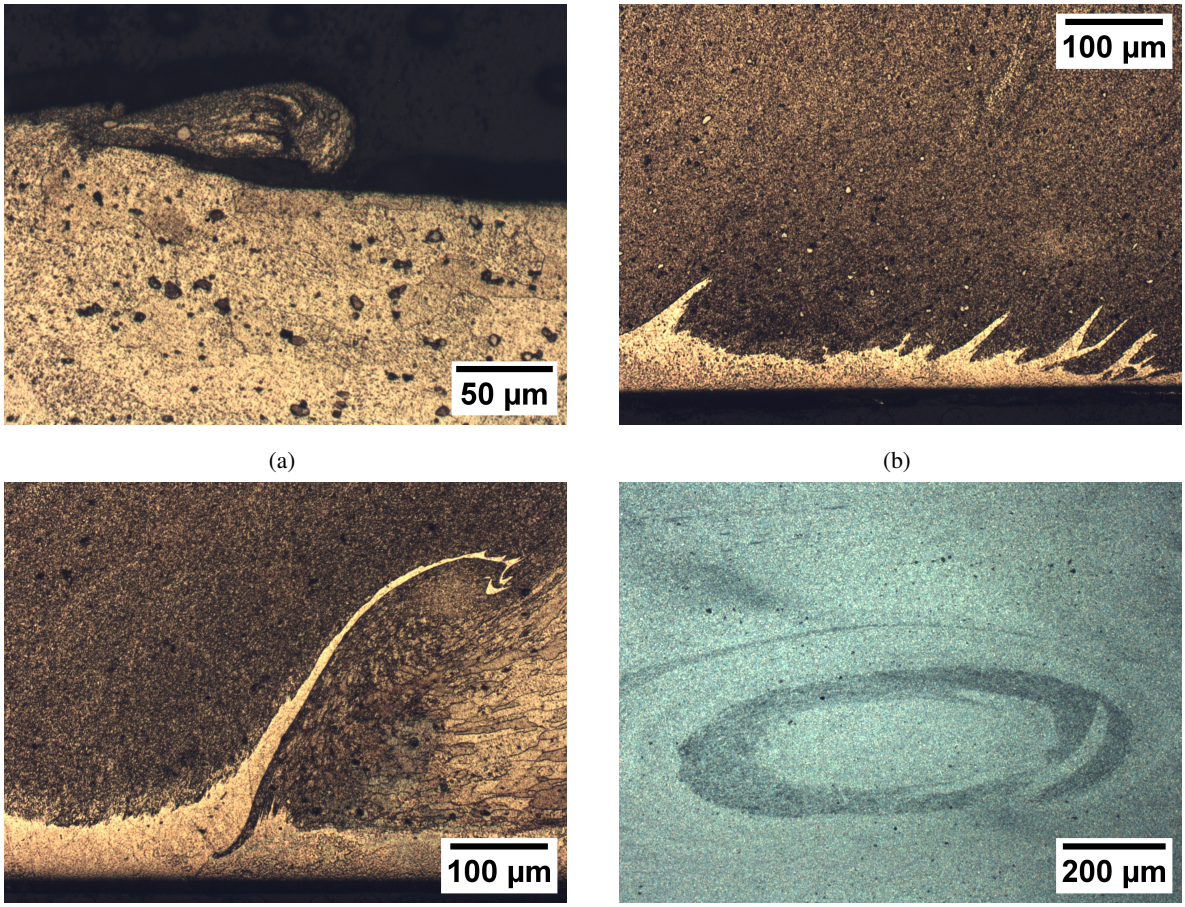

(a) (b)

(c) (d)

Figure 28: *Optical micrographs at 50-200x magnifications showing microstructural details of the welds, including (a) flash (b) cladding in NZ of 1.6 mm specimen, (c) cladding in NZ of 3.2 mm specimen and (d) onion rings (in Dark Field).*

4.2 Microhardness profiles

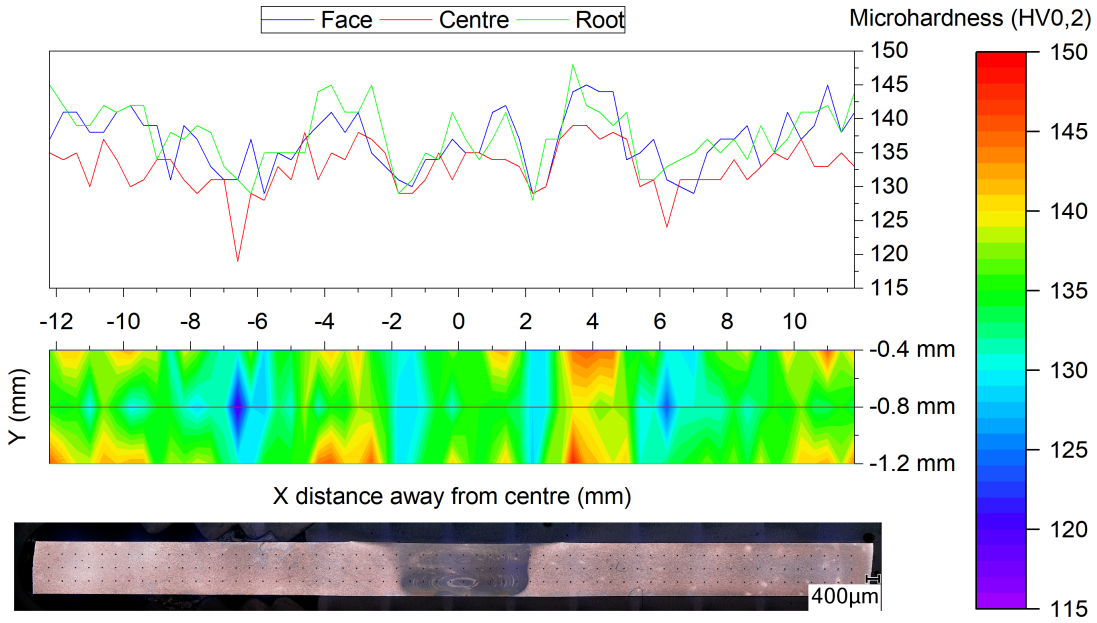

Figure 29: *Contour map of the microhardness along the weld cross-sections of the 1.6 mm bare specimen. Corresponding microhardness profiles and weld macrostructure are displayed above and below the contour map, respectively.*

Contour maps of the microhardness along the weld cross-sections are shown in Figure 29 to Figure 31. A notable change in microhardness is observed between each weld zone of the 1.6 mm specimens. First, an average microhardness of 138 $\pm$ 4 $HV_{0.2}$ was observed in the BM of the 1.6 mm bare specimen on both sides of the weld. A small drop in microhardness was observed in the HAZ, which was on average 135 $\pm$ 4 $HV_{0.2}$ on the RS and 136 $\pm$ 5 $HV_{0.2}$ on the AS. The microhardness dropped even further in the TMAZ, in which an average of 130 $\pm$ 1 $HV_{0.2}$ was observed on the RS and 129 $\pm$ 0 $HV_{0.2}$ on the AS. The microhardness increased again in the NZ, in which an average of 135 $\pm$ 3 $HV_{0.2}$ was observed.

A similar microhardness evolution was observed in the 1.6 mm Alclad specimen: An average of 140 $\pm$ 3 $HV_{0.2}$ was observed in the BM on both sides of the weld, while a small drop to 136 $\pm$ 5 $HV_{0.2}$ was observed in the HAZ on both sides of the weld. Again, a further drop in microhardness (to 130 $\pm$ 4 $HV_{0.2}$) was observed in the TMAZ, while an increase to 134 $\pm$ 3 $HV_{0.2}$ was observed in the NZ. However, the lowest microhardness of around 126 $HV_{0.2}$ was measured in the TMAZ of the 1.6 mm Alclad specimen, whereas the lowest microhardness of around 124 $HV_{0.2}$ was observed in the HAZ on the RS of the 1.6 mm bare specimen. In the HAZ of both specimens, a varying microhardness depending on location was observed in the HAZ, ranging from 124 to 148 $HV_{0.2}$. Finally, a maximum microhardness of 148 $HV_{0.2}$ was observed in the BM and HAZ of both specimens.

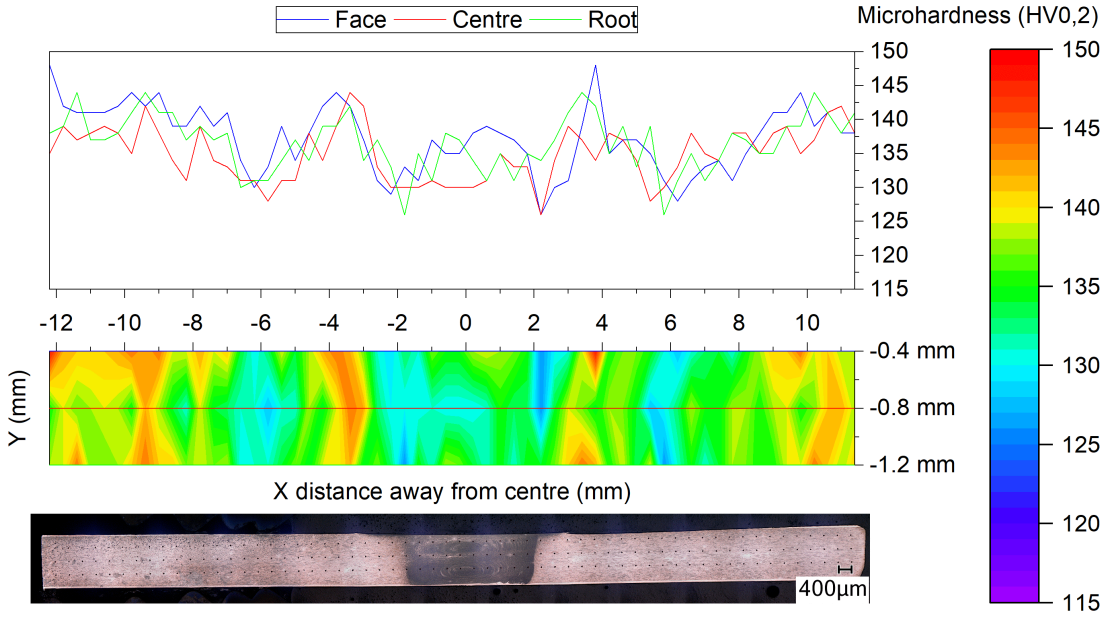

Figure 30: *Contour map of the microhardness along the weld cross-sections of the 1.6 mm Alclad specimen. Corresponding microhardness profiles and weld macrostructure are displayed above and below the contour map, respectively.*

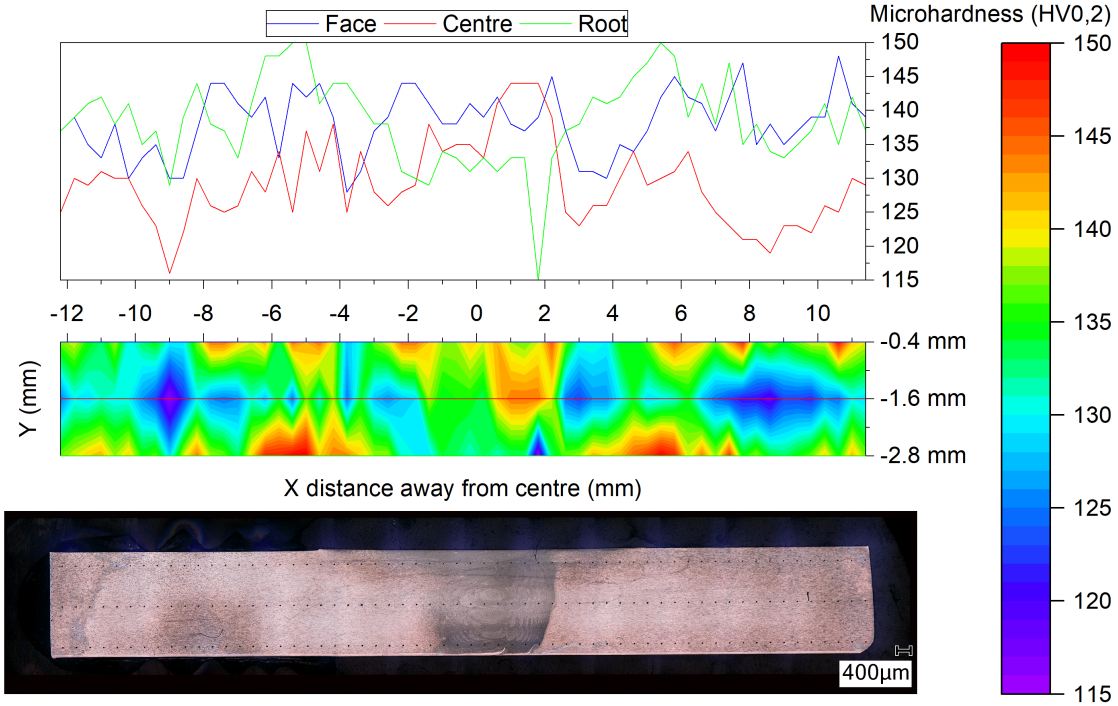

Figure 31: *Contour map of the microhardness along the weld cross-section of the 3.2 mm Alclad specimen. Corresponding microhardness profiles and weld macrostructure are displayed above and below the contour map, respectively.*

Next, some strange phenomena were observed in the 3.2 mm specimen: Measurements done along the centre line (at -1.6 mm below the top surface) showed notable lower microhardness compared to the face and root profiles, as is evident in Figure 31. Larger areas of lower microhardness were observed in the HAZ in mid thickness. Due to this low microhardness along the mid-thickness of the sheet, lower averages were observed for the BM (134 $\pm$ 5 $HV_{0.2}$ for RS and 135 $\pm$ 7 $HV_{0.2}$ for AS) than in the HAZ (136 $\pm$ 8 $HV_{0.2}$ for RS and 135 $\pm$ 8 $HV_{0.2}$ for AS). Furthermore, a higher average microhardness of 134$\pm$ 7 $HV_{0.2}$ was observed in the TMAZ on the RS and 139 $\pm$ 5 $HV_{0.2}$ on the AS. However, an average microhardness of 136 $\pm$ 5 $HV_{0.2}$ was observed in the NZ, which is somewhat similar to the average microhardness of the NZ of the 1.6 mm specimens. Moreover, the lowest microhardness of 115 $HV_{0.2}$ was observed in the root of the NZ, which was located on a flow arm of the cladding mixed into the NZ. Finally, a maximum microhardness of 150 $HV_{0.2}$ was observed in the HAZ.

4.3 Tensile test results

4.3.1 Tensile strength and elongation

The average ultimate tensile strength (UTS) of the uncorroded base material specimens, uncorroded weld specimens and corroded weld specimens are shown in Figure 32a. First, the UTS of the 1.6 mm bare sheet in LT-direction is 471 $\pm$ 2 MPa before welding, which is similar to the UTS reported by the supplier (section 3.1.1). An average UTS of 456 $\pm$ 1 MPa was observed for the welded specimens, which is a weld efficiency of 96.8%. The UTS of the corroded weld specimens is slightly higher at 460 $\pm$ 1 MPa. Second, an average UTS of 417 $\pm$ 2 MPa was observed for the 1.6 mm Alclad sheet in LT-direction, which is 21 MPa lower than the UTS reported by the supplier. A higher average UTS of 424 $\pm$ 6 MPa was observed for the uncorroded weld specimens, which would mean a weld efficiency of 101.7% was achieved. Furthermore, an average UTS of 432 $\pm$ 5 MPa was observed for the corroded weld specimens, which is a further increase in strength of 8 MPa. Reasons as to why these phenomena may have occurred are discussed in section 5.1.2. Third, the UTS of the 3.2 mm Alclad sheet in LT-direction is 440 $\pm$ 1 MPa, which is 13 MPa lower than the UTS reported by the supplier. An average UTS of 422 $\pm$ 1 MPa was observed for the welded specimens, which is a weld efficiency of 95.9%. Finally, the UTS of the corroded weld specimens was determined to be 423 $\pm$ 6 MPa, which is again slightly higher than the UTS of the uncorroded weld specimens.

The average elongation of the gauge length of the tensile specimens, which was measured after fracture and is expressed in max strain percentage, is shown in Figure 32b. The average elongation of the uncorroded BM of the 1.6 mm bare sheet was 22.3 $\pm$ 0.7 % on average, whereas a smaller elongation of 14.2 $\pm$ 0.3 % was observed for the uncorroded weld specimens, resulting in a weld efficiency of 63.7%. The corroded weld specimens showed an even lower elongation of 11.2 $\pm$ 0.4 %. Next, an elongation of 17.6 $\pm$ 1.1 % was observed for the uncorroded BM of the 1.6 mm Alclad sheet. With an average elongation of 7.4 $\pm$ 0.6 %, a weld efficiency of 42.0% was achieved for the uncorroded weld specimens. Interestingly, a somewhat larger elongation was achieved on achieved for the corroded weld specimens (8.0 $\pm$ 0.0 %). Similar phenomena are observed in the 3.2 mm Alclad sheet, where a much larger elongation (21.9 $\pm$ 0.5 %) was observed in the uncorroded BM specimens than in the welded specimens: 7.1 $\pm$ 0.3 % and 7.2 $\pm$ 0.2 % for the uncorroded and corroded weld specimens respectively. The drop in elongation between unwelded and welded material results in a weld efficiency of only 32.4% for the 3.2 mm Alclad welds.

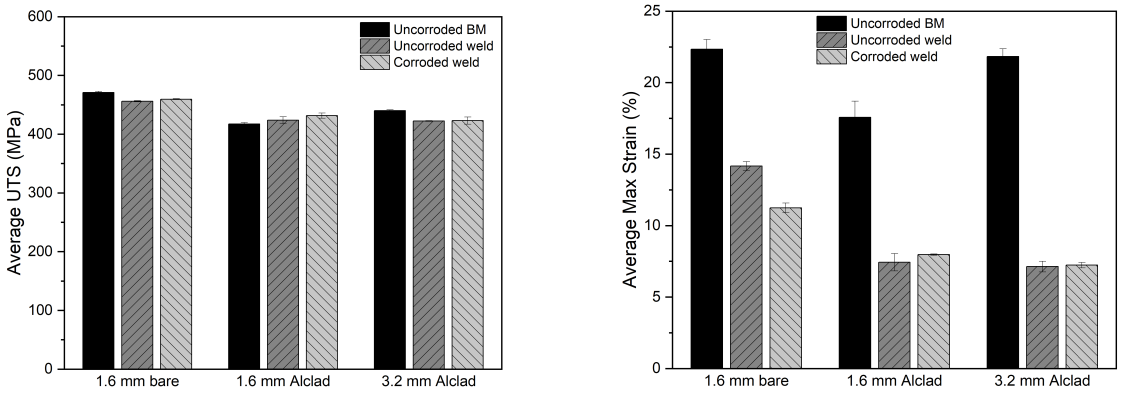

(a) (b)

Figure 32: *Mechanical properties of tensile tested specimens. (a) Average ultimate tensile strength (UTS). (b) Average elongation of the gauge length after fracture (expressed in max strain percentage).*

Finally, the graphs in Figure 32 show that the 1.6 mm bare sheet has the highest tensile properties, and that the welded specimens of the 1.6 mm bare and 3.2 mm Alclad sheets have a slightly lower UTS with respect to their BM. Furthermore, all welded specimens have a considerably lower ductility than their original BM. Next, no change in strength was observed for corroded weld specimens compared to uncorroded weld specimens. Furthermore, no notable change in ductility was observed between corroded and uncorroded Alclad weld specimens. However, the ductility of the corroded weld specimens of the 1.6 mm bare sheet is lower than of the uncorroded weld specimens.

4.3.2 Fracture locations of weld specimens

An overview of the fracture locations of the uncorroded and corroded weld specimens is shown in Figure 33. For all uncorroded weld specimens, the specimens fractured along the weld root on the AS of the weld. Some fracture surfaces are smooth whereas others are pointy. However, the corroded Alclad specimens show more displacement of the crack along the fracture, which is not smooth. Although, the corroded 1.6 mm bare specimen shows similar fracture as the uncorroded weld specimens, even though corrosion pits are observed on the RS as well. Unfortunately, no fractography was done to help determine the type of fracture, nor were any measurements taken regarding area reduction, since that was out of scope of the project. Still, it is noteworthy that all specimens fractured along the weld root on the advancing side, with some small necking visible in the uncorroded weld specimens.

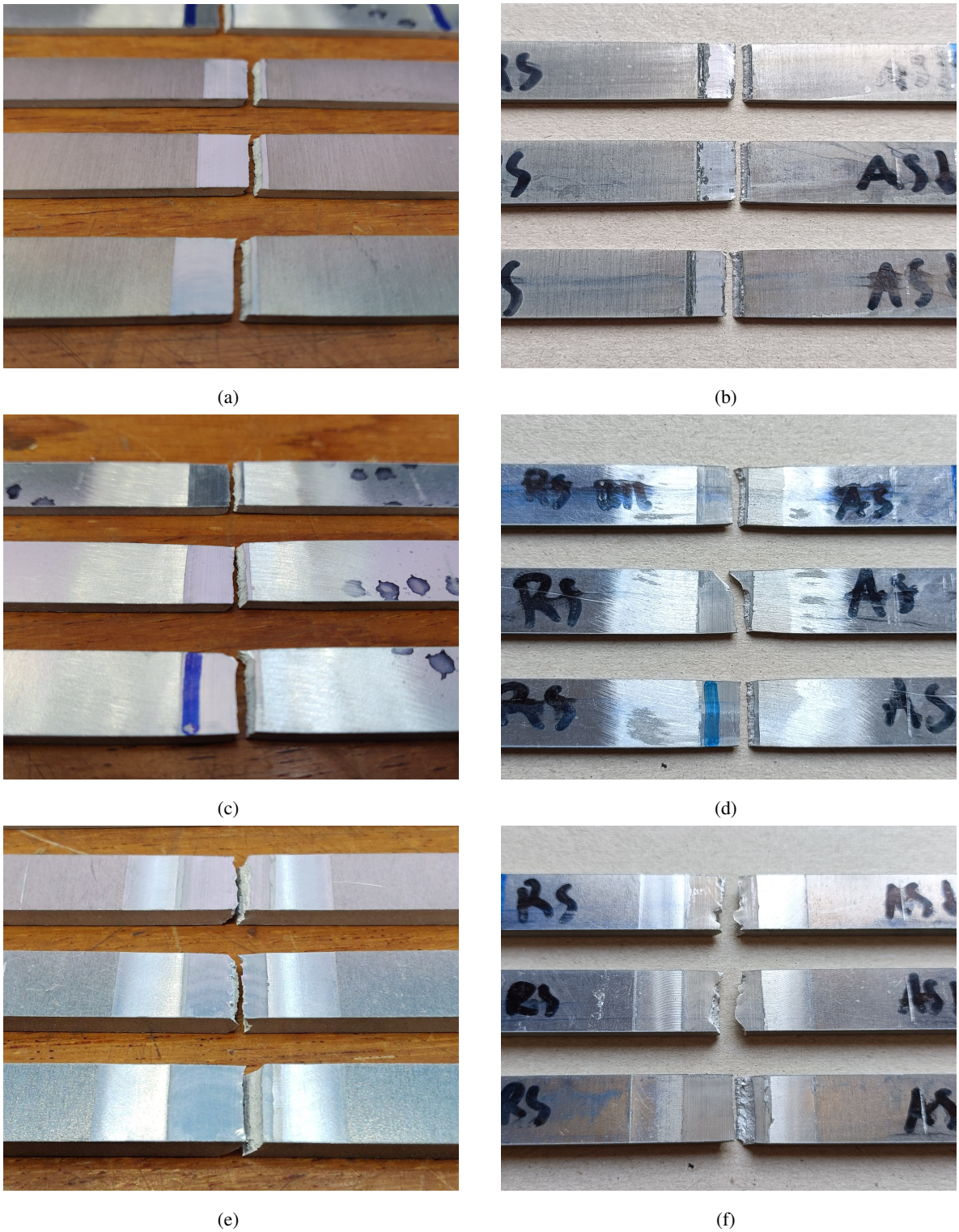

(a) (b)

(c) (d)

(e) (f)

Figure 33: *Fracture locations of fractured uncorroded (left) and corroded (right) weld specimens. The fracture location is along the weld root on the advancing side (AS) for all specimens. (a,b) 1.6 mm bare specimens. (c,d) 1.6 mm Alclad specimens. (e,f) 3.2 mm Alclad specimens. In these images, RS is on the left and AS is on the right, weld tool travelled from top to bottom.*

4.4 Immersion test results

Scans of the top (face) and bottom (root) surfaces of the uncorroded and corroded rectangular specimens were made using white light interferometry (WLI) before and after immersion. The resulting surface maps are presented in Figure 34 to Figure 37, and show the presence of flash on the face and voids in the root of the uncorroded specimens, which are considered weld defects. These defects are reported in section 4.4.1. Corrosion pits are visible on these surface maps as well, these are reported in section 4.4.2. The roughness of these surfaces is presented in 4.4.3 and the mass loss after immersion is presented in section 4.4.4.

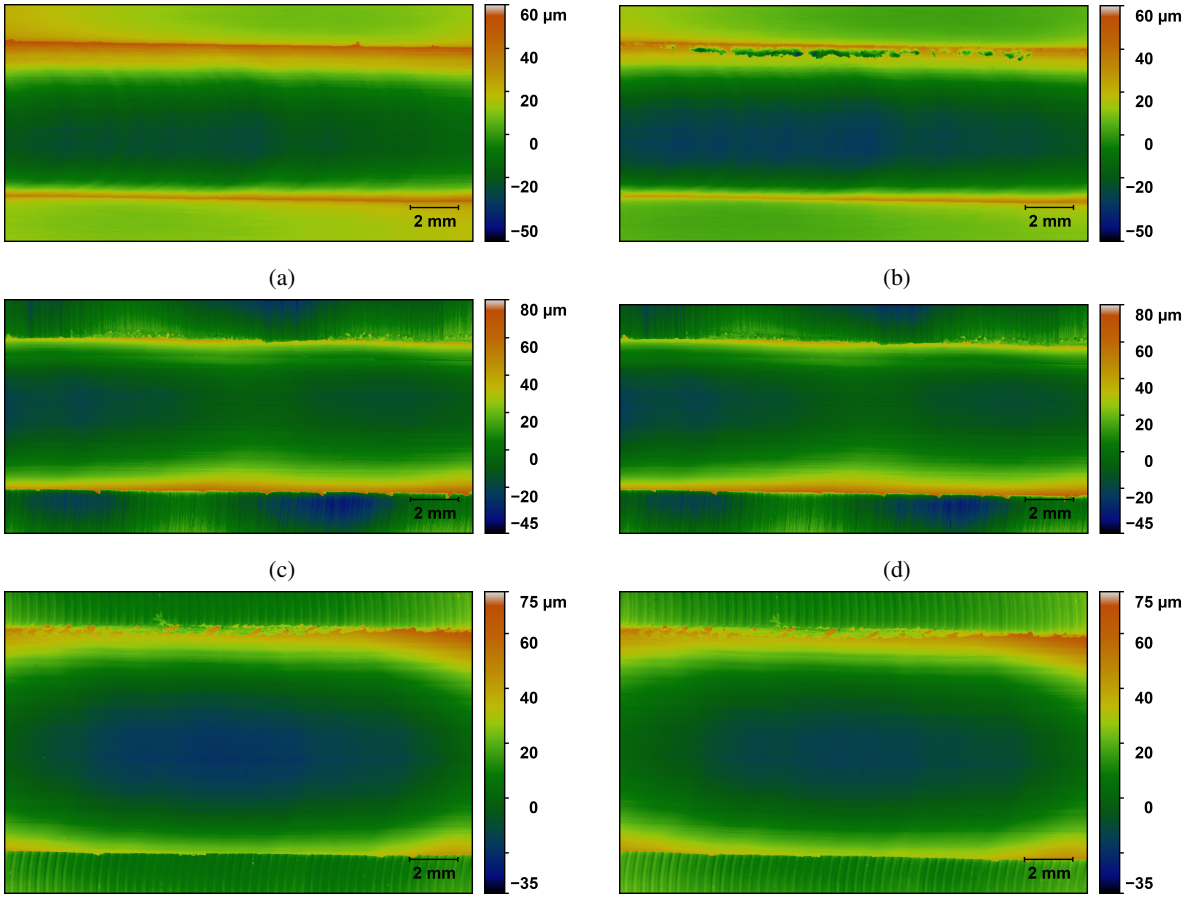

Figure 34: *WLI surface maps of the uncorroded (left) and corroded (right) surfaces of the face of (a,b) 1.6 mm bare specimen, (c,d) 1.6 mm Alclad specimen, (e,f) 3.2 mm Alclad specimen. The top of all images is the RS, the bottom of all images is the AS, with the welding tool having travelled from right to left.*

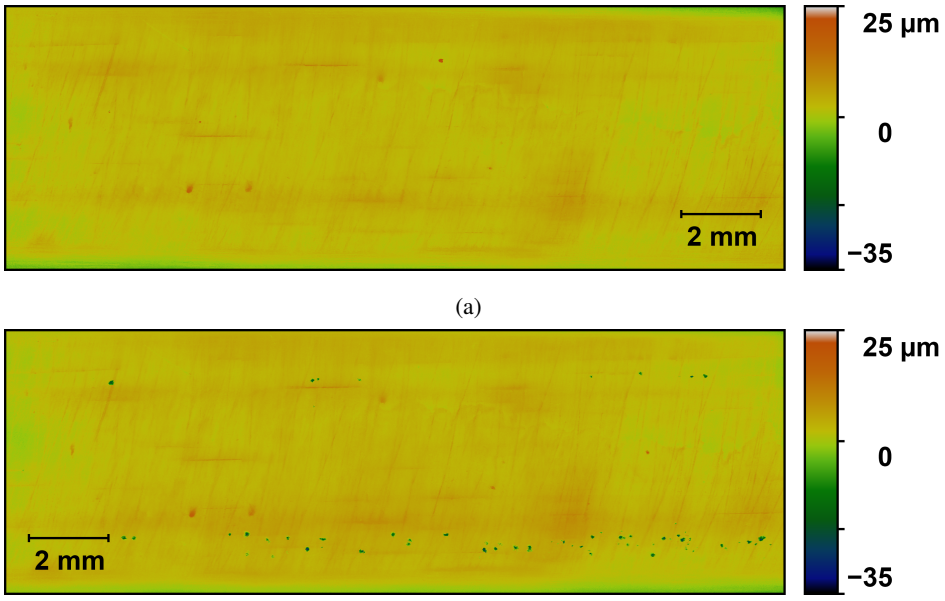

Figure 35: *WLI surface maps of the (a) uncorroded and (b) corroded surfaces of the root of the 1.6 mm bare specimen. The top of these images is the RS, the bottom of these images is the AS, with the welding tool having travelled from left to right.*

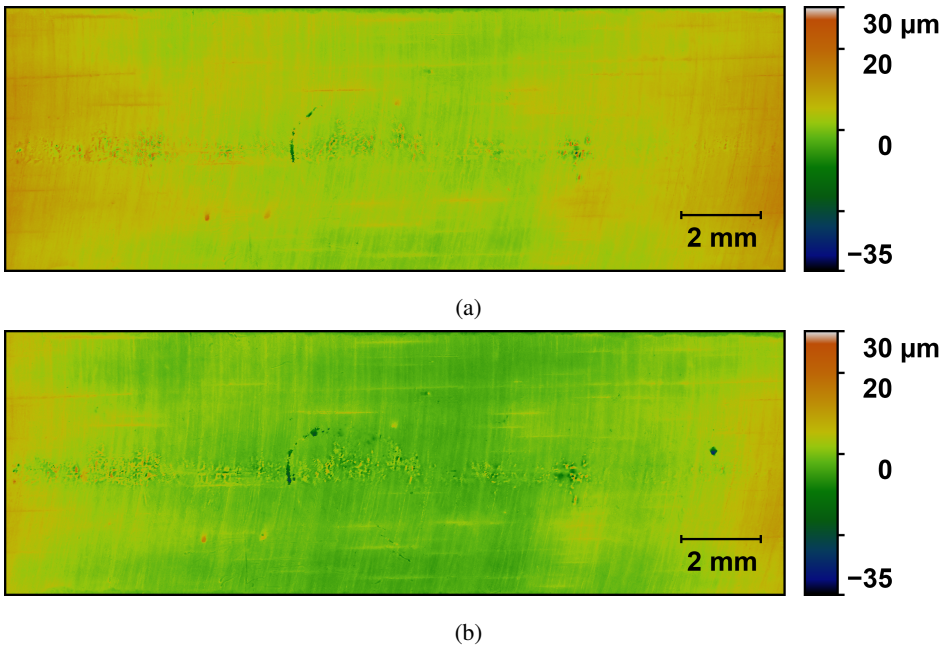

Figure 36: *WLI surface maps of the (a) uncorroded and (b) corroded surfaces of the root of the 1.6 mm Alclad specimen. The top of these images is the RS, the bottom of these images is the AS, with the welding tool having travelled from left to right.*

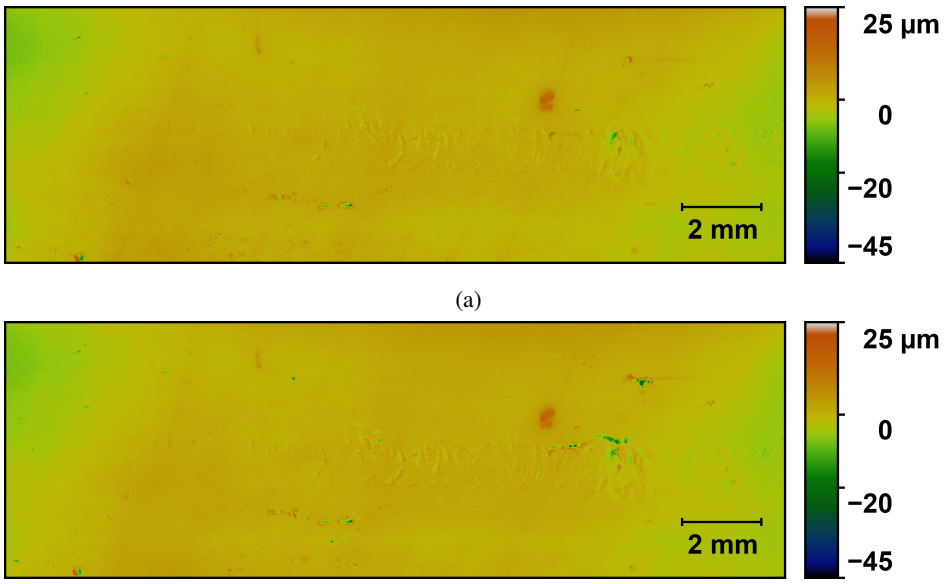

Figure 37: *WLI surface maps of the (a) uncorroded and (b) corroded surfaces of the root of the 3.2 mm Alclad specimen. The top of these images is the RS, the bottom of these images is the AS, with the welding tool having travelled from left to right.*

4.4.1 Pre-existing weld defects prior to immersion

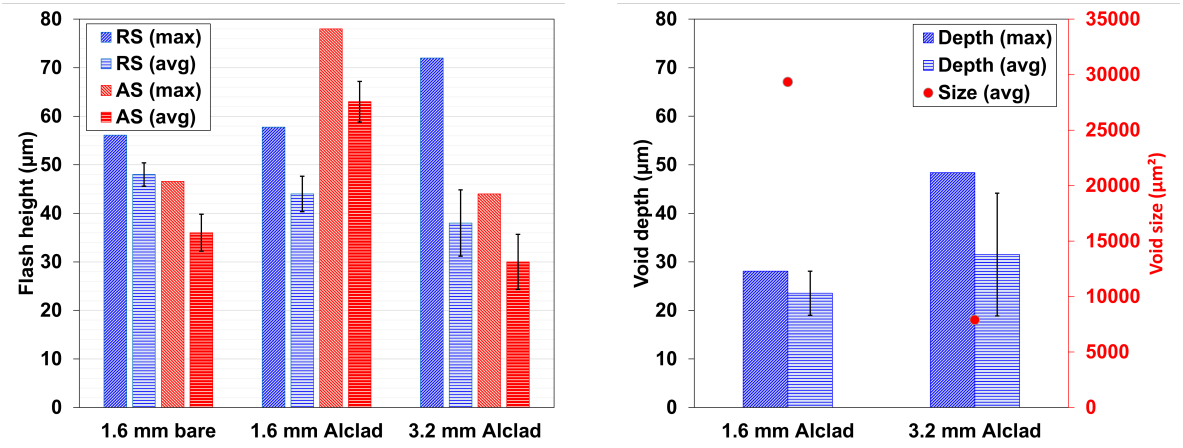

Figure 38: *Dimensions of defects on the face and root of the 1.6 mm bare, 1.6 mm Alclad and 3.2 mm Alclad immersion specimens. (a) Maximum and average height of flash on the face. (b) Maximum and average depth and average size of voids on the root.*

The dimensions of weld surface defects, such as flash on the face and voids on the root of the specimens (Figure 34 to Figure 37), were measured prior to immersion and are presented in Figure 38. The local height of the flash with respect

to the BM on the face of the 1.6 mm bare specimen is on average 48 $\pm$ 2 μm on the RS and 36 $\pm$ 4 μm on the AS, with a maximum of 56 μm located on the RS. For the 1.6 mm Alclad specimen these values are 44 $\pm$ 4 μm and 63 $\pm$ 4 μm for the average height of the flash on the RS and AS respectively, with a maximum of 78 μm located on the AS. Next, the 3.2 mm Alclad specimen has an average flash height of 38 $\pm$ 7 μm on the RS and 30 $\pm$ 6 μm on the AS, with a maximum height of 72 μm on the RS.

The weld roots of the uncorroded Alclad specimens contain large voids, which have an average size of $2.9{\cdot}10^4$ μm^2 and an average depth of 24 $\pm$ 5 μm in the 1.6 mm specimen and an average size of $7.9{\cdot}10^3$ μm^2 and an average depth of 32 $\pm$ 13 μm in the 3.2 mm specimen. No notably large voids were observed in the 1.6 mm bare specimen.

4.4.2 Corrosion pits morphology and statistics

Next, corrosion pits (or pits for short) were discovered on the face and root of the 1.6 mm bare specimen after immersion in 3.5% NaCl for 24 hours, which are visible in Figure 34b and Figure 35b. Pits were not immediately visible on the Alclad specimens, however, more detailed WLI scans of smaller areas at higher magnification reveal the presence of very fine pits on the surfaces of both Alclad specimens. A few examples of the corrosion pits are shown in Figure 39.

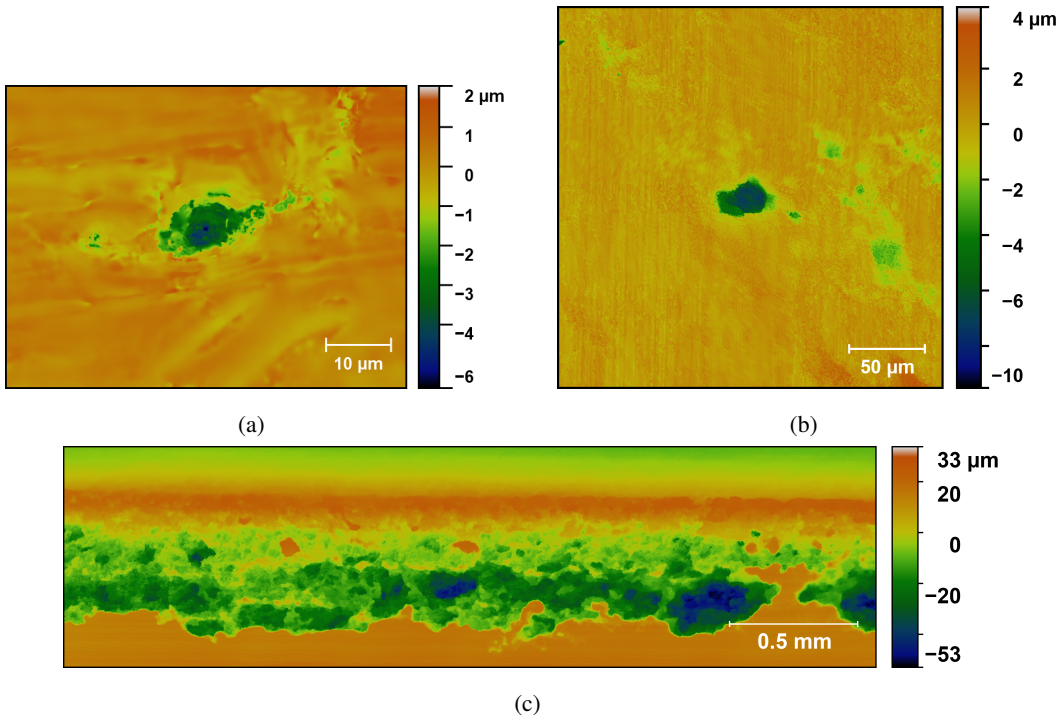

Figure 39: *Surface maps showing corrosion pits on the (a) root of 1.6 mm Alclad specimen, (b) root of the 3.2 mm Alclad specimen, and (c) face of the 1.6 mm bare specimen (on the RS flash).*

All corrosion pits, except for those on the face of the 1.6 mm bare specimen, are circular of shape. The pits on the face of the 1.6 mm bare specimen are elongated in the welding direction (Figure 39c), and are located near the flash on the RS, inside the weld area (2.7 mm away from the weld centre). The pits on the root of the 1.6 bare specimen are located

2.0-2.5 mm away from the weld centre, on the AS. Pits on the roots of the Alclad specimens are spread out randomly, while some formed on and near pre-existing weld defects.

The maximum pit depth, average pit depth, average pit size and pit density are presented per specimen surface in Figure 40. The face of the 1.6 mm bare specimen contains the largest pits, both in depth (86.2 μm) and size ($1.42 \cdot 10^5$ μm^2). The root of the 1.6 bare specimen contains more pits, but are of smaller depth (40.0 μm) and size ($5.63 \cdot 10^3$ μm^2). Less pits were observed on the face of the 1.6 mm Alclad specimen, which are of smaller depth (12.0 μm) and size ($3.07 \cdot 10^2$ μm^2) as well. On the other hand, the root of the 1.6 mm Alclad specimen contains more and larger pits, which are 32.6 μm deep and are $9.76 \cdot 10^3$ μm^2 in size. Finally, only a few small pits of 9.6 μm in depth and $1.93 \cdot 10^2$ μm^2 in size were observed on the root of the 3.2 mm Alclad specimen, and none were observed on the face of this specimen.

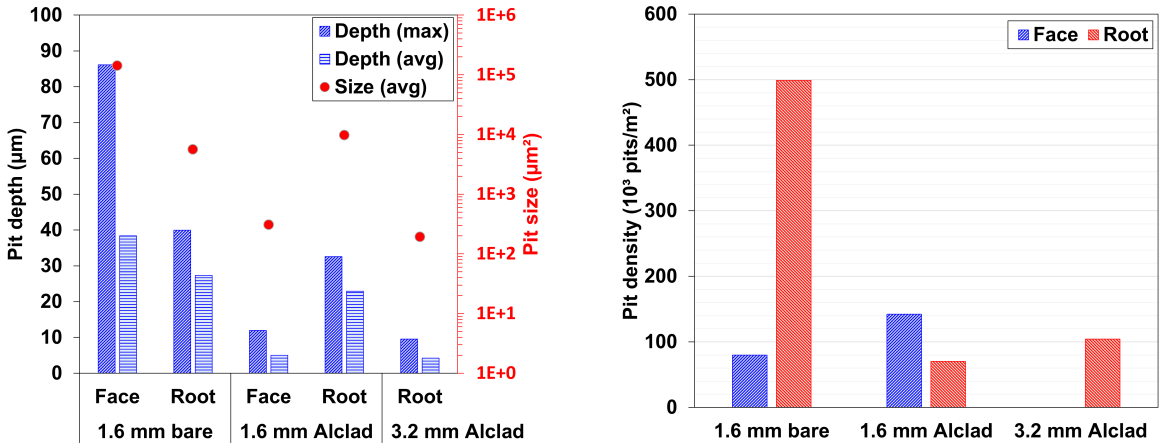

(a) (b)

Figure 40: *Pit statistics of the 1.6 mm bare, 1.6 mm Alclad and 3.2 mm Alclad specimens, showing the (a) dimensions of corrosion pits and (b) pit density (amount of corrosion pits per square meter of weld section).*

4.4.3 Surface roughness

Next to the dimensions of pre-existing weld defects and corrosion pits, the surface roughness parameters of the uncorroded and corroded rectangular specimens were obtained from the WLI surface maps (Figure 34 to Figure 37) as well. The complete set of surface roughness parameters, which includes the arithmetic mean roughness (Sa), skewness (Ssk), area texture kurtosis (Sku), maximum peak height (Sp) and maximum valley depth (Sv), is presented in Table 8. Sa is the average deviation from the mean surface, Ssk is the symmetry between peaks and valleys, Sku is the sharpness of the peaks and valleys, and Sp and Sv are the maximum positive and negative deviation from the mean surface, respectively. The most important parameters are discussed below, the other parameters are discussed in Appendix A.3.

The concave shape of the weld face and the flash on the RS and AS result in a roughness (Sa) of 12-15 μm for all three uncorroded specimens. The roots of these specimens are much smoother and have a roughness of 1-2 μm. The surface roughness stayed relatively the same after immersion. However, the maximum valley depth (Sv) of some surfaces did change after immersion: On the face of the 1.6 mm bare specimen, the maximum valley depth changed from 31 μm before immersion to 41 μm after immersion, and changed from 12 μm to 35 μm on the root. The the root 3.2 mm Alclad specimen was affected as well, in which a change in Sv was observed from 36 μm before immersion to 46 μm after immersion, although no large change in Sv was observed on the face. Finally, no large change in Sv was observed on the face and root of the 1.6 mm Alclad specimen.

Table 8: *Surface roughness parameters of the face and root of the 1.6 mm bare, 1.6 mm Alclad and 3.2 mm Alclad rectangular specimens, before and after 24 hr immersion in 3.5% NaCl. The parameters are the arithmetic mean roughness (Sa), skewness (Ssk), area texture kurtosis (Sku), maximum peak height (Sp) and maximum valley depth (Sv).*

		Uncorroded					**Corroded**				
Surface	**Specimen**	**Sa (μm)**	**Ssk (-)**	**Sku (-)**	**Sp (μm)**	**Sv (μm)**	**Sa (μm)**	**Ssk (-)**	**Sku (-)**	**Sp (μm)**	**Sv (μm)**
Face	1.6 mm bare	15.45	0.18	2.13	54.64	31.47	15.12	0.07	1.92	50.41	40.72
	1.6 mm Alclad	12.11	1.04	4.17	78.47	40.48	12.20	1.07	4.17	79.03	42.21
	3.2 mm Alclad	12.14	0.60	3.12	70.42	34.46	11.75	0.52	2.91	61.97	33.93
Root	1.6 mm bare	1.10	-0.42	7.55	19.46	12.39	1.28	-1.88	22.08	16.78	34.76
	1.6 mm Alclad	2.36	0.69	3.71	22.75	32.62	2.32	0.53	4.24	19.81	33.41
	3.2 mm Alclad	2.03	-0.44	3.94	24.85	35.79	2.38	-0.50	4.23	19.38	45.60

4.4.4 Mass loss results

The 50 mm x 20 mm rectangular specimens were weighed before and after 24 hours immersion in 3.5% NaCl solution. The mass loss of these specimens after immersion is shown in Figure 41. Starting with a mass of 4.3864 gram before immersion, the 1.6 mm bare specimen lost 1.7 mg which is a percentage loss of 0.04%. The 1.6 mm Alclad specimen had a starting mass of 4.3849 gram before immersion and lost 1.2 mg after immersion, which is a percentage loss of 0.03%. The starting mass of the 3.2 mm Alclad specimen was 8.7982 gram, and lost 1.2 mg after immersion, which is a percentage loss of 0.01%. Thus, the bare specimen lost the most mass overall, while the Alclad specimens lost similar amount of mass. However, in terms of percentage the 3.2 mm Alclad specimen lost the least amount of mass.

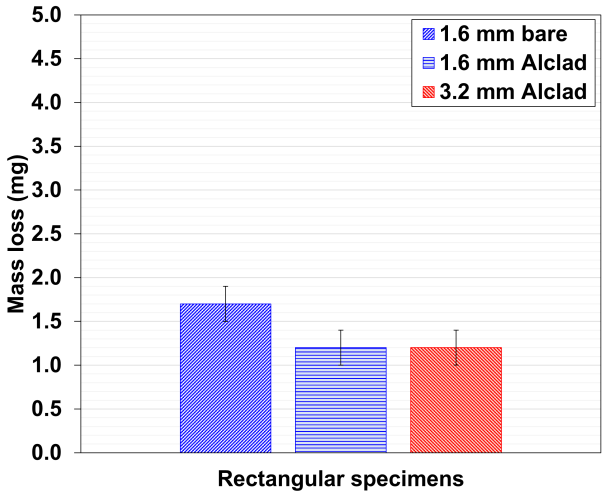

Figure 41: *Mass loss of the 50 mm x 20 mm rectangular specimens after 24 hours of immersion in 3.5% NaCl solution.*

4.5 Electrochemical results

The following sections describe the results obtained from the triple electrochemical tests performed per weld zone on the exposed weld cross-sections of the embedded rectangular specimens. First, the open circuit potentials of the weld zones are presented in section 4.5.1, after which an overview of the linear polarisation resistance (LPR) data is given in section 4.5.2. Finally, the potentiodynamic polarisation data are presented in section 4.5.3. In the following sections, the results of the TMAZ are presented as a combination of HAZ/TMAZ, because a part of the HAZ was exposed in the 1 mm diameter cell as well, due to the cell being wider than the width of the TMAZ. This area was tested only once per side of the weld per specimen for this reason as well.

4.5.1 Open circuit potential

Open circuit potential (OCP) measurements were performed in triples, from which an an average was obtained per weld zone per specimen. In each OCP measurement, the potential was recorded for 1 hour with a 1 mm diameter electrochemical cell containing 100 ml of 3.5% NaCl solution. During these measurements small and large fluctuations in potential were observed in all zones, although some potentials stabilised over time as shown in an example in Figure 42a.

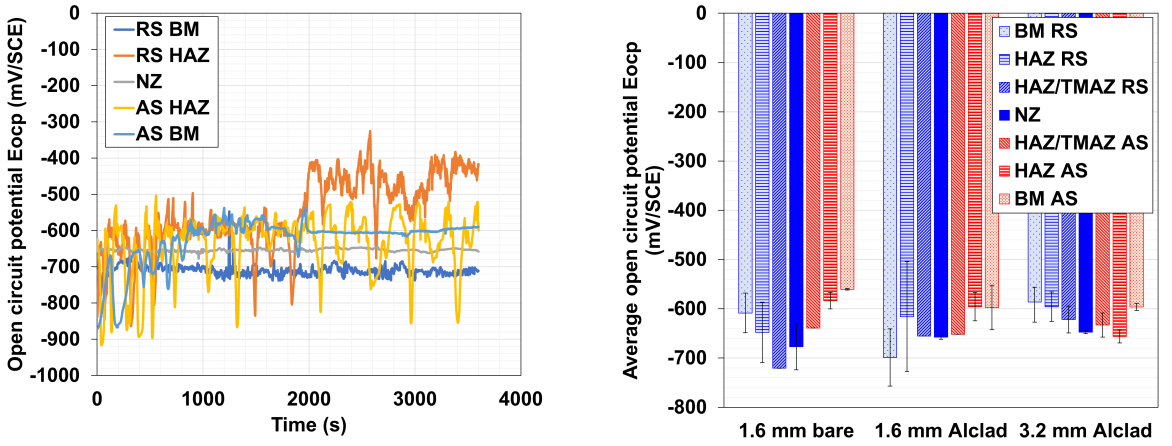

(a) (b)

Figure 42: *(a) OCP measurements versus time in the weld zones of the 1.6 mm Alclad specimen. (b) Average and mean deviation of the open circuit potential (E_{ocp}) per weld zone per specimen.*

The average open circuit potential (E_{ocp}) and standard deviation are presented per weld zone per specimen in Figure 42b. The error bars show the repeatability of the results, although there are no error bars for the HAZ/TMAZ due to the aforementioned singular tests performed on this area. The figure shows large differences in E_{ocp} between the weld zones in each specimen. A difference of 160 mV is observed between the HAZ/TMAZ on the RS and the BM on the AS of the 1.6 mm bare specimen, which are the zones with the most electronegative (-721 mV/SCE) and most noble potential (-561 $\pm$ 2 mV/SCE), respectively. Next, a difference of 101 mV is observed between the BM on the RS (-699 $\pm$ 58 mV/SCE) and the BM on the AS (-598 $\pm$ 45 mV/SCE) of the 1.6 mm Alclad specimen. There is a difference in E_{ocp} of 60 mV between the NZ (-658 $\pm$ 4 mV/SCE) and the BM on the AS (-598 $\pm$ 45 mV/SCE) as well, the latter

potential being the most noble for this specimen. On the 3.2 mm Alclad specimen, a difference of 70 mV is observed between the most electronegative (-656 $\pm$ 13 mV/SCE) and most noble potential (-586 $\pm$ 41 mV/SCE), which are located in the HAZ on the AS and the BM on the RS, respectively. Finally, except for the HAZ/TMAZ on the RS and AS of the 1.6 mm Alclad specimen, no similar weld zones on either side of a nugget zone of all three specimens have similar E_{ocp}.

4.5.2 Polarisation resistance

The average and standard deviation of the polarisation resistance (R_p) are presented per weld zone per specimen in Figure 43. The figure shows less repeatable and overall lower R_p data are observed for the weld zones of the 1.6 mm specimens compared to the 3.2 mm specimen. Only the HAZ on the RS of the 1.6 mm bare specimen has a higher average R_p, but this average is not very repeatable considering the fact that the standard deviation is as large as the average. A possible cause for this large deviation can be found in the spread of the data between measurements performed on this zone, as presented in Appendix A.4. Similarly, non-repeatable data is also observed for the BM on the RS of this specimen, and for the BM and HAZ on the RS of the 1.6 mm bare specimen as well. Furthermore, large differences in R_p are observed between the weld zones of the 1.6 mm specimens. Although, somewhat similar and repeatable R_p of about 10000 to 11000 $\Omega \cdot cm^2$ is observed in the BM on the AS of both 1.6 mm specimens, for which the standard deviation is about 4200 to 4300 $\Omega \cdot cm^2$.

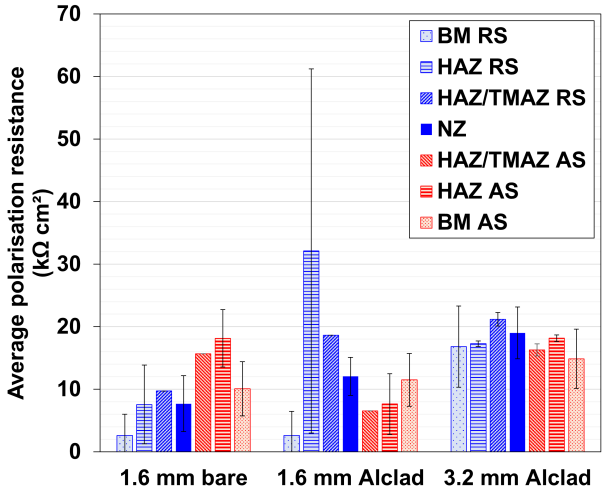

Figure 43: *Corrosion or polarisation resistance (R_p) per weld zone per specimen, as tested in 3.5% NaCl solution in a 1 mm diameter electrochemical cell.*

Compared to the 1.6 mm specimens, more repeatable R_p data is obtained for the weld zones of the 3.2 mm Alclad specimen, in which the R_p ranges from about 15000 to 21000 $\Omega \cdot cm^2$ as measured on the BM on the AS and the HAZ/TMAZ on the RS, respectively. Compared to the BM, slightly higher R_p are observed in the the weld zones of this specimen. However, it must be noted that the spread of R_p values across all zones is similar to the maximum standard deviation observed for this specimen, which is about 6500 $\Omega \cdot cm^2$.

4.5.3 Potentiodynamic polarisation measurements

Figure 44 shows representative polarisation curves per weld zone per specimen, which were obtained from the potentiodynamic polarisation measurements. The corrosion potential (E_{corr}) and corrosion current density (i_{corr}) were extracted from these polarisation curves by taking the X and Y coordinates of the intersection of the cathodic and anodic tafel slopes. The pitting potential (E_{pit}) was taken as the potential at which the current density rapidly increases.

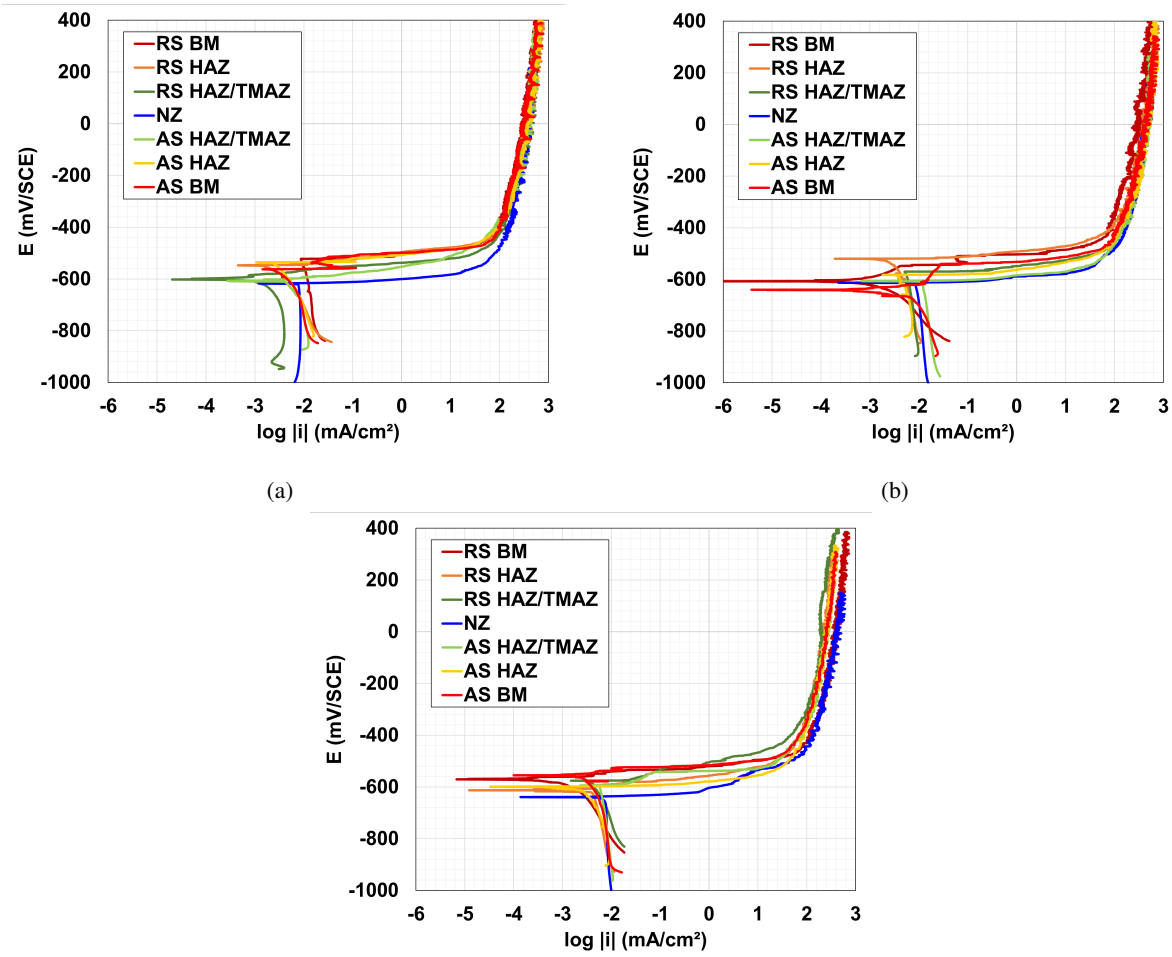

Figure 44: *Polarisation curves of the weld zones in the (a) 1.6 mm bare specimen, (b) 1.6 mm Alclad specimen and (c) 3.2 mm Alclad specimen.*

First, nearly vertical cathodic branches are observed in most of the polarisation curves, whereas the anodic branches are nearly horizontal just above E_{corr}. The latter indicates a rapid increase in current density over a small increase in potential, which can be interpreted as the pitting potential (E_{pit}). At potentials above E_{pit}, the anodic branches change to a nearly vertical slope, which indicates the current density does not increase (much) further at those potentials. E_{corr} and E_{pit} are of similar value for most weld zones. Fluctuations in current density are visible at potentials above E_{pit}. These phenomena are observed for all three specimens.

However, some polarisation curves are different than as described above. For example, small passivation is observed in the BM on the AS of the 1.6 mm bare specimen before the pitting potential is reached. Similarly for the BM of the 1.6 mm Alclad specimen, the potential increases slightly before reaching E_{pit}. Though, most polarisation curves of the weld zones follow the earlier described patterns.

Next, the E_{corr} and E_{pit} values were averaged per test location per specimen and are presented in Figure 45a and Figure 45b, respectively. Overall, an increase in E_{corr} and E_{pit} is observable on both sides of the weld from the BM to the NZ for the 1.6 mm bare specimen, with the NZ having the most active E_{corr} and E_{pit}. Similar observations can be made for the Alclad specimens, with the exception of the very active corrosion and pitting potentials of the BM on the RS of the 1.6 mm Alclad specimen. Large deviations in the average E_{corr} and E_{pit} are observed in the BM and HAZ on the RS of the 1.6 mm Alclad specimen, indicating less repeatability compared to tests performed at other weld zones.

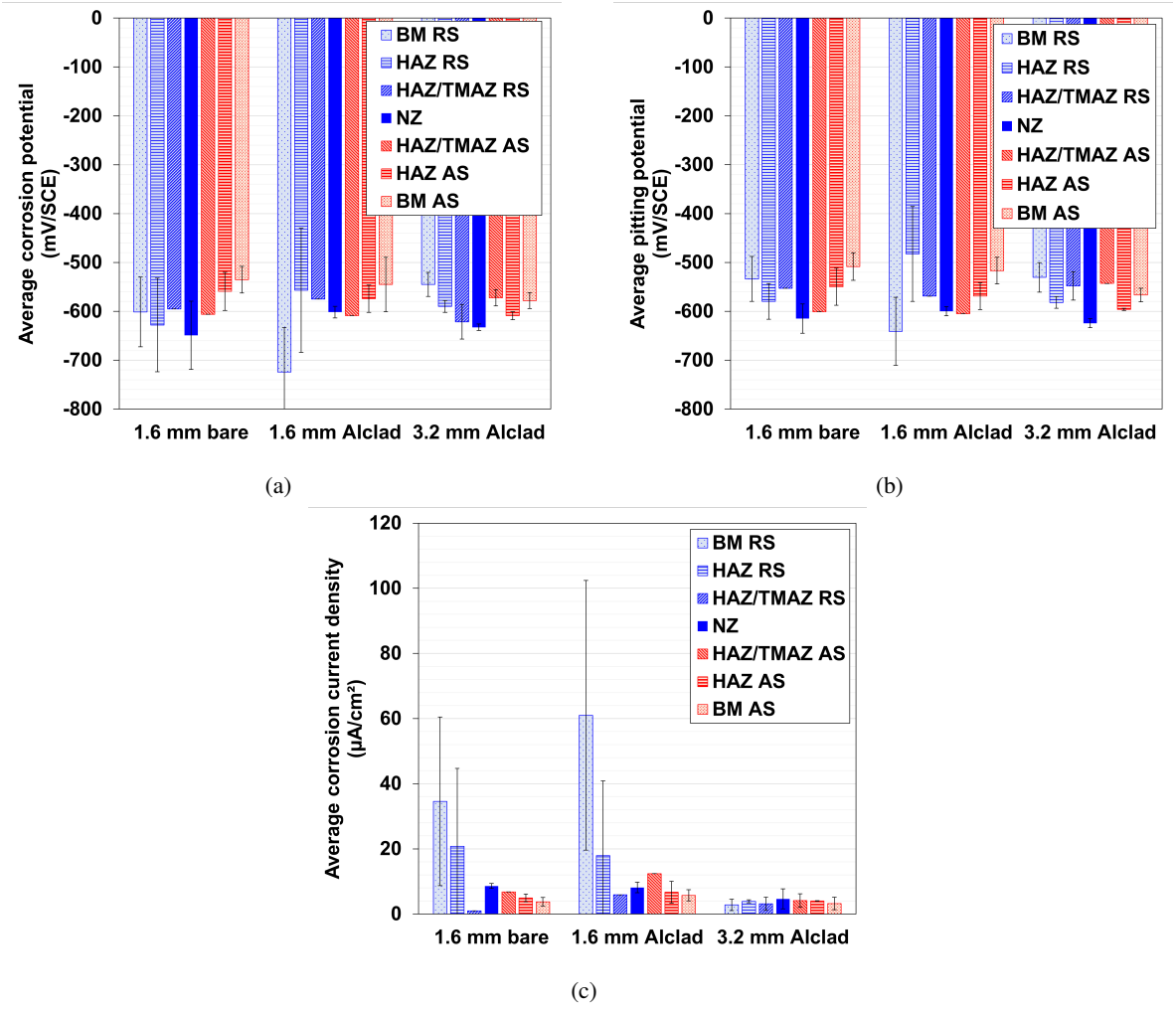

Figure 45: *Graphs showing averaged values per weld zone per specimen for (a) corrosion potential, (b) pitting potential and (c) corrosion current density.*

Finally, the i_{corr} values were averaged per test location per specimen as well, which are presented in Figure 45c. Starting with the 3.2 mm Alclad specimen, the average i_{corr} ranges from 2.8 ± 1.8 μA/cm^2 in the BM to 4.6 ± 3.1

μA/cm^2 in the NZ. In between these zones, the average i_{corr} increases from the BM to the NZ. Similar observations can be made for the advancing side of the 1.6 mm bare specimen, where the i_{corr} increases from 3.8 $\pm$ 1.3 μA/cm^2 in the BM to 8.6 $\pm$ 0.8 μA/cm^2 in the NZ. However, on the retreating side of this specimen very high i_{corr} of about 21 to 35 μA/cm^2 and large standard deviation of similar value are observed in the BM and the HAZ. This would indicate that the data is not repeatable for these two zones, possibly due to an outlier. Similarly, very high i_{corr} are observed in the BM (61 $\pm$ 41 μA/cm^2) and the HAZ (18 $\pm$ 23 μA/cm^2) on the RS of the 1.6 mm Alclad specimen, which are not repeatable due to the high standard deviation as well. Fortunately, repeatable data is obtained for the other zones of the 1.6 mm Alclad specimen, in which the average i_{corr} ranges from 5.7 $\pm$ 1.7 μA/cm^2 in the BM (on the AS) to 12 μA/cm^2 in the HAZ/TMAZ on the AS.

5 Discussion

5.1 Characterisation of the weld microstructure and relationship with mechanical properties

5.1.1 Weld macrostructure and surface appearance

The NZ of each weld follows the shape of the respective tool pin, and are of similar width as the pin diameter. The small recrystallised equiaxed grains (∼5 μm) in the NZ can be explained by large plastic deformation and high heat cycle caused by travel and rotation of the tool pin, and are similar in shape and size to those in friction stir welds [12], [32]. The TMAZ was characterised by non-recrystallised rotated grains (∼15 μm) just outside the NZ, with an abrupt microstructural transition on the AS and a gradual transition from NZ to TMAZ and HAZ on the RS. The rotation of the grains is caused by plastic deformation due to the rotating pin and is helped by a small heat cycle [8], [87]. Furthermore, the difference in transition between NZ and TMAZ between the AS and RS can be explained by partial recrystallisation occurring in the TMAZ on the RS due to a locally larger heat input and more plastic deformation with respect to the AS, which is caused by a difference in material flow [87], [113]. These microstructural differences between RS and AS are typical for both conventional and stationary shoulder friction stir welds [12], [79], [87], [113].

Next, the welds' HAZ contain similar sized grains as the BM (40-50 μm), since there is no plastic deformation and lower heat input due to the lack of rotating shoulder. The similar size of the grains made it impossible to determine the width of the HAZ by optical microscopy alone, therefore the microhardness profiles were used to determine the width. Typically, microstructural observations with SEM and/or TEM are used to identify the amount and size of hardening precipitates in the HAZ [32], which can help distinguish the HAZ from the BM as well. These microstructural observations with SEM and/or TEM are therefore recommended for a future study, in which the microhardness (and corrosion properties) can be linked to the distribution of hardening precipitates. Lastly, macrostructural differences between the 1.6 mm and 3.2 mm weld specimens, such as the different shapes of the onion rings, and the more gradual transition between the NZ and the TMAZ on the RS of the 3.2 mm weld specimen compared to the 1.6 mm weld specimens, may be explained by differences in material flow caused by the different tool pin designs used to weld these sheets. Mixing of cladding into the NZ of the Alclad specimens may be attributed to the tool pin design as well. To fully understand the impact of tool pin design on material flow, heat cycle, recrystallisation, recovery and precipitation it is recommended to perform a subsequent study into this effect by varying the tool pin design and recording the subsequent parameters.

Next, some small weld thinning of 0.02 to 0.04 mm was observed in the welds, which may be attributed to the plunge depth of the pin and to removal of material by the shoulder [8], [95]. The size of flash (∼60 μm) on the face of the welds can also be attributed to the removal of material by the shoulder [8], [113]. Using photos of surface appearances, Li, Yue, Ji, *et al.* [113] have shown that the size of flash is lower in stationary shoulder friction stir welds than in conventional friction stir welds, although no quantitative comparison was reported. Furthermore, the surface roughness parameters (Table 8) indicate relatively smooth surfaces were achieved compared to conventionally FSW'd joints [14], [113], [114]. This may be explained by the smoothening effect of the stationary shoulder, according to Wu, Chen, Strong, *et al.* [14] and Li, Yue, Ji, *et al.* [113]. Furthermore, the larger surface roughness (Sa) of the face of the welds with respect to their roots can be explained by the fact that the tool interacts with the material on the face more so than the root. Unfortunately, the surface roughness of the face (∼ 15 μm) is larger than is acceptable in aerospace

engineering (3.2 μm), therefore a post-welding surface finish is recommended. Finally, the maximum peak height (Sp) and maximum valley depth (Sv) can be explained by the displacement of material described earlier, resulting in the earlier mentioned flash and minor weld thinning.

Unfortunately, some weld defects in the form of voids exist on the roots of the uncorroded 1.6 mm and 3.2 mm Alclad specimens (Figure 36 and Figure 37) but not on the bare specimen, which may indicate material flow problems of the clad layer during welding. Material flow problems in the root can caused by incorrect plunge depth, or insufficient heating due to too high tool travel speed at too low tool rotation speed [8], [73]. To make sure the stationary shoulder friction stir welds are sound and without defects, a study should be performed on the heat generation during welding, which can be done using thermocouples in combination with a variation of welding speeds. Care should be taken that sufficient heat is generated in the weld root. In case the temperature is sufficiently high and these void defects still occur, a study can be performed in which the plunge depth or pin length is varied, to see whether this effect still occurs at larger plunge or penetration depths.

5.1.2 Microstructure, microhardness and tensile properties

In section 4.2 and Figures 29-31 the distribution of the microhardness across the welds was shown. Generally, a drop in microhardness was observed from the BM to the HAZ, with a maximum microhardness in the HAZ near the TMAZ, before falling to a minimum in the TMAZ and a small increase again in the NZ. Typically, these observations are explained using SEM or TEM images combined with differential scanning calorimetry (DSC), which show the distribution and size of hardening precipitates per weld zone [12], [32], [94]. Unfortunately, none of these techniques were applied in this thesis, and therefore no details on the precipitation of the SSFSW'd AA2024-T3 butt joints can be given. However, the microhardness profiles show similar patterns as those observed by Bousquet, Poulon-Quintin, Puiggali, *et al.* [32], who showed that the microhardness in FSW'd AA2024-T351 was mainly controlled by the distribution of GPB-zones and intergranular S-phase precipitates (Figure 7). Due to the welding and concurrent heat cycle, some of these GPB-zones dissolved into solid solution and S-phase precipitates coarsened, altering the local microhardness. However, these phenomena need to be investigated for stationary shoulder friction stir welds in a future study, to be able to fully support the observations made in this thesis. Lastly, the Hall-Petch relationship states that strength increases when grain size decreases, which would explain the rise in microhardness in the NZ [12], [32].

Next, the ultimate tensile strength (UTS) of the uncorroded BM specimen was in line with the UTS specified by the supplier for the 1.6 mm bare sheets. However, the measured UTS of the uncorroded BM specimens of the 1.6 mm Alclad and 3.2 mm Alclad specimens were respectively 21 MPa and 15 MPa lower than the UTS reported by the suppliers. This difference is likely caused by an inaccurate reading of the specimens' thickness, as the dimensional accuracy can affect the test results greatly [123]. Since the UTS is determined by the maximum amount of applied force divided by the cross-sectional area perpendicular to the force direction, a different reading in one or two of the cross-sectional area's dimensions results in a different UTS. To support this theory, by using the material thickness as reported by the suppliers (1.6 mm) together with the maximum force measured during tensile testing ($\sim$4.3 kN) in the calculation for the UTS, the same UTS is achieved for the tested BM of the 1.6 mm Alclad specimens as the UTS reported by the suppliers ($\sim$438 MPa). Furthermore, the observed UTS of the BM of the 1.6 mm Alclad specimens is lower than that of the welded specimens, which is rather uncommon [84], [91], [92]. Typically, welds are less strong than unwelded material due to the change in microstructure (over-ageing and coarsening of hardening precipitates) and

resulting drop in microhardness [12], [32]. Thus, it is highly likely that the UTS of the 1.6 mm Alclad uncorroded BM specimens as presented in section 4.3 is incorrect. Therefore, the UTS specified by the supplier is used as the UTS of the 1.6 mm Alclad uncorroded BM specimens for the remainder of this discussion.

The 1.6 mm bare specimens have the highest UTS and elongation before and after welding, compared to the Alclad specimens, which can be explained by the lower tensile properties of the applied AA1050 layer on the Alclad specimens. The drop in UTS after welding can be attributed to the drop in local microhardness of the TMAZ and due to the weld thinning, since the TMAZ has low microhardness and this location has reduced load baring area. The HAZ also has low microhardness, but since this is outside the thinned area, the load bearing area is larger than inside the weld itself. The reduction in elongation (or embrittlement) of the weld can be attributed to the change in macrostructure: The small equiaxed grains in the NZ enable more brittle fracture, due to the ease of which a crack can propagate along these small grains (intergranular fracture). Furthermore, the sharp transition of the macrostructure between the NZ and the TMAZ on the AS may also play a role in this embrittlement; large interfaces between weld zones enable quick intergranular fracture without microvoid coalescence [125]. Moreover, cracks could grow more easily along the clad flow arm that is mixed into the NZ of the Alclad specimens for the same reason as well, which lowers ductility. Lastly, the weld defects (voids) on the roots of the Alclad specimens may play a role in the loss of ductility as well, as cracks can initiate and grow quicker in these voids. The flow problems of the cladding during welding as described in section 5.1.1 may therefore also be a possible cause for the loss in ductility. However, all welds still show ductile fracture behaviour as is evident by small necking near the fracture and dimpled surface, shown in Figure 33.

Similar loss of ductility was found in friction stir welds as studied by Radisavljevic, Zivkovic, Radovic, *et al.* [84], Li, Xu, Li, *et al.* [91], and Zhang, Xiao, and Ma [92], which shows that loss of ductility is still an issue in welding. However, embrittlement of the weld should be studied more thoroughly using electron backscatter diffraction (EBSD) to create texture maps of the macrostructure, which help locate aligned slip planes. Furthermore, digital image correlation (DIC) should be used during tensile tests to locate low strain zones, after which fractography using SEM can be used to identify the fracture surfaces. From these fracture surfaces the corresponding fracture mechanisms such as microvoid coalescence or cleavage can be determined, which allow for interpretation of the local ductility.

5.2 Characterisation of corrosion behaviour and relationship with microstructure

5.2.1 Susceptibility to pitting corrosion

In section 4.4.2 the pit morphology and pit statistics were presented. In that section, it was shown that the face of the 1.6 mm bare specimen contained the largest and deepest pits (located on the RS flash), compared to the other specimens and surfaces. The root of the 1.6 mm bare specimen also contained a high density of pits, but these were in smaller size and depth. This would indicate that the RS flash on the face is a more active corrosion site, and more susceptible to pitting corrosion than the root of the bare specimen. This can be caused by local corrosion kinetics favouring this location, which is discussed in section 5.2.3. Differences in roughness may play a role here as well, since the face of the 1.6 mm bare specimen has a higher surface roughness than the root (Table 8). However, this is not a definite explanation for this observation, as there may be different corrosion kinetics at play between the face and root of the weld. This difference in severity of pitting between face and root may be studied in a follow up project, by exposing the face and root surfaces to a salt solution separately.

The Alclad specimens show less severe pitting than the bare specimen, although a few small pits were still present. This can also be attributed to local corrosion kinetics, in which the Clad layer has a more electronegative corrosion potential, but lower corrosion current density (than the bare specimens). Also, the lack of pits on the face of the Alclad specimens (from which the cladding was removed) indicates the protective capabilities of the cladding, which is similar to observations made by Petroyiannis, Pantelakis, and Haidemenopoulos [111].

The tensile properties may also confirm the susceptibility of the bare specimens to pitting corrosion. The elongation (presented as max strain % in Figure 32b) was noticeably reduced after immersion in 3.5% NaCl for the bare specimens, but not for the Alclad specimens. This may be due to the formation of deep and large pits on the face of the bare specimen, whereas the Alclad specimens did not form such large and deep pits. The formation of large and deep pits can introduce crack initiation sites, which would lower the elongation. This was observed by Petroyiannis, Pantelakis, and Haidemenopoulos [111], who have linked corroded surfaces of unwelded AA2024 to loss in local ductility. However, fractography was not conducted in this thesis, thus this may not be concluded from the results presented in this thesis alone. Fractography using SEM is therefore recommended for a follow up project.

However, the UTS was unaffected by pitting corrosion, which was against expectation. An explanation for this may be that the corrosion pits were not significantly deeper than the amount of weld thinning. The molarity of the test solution and the exposure time of the specimens in the solution, which affect corrosion rate [126], may not have been sufficient enough to produce corrosion pits deep enough to affect the UTS. Uncertainty in the determination of thickness of the tensile test specimens and tolerances of sheet thickness ($\pm$ 5%) may play a role as well. Similar observations were made by Pantelakis, Chamos, and Kermanidis [99], who have shown that the UTS of (unwelded) bare and Alclad AA2024 specimens is not affected by pitting corrosion for exposure times of up to at least 100 hours in 3.5% NaCL solution, which they attributed to small uniform corrosion (20 μm) instead of pitting corrosion.

Nonetheless, based on the depth and size of pits in the immersion specimens, and the loss of elongation of the 1.6 mm bare tensile specimens, it is clear that the bare specimens are the most susceptible to pitting corrosion. Furthermore, the existence of small pits on the Alclad specimens shows that these specimens are somewhat susceptible to pitting corrosion, although the severity of corrosion is much less than bare specimens. The discussion of the corrosion kinetics in the following section can shed a light on the mechanisms behind these observations.

5.2.2 Open circuit, corrosion, and pitting potential

The open circuit potential (E_{ocp}) and corrosion potential (E_{corr}) are different at some test locations, whereas they should be the same as they both describe the equilibrium potential of oxidation and reduction reactions happening simultaneously without a net flow of current [120]. This difference may be caused due to a still changing potential at the end of the OCP measurement, which would result in a different equilibrium potential when measured at a later time. Mansfeld [120] states that OCP increases over time due to passivation of passive specimens, but can decrease at the onset of localised corrosion. On the other hand, the difference between Eocp and Ecorr may also be caused by the potentiodynamic polarisation measurement, either by inaccuracies in the application of the tafel extrapolation method, or by the fact that the polarisation measurement was performed at a later time, which would result in the increased corrosion potential mentioned earlier. For future studies, longer test times are suggested for the OCP measurements, such that the potential has fully stabilised before commencing other electrochemical studies on that test location.

However, it must be noted that both potentials follow similar trends along the weld cross-sections: potentials become more negative from the BM to the NZ (and back again to the BM on the other side of the weld), with a large difference in potential between the most noble and most active corrosion sites (of up to 160 mV). This trend may indicate that the weld zones are more susceptible to corrosion than the BM, which is discussed in the next sections. In the following sections, Eocp is considered as the corrosion potential, since the OCP measurements and the immersion tests were both performed under open circuit conditions, meaning no external potential or current was applied. The E_{ocp} values may therefore be a better representation of the equilibrium reactions occurring at the surface of the immersion specimens than the corrosion potentials obtained from the polarisation curves, although the polarisation curves give more insights in the corrosion kinetics [120]. The corrosion kinetics are discussed in a later section.

Finally, similar trends are observed for the pitting potential (Epit) as well, where the most active potentials are observed in or near the NZ and become more noble towards the BM. Furthermore, pitting potentials equal to or near the corrosion potential show the immediate breakdown of the surface layer at those locations, which is the case for the weld zones. On the contrary, a large difference shows some passive behaviour, which is the case for the BM of the specimens.

5.2.3 Relationship between corrosion potential, locations of corrosion pits and microstructure

First, the locations of corrosion pits on the face of the 1.6 mm bare specimen correspond with the zone in which the most electronegative (or active) corrosion potential observed, namely that of the HAZ/TMAZ border on the retreating side (RS). On the contrary, the distribution of pits on the root of this specimen is located mainly on the advancing side (AS), however these pits are located on the HAZ/TMAZ border as well. Similar location of corrosion were observed in friction stir welds, in which pitting and IGC was observed in the HAZ at the HAZ/TMAZ border [31]. Threadgill, Leonard, Shercliff, *et al.* [8] discuss several papers in which it is shown that corrosion location is dependent on welding parameters and local microstructure, which they mainly attribute to vulnerable copper depleted zones due to the precipitation of a copper rich network along grain boundaries. Bousquet, Poulon-Quintin, Puiggali, *et al.* [32] related the corrosion sites to the distribution of hardening precipitates and size of grain structure; continuous lines of S-phase precipitates along grain boundaries in the HAZ enhance IGC. As mentioned in earlier discussions, no characterisation techniques that could identify such precipitates were performed in this thesis, and are therefore recommended for further research in order to link the corrosion observations with the distribution of precipitates.

Next, the corrosion potential of the BM on the RS of the 1.6 mm Alclad specimen is inconsistent with literature and seems to be more in the range of expected potentials for AA1050 (Table 4). It is possible that during testing the electrochemical cell was placed too close to the clad layer, which was not fully removed from the face prior to testing (only near the weld area) to test the specimens as delivered. In ASTM G69 it is suggested to remove the cladding before testing for open circuit or corrosion potentials, since cladding can have an influence on the results [110]. However, the corrosion potential of the BM on the AS of this specimen is consistent with literature (Table 4), and the trend or distribution of corrosion potentials is otherwise consistent with that of the 1.6 mm bare specimen. Here, the most active corrosion potential is observed on the NZ and on the HAZ/TMAZ near the NZ. However, no large and deep pits were observed on the face or the root of the 1.6 mm Alclad specimen, only a few smaller and shallower pits were observed (Figure 40). Furthermore, even though there was no cladding near the weld face, there were only a few small pits observed on the face of this specimen. This can be explained by the protective properties of the cladding as described by Petroyiannis, Pantelakis, and Haidemenopoulos [111], who described a sufficient corrosion protection when at least

30% of the substrate surface was covered with cladding. Further implications of this observation are discussed in section 5.3.2. The shallow depth of the pits that did form may be explained by the low corrosion current density of the clad layer, which is about 0.89 μA/cm^2 for AA1050 (Table 4). Finally, the deepest and largest corrosion pits on the root of the 1.6 mm Alclad specimen seemed to have formed on pre-existing voids, the possible cause of which have been discussed in section 5.1.1. These pre-existing voids are likely to have been formed by the welding process and are considered as defects. Since there is a fault in the microstructure, this site may be more active than others due to a possible lack of oxygen in the void, which may lead to crevice corrosion [34], [96], [127]. However, this was not tested explicitly in this thesis and does not need to be tested in future projects, as the voids should not exist in the first place.

Finally, the 3.2 mm Alclad specimen showed the least amount of pitting in the white light interferometry (WLI) scans, with no observable pits on the face (Figure 34f) and only a few shallow pits on the root (Figure 37). This may be explained by the relatively high polarisation resistance measured for this specimen, compared to the 1.6 mm specimens (Figure 43). The measured corrosion current density is low for this specimen as well, which would explain the shallowness and small size of the pits. Similar to the 1.6 mm Alclad specimen, the cladding seems to provide corrosion protection for the face, from which the cladding was removed prior to welding.

5.2.4 Relationship between local corrosion kinetics, observed corrosion damage and microstructure

Although there were no significantly deep pits observed on the face and root of the 3.2 mm Alclad specimen due to the protective capabilities of the clad layer, the potendiodynamic polarisation data shows an interesting increase in i_{corr} from the BM to the NZ, similar to the decrease in potential between these zones. This would indicate that a faster corrosion rate is possible at the NZ compared to the BM, should there no protective clad layer.

A similar trend is observed on the AS of the 1.6 mm thick specimens as well, for which the i_{corr} also increases from the BM to the NZ, which provides more certainty to the above relationship. However, in the BM and HAZ on the RS of these specimens the i_{corr} are much higher than is reported in literature (Table 4), and are inconsistent with respect to the zones on the RS. A high standard deviation is observed here as well, which indicates these results are not repeatable for these locations. These high i_{corr} may be explained by either local galvanic corrosion between the clad layer and the substrate for the Alclad specimen, or by possible strain deformation or residual stresses (from cutting the specimen, for example) [32]. The i_{corr} of these zones is therefore considered incorrect and ignored in further discussion.

Fortunately, the i_{corr} values of repeatable measurements of all three specimens are in line with literature (Table 4), as the i_{corr} ranges from 2.8 μA/cm^2 in the BM, which may be linked to the presence of Al_2Cu (θ-phase) particles, to about 12 μA/cm^2 in the HAZ/TMAZ, which may be linked to the presence of Al_2CuMg (S-phase) particles. Interestingly, the location of high microhardness (Figure 29) coincides with this location of high i_{corr}, which may suggest that more (peak-aged) S-phase hardening precipitates are indeed present in the HAZ/TMAZ. As mentioned earlier, the corrosion pits observed on the face of the 1.6 mm bare specimen are located in this zone as well, the depth of these pits may therefore be directly related to the corrosion current density to the presence of S-phase precipitates. A follow up study in which microstructural characterisation techniques are applied at the nano scale may provide insights in the distribution and size of these precipitates in these welds.

5.3 Effectiveness and feasibility of Alclad as corrosion protection method

5.3.1 Influence of cladding on mechanical properties

The clad layer influences the overall mechanical properties of all Alclad specimens negatively, due to the lower mechanical properties of AA1050 (Table 2). This means that the load bearing area (or stress bearing area) is lowered by the thickness percentage of the clad layer. This was observed for all tested tensile specimens, where the 1.6 mm bare specimens had the highest UTS and elongation in the BM only, uncorroded weld and corroded weld specimens, compared to the Alclad specimens. However, the UTS of the welded Alclad specimens did not seem to be affected much by the mixing of cladding into the weld (Figure 28), as all welded specimens showed similar weld efficiencies for the UTS (around 96%). This may indicate that optimal weld parameters were used with respect to the UTS, as Ji, Li, Zhou, *et al.* [93], Xu, Li, Lv, *et al.* [94], and Li, Yue, Ji, *et al.* [113] showed that stationary shoulder friction stir welded Alclad AA2024 can achieve higher failure loads with improved weld parameters.

However, a larger loss in ductility was observed in the Alclad specimens after welding compared to the bare specimens (section 4.3), which may be attributed to the mixing of cladding into the weld (Figure 28) and the presence of voids in the root. Moreover, the flow arm of the cladding into the nugget zone was longer for the 3.2 mm Alclad specimen compared to the 1.6 mm Alclad specimen, while coincidentally a greater loss in elongation after welding was observed for the former specimen. This may indicate a correlation between the amount of mixing of cladding into the weld and the reduction in elongation. The possibility of a correlation between these phenomena could be subject of a follow up project, but as the mixing of cladding into the weld should be avoided (according to Zhang, Xiao, Wang, *et al.* [37]) this may not be such an interesting subject.

5.3.2 Influence of cladding on corrosion behaviour

As discussed in section 5.2.3, the Alclad specimens showed less corrosion damage (smaller and shallower pits, lower pit density) after 24 hour immersion in 3.5% NaCl solution than the bare specimen, which was attributed to a more active corrosion potential and a lower corrosion current density of the clad layer[6] with respect to the substrate. It is commonly known that sites with more active corrosion potential are preferentially attacked over sites with more noble corrosion potential [34], [96]. The small pits that did form on the root can be explained by the low corrosion current density of AA1050 (Table 4), which indicates a low corrosion current rate (and inversely high corrosion resistance). Furthermore, the top surfaces of the Alclad specimens, from which the clad layer was removed prior to welding, showed no or little corrosion damage, indicating that the cladding provides protection outside of the cladded zone. This effect was demonstrated (for unwelded AA2024) in a study by Petroyiannis, Pantelakis, and Haidemenopoulos [111] as well, in which only 30% coverage was needed to provide sufficient corrosion protection. This results in the high effectiveness of protection, even for welded specimens.

5.3.3 Feasibility of Alclad for corrosion protection method

It is clear that cladding lowers the tensile properties, but provides effective corrosion protection by lowering the susceptibility to pitting corrosion. However, other studies have shown that fatigue strength/life (not tested here) may be reduced by 50% for unwelded AA2024-T3 due to cladding [99]. Together with the lowered tensile properties and

[6] The clad layer was not tested on its own, and thus this observation is based on data from literature.

possible mixing of cladding into the weld, the application of cladding may not be an optimal solution if these welds are to be used in aerospace applications. It is therefore recommended to investigate possible alternatives for corrosion protection methods of stationary shoulder friction stir welded AA2024-T3. A possible suggestion may be to investigate the application of anodisation techniques on bare AA2024-T3 after welding, with or without conversion coatings.

5.4 Comparison and ranking of weld performance

The welds are compared and ranked based on their performance with with respect to the mechanical and corrosion properties, after which a ranking based on overall performance is presented.

5.4.1 Ranking based on mechanical properties

Based on the microhardness values and tensile properties presented in section 4.2 and section 4.3, the 1.6 mm bare specimen performs best, followed by the 1.6 mm Alclad specimen and the 3.2 mm Alclad specimen. As mentioned in section 4.3, the 1.6 mm bare specimen has the highest UTS and elongation between all specimens (BM only, uncorroded weld and corroded weld). The Alclad specimens have similar UTS before and after welding, but the 1.6 mm specimen has better weld efficiency (with respect to the elongation) than the 3.2 mm specimen, placing the 1.6 mm Alclad specimen on the second place, followed by the 3.2 mm Alclad specimen.

5.4.2 Ranking based on corrosion behaviour

The ranking with respect to corrosion behaviour is based on the overall corrosion performance of each weld (so, not per weld zone), and is based on the polarisation or corrosion resistance (R_p), corrosion current density (i_{corr}), average pit depth and density, average pit size and impact on elongation. A higher R_p means a better resistance against corrosion [96], [120], thus overall higher R_p in Figure 43 is better. A lower i_{corr} means a slower corrosion reaction [96], [120], thus overall lower i_{corr} in Figure 45c is better. A lower average pit depth and density and a smaller pit size indicates less corrosion has occurred in the time of exposure, thus overall lower numbers in Figure 40 indicate a better corrosion performance. A smaller change in elongation in Figure 32b between uncorroded and corroded weld specimens indicates better corrosion performance. For almost all parameters, the 3.2 mm Alclad specimen performs best, the 1.6 mm Alclad specimen performs second best and the 1.6 mm bare specimen performs worst. This means that the 1.6 mm bare specimen is affected by corrosion the most, whereas the 3.2 mm Alclad specimen is affected the least.

5.4.3 Ranking based on overall performance

Since mechanical properties are most important for the selection of alloys/materials in aerospace design [37], [95], the importance of these properties are weighed over the corrosion properties since the latter can be enhanced with proper protection methods. As such, the 1.6 mm bare specimen performs best, followed by the 3.2 mm Alclad specimen and finally succeeded the 1.6 mm Alclad specimen.

Although the 1.6 mm bare specimen performs best overall because of the better mechanical properties and lack of cladding mixed into the weld, the bare specimens are highly susceptible to pitting corrosion in chloride containing environments. To avoid weld defects and improve corrosion resistance it is recommended to perform subsequent

research on finding or developing a suitable post-welding corrosion protection method, such as post-weld application of Alclad or post-weld anodisation.

5.5 Comparison with FSW'd AA2024 from literature

5.5.1 Macrostructure, microstructure and surface roughness

First, smaller TMAZ and HAZ are achieved in the SSFSW'd 1.6 mm bare, 1.6 mm Alclad and 3.2 mm Alclad sheets compared to the TMAZ and HAZ of the 12 mm thick FSW'd AA2024-T3 sheets as presented in Figure 7a (by Bousquet, Poulon-Quintin, Puiggali, *et al.* [32]). Similar decrease in width of the weld zones between FSW'd and SSFSW'd joints was observed by Wu, Chen, Strong, *et al.* [14] and Xu, Li, Lv, *et al.* [94]. An explanation for this result was presented by Wu, Chen, Strong, *et al.* [14], who have demonstrated that a smaller and more uniform through thickness thermal field is produced when a stationary shoulder is used compared to a rotating shoulder, which results in smaller weld zones.

Second, smaller grain sizes are observed in the BM and HAZ of the SSFSW'd 1.6 mm bare, 1.6 mm Alclad and 3.2 mm Alclad sheets compared to the 12 mm thick FSW'd AA2024-T3 sheets [32], although similar grain sizes are observed in the NZ. The difference in grain size in the BM and HAZ may be explained by the difference in sheet thickness, since the rolling process has a larger influence on the surface material than the bulk material [36]. The similar grain size of the NZ may be explained by the fact that similar temperature and deformation strain are reached to recrystallise the grains in this weld zone [14].

Finally, the surface roughness of the SSFSW'd 1.6 mm bare, 1.6 mm Alclad and 3.2 mm Alclad sheets is lower compared to the surface roughness of FSW'd (and SSFSW'd) 0.8 mm Alclad lap-joints as reported by Dong, Yang, Ren, *et al.* [114], meaning a smoother weld surface is achieved in the former welds. As discussed earlier in section 5.1.1, the smoother surface of the SSFSW'd joints can be explained by the smoothening effect of the stationary shoulder and smaller shoulder plunge depth, whereas more material is displaced by the rotating shoulder in conventional FSW [14], [113].

5.5.2 Microhardness and tensile properties

Similar microhardness are reported for the BM of FSW'd and SSFSW'd joints [12], [32], even though the sheets are of different thickness. However, overall slightly higher microhardness was achieved across the weld zones of the SSFSW'd 1.6 mm bare, 1.6 mm Alclad and 3.2 mm Alclad sheets compared to literature [12], [32]. A possible explanation for this observation can be a difference in precipitate distribution, which in turn can be explained by the smaller and more uniform through thickness thermal field produced in SSFSW compared to FSW, as proposed by Wu, Chen, Strong, *et al.* [14]. The lower heat generated in the TMAZ and HAZ results in less over-ageing of the hardening precipitates, which result in more peak-aged precipitates which increase the microhardness [92]. However, the size and distribution of hardening precipitates was not observed in this thesis, and should therefore be measured using the appropriate techniques in a follow up study.

Better tensile properties in terms of weld efficiency are observed for the SSFSW'd 1.6 mm bare, 1.6 mm Alclad and 3.2 mm Alclad sheets compared to FSW'd sheets as reported by Radisavljevic, Zivkovic, Radovic, *et al.* [84], Li, Xu, Li, *et*

al. [91], and Zhang, Xiao, and Ma [92]. Higher weld efficiency was achieved for both the ultimate tensile strength and maximum elongation. The better weld efficiency of the SSFSW'd sheets may be attributed to several factors, including but not limited to higher microhardness of the weld zones (due to less over-ageing of hardening precipitates), a more gradual transition of the macrostructure between weld zones, and smaller weld thinning.

5.5.3 Corrosion properties

Overall less corrosion damage (in terms of pit depth) was observed in the SSFSW'd 1.6 mm bare, 1.6 mm Alclad and 3.2 mm Alclad joints compared to FSW'd joints [30]–[32]. However, lower corrosion and breakdown potentials are observed for the SSFSW'd 1.6 mm bare, 1.6 mm Alclad and 3.2 mm Alclad joints and the FSW'd joints [30], [32]. A possible reason for these differences may be attributed to the higher NaCl concentration used in the aforementioned studies, more so than to a difference in macrostructure, since higher NaCl concentration increases the corrosion rate [126]. It may be possible that the smaller weld zones of the SSFSW'd joints are of influence as well, since less material with corrosion enhancing microstructure is available. However, no correlation or causation between the size of the weld zones (TMAZ and HAZ) and the corrosion properties can be established, since no direct comparison of the corrosion properties between SSFSW'd and FSW'd joints of the same thickness and test solution was made in this thesis. Therefore, a direct comparative study between FSW'd and SSFSW'd joints of similar sheet thickness and test solution may be needed to provide these insights.

6 Conclusions

Based on the analysis of the results and subsequent discussion, the following could be concluded regarding the research questions:

1) What are the dimensions of macrostructural features and surface appearance of the SSFSW'd joints, in terms of weld zone size, grain size, surface roughness, weld thinning, and flash?

The welds' macrostructure are characterised by a nugget zone (NZ) in the centre of the weld, with a width similar to the tool pin diameter, which contain fully recrystallised equiaxed grains of about 5 μm. The NZ is neighboured by small (max 1.2 mm wide) thermo-mechanically affected zones (TMAZ) with a gradual microstructural transition on the retreating side (RS) and a sharp transition on advancing side (AS). The TMAZ contains rotated grains in ST-direction ($\sim$15 μm) which are not (fully) recrystallised. The TMAZ is followed by the heat affected zone (HAZ), which are about 6 mm wide according to the microhardness profiles and contain similar sized grains as the base material (BM) (40-50 μm). Small weld thinning of 0.02-0.04 mm and flash on the weld face in the order of 60 μm was observed in all welds. Surface roughness of $\sim$15 μm was achieved on the weld faces and $\sim$2 μm on the roots. Cladding was partially mixed into the NZ of the Alclad welds. Voids on the root of the Alclad specimens may indicate material flow problems or insufficient heating at the root.

2) Is there a relationship between the macrostructural features, microhardness, tensile properties and fracture locations of the welds?

Weld efficiencies of 96% with respect to the ultimate tensile strength (UTS) and 40-60% with respect to the elongation were achieved for the SSFSW'd joints, which was attributed to a drop in microhardness in the TMAZ to $\sim$126 $Hv_{0.2}$ and the sharp microstructural transition between the NZ and the TMAZ on the AS. The lower elongation of the Alclad welds compared to the bare weld was attributed to partially mixed clad layer into the NZ, and to voids on the root of the Alclad welds. All welded specimens fractured along the weld root on the AS.

3) Which weld zones are the most susceptible to pitting corrosion in terms of pit dimensions and effect on tensile properties, and is there a relationship with the macrostructure and local electrochemical properties?

The 1.6 mm bare weld is very susceptible to pitting corrosion as was evident by the formation of relatively large pits on the RS of the weld face and high density of smaller pits on the root. The 1.6 mm Alclad weld is less susceptible to pitting corrosion as less pitting was observed on both the face and the root. The 3.2 mm Alclad weld is not very susceptible to pitting corrosion as very few and shallow pits were observed, although pits did form on pre-existing voids on the root surface.

Corroded weld specimens showed no loss of strength compared to uncorroded weld specimens after 24 hr immersion in 3.5% NaCl solution, however some loss in elongation was observed in the 1.6 mm bare weld, which was attributed to the formation of the deep pits on the face of this weld.

The location of pits on the 1.6 mm bare weld were related to the most active corrosion potential of the HAZ/TMAZ border, compared to the potentials of other zones, which may lead to local galvanic corrosion between the weld zones. The low amount of pitting on the 3.2 mm Alclad weld was related to a high corrosion resistance and low corrosion current density of the weld zones.

4) How effective is Alclad as a corrosion protection method for SSFSW'd joints, and is Alclad feasible in terms of impact on mechanical properties and macrostructural features?

Alclad is an effective but not feasible corrosion protection method for the welds, since less pitting corrosion but larger loss in ductility were observed in the Alclad welds, compared to the bare weld.

5) Which weld configuration (1.6 mm bare, 1.6 mm Alclad, 3.2 mm Alclad) performs best with respect to the mechanical and corrosion properties?

Based on the microhardness and tensile properties, the 1.6 mm bare weld performed best, followed by the 1.6 mm Alclad weld and 3.2 mm Alclad weld. The reverse is true with respect to the corrosion properties. Overall, the 1.6 mm bare weld performs best overall due higher microhardness and tensile properties, lack of cladding mixed into the weld, and the availability of other corrosion protection methods.

6) How do the SSFSW'd joints compare to FSW'd joints from literature, with respect to the macrostructural features, mechanical properties and corrosion behaviour?

Smaller TMAZ and HAZ and lower surface roughness were observed in the stationary shoulder friction stir welds compared to friction stir welds from literature. Better weld efficiency and slightly higher microhardness is achieved across all weld-zones compared to FSW'd joints from literature. Less corrosion damage was observed in the SSFSW'd joints compared to FSW'd joints from literature.

7 Recommendations

The following suggestions are recommended for follow up studies:

1) Relate the size of the weld zones and the distribution and size of intermetallic particles across the welds to the thermal field generated during welding, by measuring the heat distribution using thermos couples at several points along the weld and identifying the IMPs with the help of SEM/TEM and XRD. Next, relate the mechanical and corrosion properties to these IMPs.
2) To fully understand the impact of tool pin design on material flow, heat cycle, recrystallisation, recovery and precipitation it is recommended to perform a subsequent study into this effect by varying the tool pin design and length and recording the subsequent parameters.
3) Perform fractography on the fractured surfaces of uncorroded and corroded weld specimens using SEM, to identify local fracture mechanisms and specific locations of fracturing, and to possibly find a relationship between the corrosion and fracture mechanisms. This can be combined with electron backscatter diffraction (EBSD) for texture maps of the macrostructure and digital image correlation (DIC) during tensile testing, which help identify aligned slip planes and low ductility zones.
4) Investigate other corrosion protection methods such as post-weld anodisation and coatings, to avoid weld defects and improve corrosion resistance. Use salt-spray tests, alternating immersion tests or more aggressive test solutions to accelerate corrosion mechanisms on the anodised layer or coating. Longer exposure times up to at least several days are preferred, in order to observe any meaningful corrosion damage. Shear tests or bending tests should be applied according to industry standards to test bonding of the layers. Fractography needs to be applied afterwards to determine the bonding.
5) Test the welds' fatigue life, fracture toughness and determine the susceptibility to intergranular corrosion, stress corrosion cracking and corrosion fatigue, as these are important aspects in aerospace industry.
6) Remove cladding before performing electrochemical measurements (OCP, LPR, potentiodynamic) on the cross-section of the weld, to take out the influence of cladding on these values. Use less aggressive test solutions when using small sized electrochemical cells (1 mm diameter).
7) To fully show the possible effect of a smaller TMAZ and HAZ on the weld properties, a study should be performed in which both conventional and stationary shoulder friction stir welds of similar material and thickness are characterised with respect to macrostructure, microstructure, mechanical properties and corrosion behaviour. Otherwise, a study should be performed to test the effect of several variations of weld parameters (most importantly tool travel speed and rotation speed) on the size of the weld zones and corresponding corrosion properties of SSFSW'd joints only, since these parameters influence the heat generation and corresponding sizes of the weld zones the most. In either study, the corrosion properties should be tested under the same test conditions to make a valid comparison.

Acknowledgements

In this part of the thesis I would like to acknowledge and thank those who helped me during this project. First, I would like to express my deepest appreciation to GKN Fokker for providing me with and trusting me with this amazing project. Second, I would like to thank my supervisors Arjan Mol, Daniela Danciu, Andrew den Bakker and Louis Mcbride, for their availability, insights, tips, and guidance throughout the project.

Major thanks go out to Agnieszka Kooijman for teaching me how to do the electrochemical measurements, helping with ideation and suggestions for test setups. Special thanks go out to María Terol Sánchez and Ragnheidur Benonisdottir, for not only being valuable friends and support, but also for teaching me sanding, polishing, optical microscopy and hardness testing. I am also grateful to Gianni Ling for helping me understand how to perform and analyse white light interferometry. Furthermore, I would like to thank Sean Scott, Arjan Cornet, Ali Kosari and Can Özkan for their valuable discussions, teachings and interesting talks.

Next, I would like to acknowledge the help from Jeroen den Backer from The Welding Institute and Pablo Coladasmato from GKN Aerospace, for their help with supplying the welded sheets and taxes/border issues. Special thanks go out to the people at DEMO as well, for supplying the specimens quickly and precisely.

Many thanks go to my friends and family as well. I would like to thank my parents in particular, for supporting me all these years during my studies. Their unconditional love, trust and support has been and will always be much appreciated. Last but not least, I am very grateful to Selina for her love, patience and support throughout these past two years.

References

[1] GKN Aerospace, "Corporate brochure," GKN Aerospace, Tech. Rep., Jul. 2022. [Online]. Available: https://www.gknaerospace.com/en/newsroom/downloadable-materials/.

[2] The Business Research Company, "Aerospace global market report 2022," The Business Research Company, Tech. Rep., Oct. 2022. [Online]. Available: https://www.thebusinessresearchcompany.com/report/aerospace-global-market-report.

[3] E. B. Salas, *Projected size of the global aircraft fleet due to coronavirus outbreak from 2020 to 2032*, Online, Apr. 2022. [Online]. Available: https://www.statista.com/statistics/282237/aircraft-fleet-size.

[4] R. Lumley, "1 - introduction to aluminium metallurgy," in *Fundamentals of Aluminium Metallurgy*, ser. Woodhead Publishing Series in Metals and Surface Engineering, R. Lumley, Ed., Woodhead Publishing, 2011, pp. 1–19, ISBN: 978-1-84569-654-2. DOI: https://doi.org/10.1533/9780857090256.1. [Online]. Available: https://www.sciencedirect.com/science/article/pii/B9781845696542500018.

[5] F. Campbell, "Chapter 1 - introduction," in *Manufacturing Technology for Aerospace Structural Materials*, F. Campbell, Ed., Oxford: Elsevier Science, 2006, pp. 1–13, ISBN: 978-1-85617-495-4. DOI: https://doi.org/10.1016/B978-185617495-4/50001-9. [Online]. Available: https://www.sciencedirect.com/science/article/pii/B9781856174954500019.

[6] E. Starke and J. Staley, "24 - application of modern aluminium alloys to aircraft," in *Fundamentals of Aluminium Metallurgy*, ser. Woodhead Publishing Series in Metals and Surface Engineering, R. Lumley, Ed., Woodhead Publishing, 2011, pp. 747–783, ISBN: 978-1-84569-654-2. DOI: https://doi.org/10.1533/9780857090256.3.747. [Online]. Available: https://www.sciencedirect.com/science/article/pii/B9781845696542500249.

[7] A. Squillace, A. De Fenzo, G. Giorleo, and F. Bellucci, "A comparison between fsw and tig welding techniques: Modifications of microstructure and pitting corrosion resistance in aa 2024-t3 butt joints," *Journal of Materials Processing Technology*, vol. 152, no. 1, pp. 97–105, 2004, ISSN: 0924-0136. DOI: https://doi.org/10.1016/j.jmatprotec.2004.03.022. [Online]. Available: https://www.sciencedirect.com/science/article/pii/S0924013604004339.

[8] P. L. Threadgill, A. J. Leonard, H. R. Shercliff, and P. J. Withers, "Friction stir welding of aluminium alloys," *International Materials Reviews*, vol. 54, no. 2, pp. 49–93, 2009. DOI: 10.1179/174328009X411136. [Online]. Available: https://doi.org/10.1179/174328009X411136.

[9] R. Rai, A. De, H. K. D. H. Bhadeshia, and T. DebRoy, "Review: Friction stir welding tools," *Science and Technology of Welding and Joining*, vol. 16, no. 4, pp. 325–342, 2011. DOI: 10.1179/1362171811Y.0000000023. [Online]. Available: https://doi.org/10.1179/1362171811Y.0000000023.

[10] T. Majeed, Y. Mehta, and A. N. Siddiquee, "Precipitation-dependent corrosion analysis of heat treatable aluminum alloys via friction stir welding, a review," *Proceedings of the Institution of Mechanical Engineers, Part C: Journal of Mechanical Engineering Science*, p. 09 544 062 211 003 609, 2021. DOI: 10.1177/09544062211003609. [Online]. Available: https://doi.org/10.1177/09544062211003609.

[11] W. M. Thomas, E. D. Nicholas, J. C. Needham, M. G. Murch, P. Temple-Smith, and C. J. Dawes, "Friction welding," U.S. Patent 5 460 317, Dec. 1991. [Online]. Available: https://patents.google.com/patent/US5460317A.

[12] M. Jones, P. Heurtier, C. Desrayaud, F. Montheillet, D. Allehaux, and J. Driver, "Correlation between microstructure and microhardness in a friction stir welded 2024 aluminium alloy," *Scripta Materialia*, vol. 52, no. 8, pp. 693–697, 2005, ISSN: 1359-6462. DOI: https://doi.org/10.1016/j.scriptamat.2004.12.027. [Online]. Available: https://www.sciencedirect.com/science/article/pii/S1359646204007201.

[13] M. J. Russell, C. Blignault, N. L. Horrex, and C. S. Wiesner, "Recent developments in the friction stir welding of titanium alloys," *Welding in the World : The International Journal of Materials Joining*, vol. 52, no. 9-10, pp. 12–15, 2008, 12, ISSN: 0043-2288. DOI: 10.1007/BF03266662. [Online]. Available: https://doi.org/10.1007/BF03266662.

[14] H. Wu, Y.-C. Chen, D. Strong, and P. Prangnell, "Stationary shoulder fsw for joining high strength aluminum alloys," *Journal of Materials Processing Technology*, vol. 221, pp. 187–196, 2015, ISSN: 0924-0136. DOI: https://doi.org/10.1016/j.jmatprotec.2015.02.015. [Online]. Available: https://www.sciencedirect.com/science/article/pii/S0924013615000588.

[15] T. Warner, M. Schmidt, F. Sommer, and D. Bellot, "Characterisation of corrosion initiation on 2024 aluminium alloy by atomic force microscopy," *International Journal of Materials Research*, vol. 86, no. 7, pp. 494–502, 1995. DOI: doi:10.1515/ijmr-1995-860708. [Online]. Available: https://doi.org/10.1515/ijmr-1995-860708.

[16] V. Guillaumin and G. Mankowski, "Localized corrosion of 2024 t351 aluminium alloy in chloride media," *Corrosion Science*, vol. 41, no. 3, pp. 421–438, 1998, ISSN: 0010-938X. DOI: https://doi.org/10.1016/S0010-938X(98)00116-4. [Online]. Available: https://www.sciencedirect.com/science/article/pii/S0010938X98001164.

[17] P. Leblanc and G. S. Frankel, "A study of corrosion and pitting initiation of AA2024-t3 using atomic force microscopy," *Journal of The Electrochemical Society*, vol. 149, no. 6, B239, 2002. DOI: 10.1149/1.1471546. [Online]. Available: https://doi.org/10.1149/1.1471546.

[18] F. Queiroz, M. Magnani, I. Costa, and H. de Melo, "Investigation of the corrosion behaviour of aa 2024-t3 in low concentrated chloride media," *Corrosion Science*, vol. 50, no. 9, pp. 2646–2657, 2008, ISSN: 0010-938X. DOI: https://doi.org/10.1016/j.corsci.2008.06.041. [Online]. Available: https://www.sciencedirect.com/science/article/pii/S0010938X08002278.

[19] A. Boag, R. Taylor, T. Muster, N. Goodman, D. McCulloch, C. Ryan, B. Rout, D. Jamieson, and A. Hughes, "Stable pit formation on aa2024-t3 in a nacl environment," *Corrosion Science*, vol. 52, no. 1, pp. 90–103, 2010, ISSN: 0010-938X. DOI: https://doi.org/10.1016/j.corsci.2009.08.043. [Online]. Available: https://www.sciencedirect.com/science/article/pii/S0010938X09004090.

[20] A. Boag, A. Hughes, A. Glenn, T. Muster, and D. McCulloch, "Corrosion of aa2024-t3 part i: Localised corrosion of isolated im particles," *Corrosion Science*, vol. 53, no. 1, pp. 17–26, 2011, ISSN: 0010-938X. DOI: https://doi.org/10.1016/j.corsci.2010.09.009. [Online]. Available: https://www.sciencedirect.com/science/article/pii/S0010938X10004403.

[21] A. Hughes, A. Boag, A. Glenn, D. McCulloch, T. Muster, C. Ryan, C. Luo, X. Zhou, and G. Thompson, "Corrosion of aa2024-t3 part ii: Co-operative corrosion," *Corrosion Science*, vol. 53, no. 1, pp. 27–39, 2011, ISSN: 0010-938X. DOI: https://doi.org/10.1016/j.corsci.2010.09.030. [Online]. Available: https://www.sciencedirect.com/science/article/pii/S0010938X10004610.

[22] A. Glenn, T. Muster, C. Luo, X. Zhou, G. Thompson, A. Boag, and A. Hughes, "Corrosion of aa2024-t3 part iii: Propagation," *Corrosion Science*, vol. 53, no. 1, pp. 40–50, 2011, ISSN: 0010-938X. DOI: https://doi.org/10.1016/j.corsci.2010.09.035. [Online]. Available: https://www.sciencedirect.com/science/article/pii/S0010938X1000466X.

[23] X. Zhou, C. Luo, T. Hashimoto, A. Hughes, and G. Thompson, "Study of localized corrosion in aa2024 aluminium alloy using electron tomography," *Corrosion Science*, vol. 58, pp. 299–306, 2012, ISSN: 0010-938X. DOI: https://doi.org/10.1016/j.corsci.2012.02.001. [Online]. Available: https://www.sciencedirect.com/science/article/pii/S0010938X12000807.

[24] J. Wang, B. Zhang, B. Wu, and X. Ma, "Size-dependent role of s phase in pitting initiation of 2024al alloy," *Corrosion Science*, vol. 105, pp. 183–189, 2016, ISSN: 0010-938X. DOI: https://doi.org/10.1016/j.corsci.2016.01.016. [Online]. Available: https://www.sciencedirect.com/science/article/pii/S0010938X16300166.

[25] T. Hashimoto, X. Zhang, X. Zhou, P. Skeldon, S. Haigh, and G. Thompson, "Investigation of dealloying of s phase (al2cumg) in aa 2024-t3 aluminium alloy using high resolution 2d and 3d electron imaging," *Corrosion Science*, vol. 103, pp. 157–164, 2016, ISSN: 0010-938X. DOI: https://doi.org/10.1016/j.corsci.2015.11.013. [Online]. Available: https://www.sciencedirect.com/science/article/pii/S0010938X15301554.

[26] S. Pantelakis, D. Setsika, A. Chamos, and A. Zervaki, "Corrosion damage evolution of the aircraft aluminum alloy 2024 t3," *International Journal of Structural Integrity*, vol. 7, no. 1, pp. 25–46, Jan. 2016, ISSN: 1757-9864. DOI: 10.1108/IJSI-03-2014-0010. [Online]. Available: https://doi.org/10.1108/IJSI-03-2014-0010.

[27] G. Biallas, R. Braun, C. D. Donne, G. Staniek, and W. A. Kaysser, "Mechanical properties and corrosion behaviour of friction stir welded 2024-t351 aluminium joints," in *Proceedings of 1st International Friction Stir Welding Symposium: 14-16 June 1999, 1000 Oaks, CA, USA*, TWI Ltd and National Research Council Canada, 1999. [Online]. Available: https://www.tib.eu/en/search/id/TIBKAT:314661700/Friction-Stir-Welding-Symposium-14-16-June-1999.

[28] A. Davenport, R. Ambat, M. Jariyaboon, P. Morgan, D. Price, A. Wescott, and S. Williams, "Corrosion of friction stir welds in high strength aluminium alloys," *Journal of Corrosion Science and Engineering*, vol. 6, Jan. 2003.

[29] B. J. Connolly, A. J. Davenport, M. Jariyaboon, C. Padovani, R. Ambat, S. W. Williams, D. A. Price, A. Wescott, C. Goodfellow, and C.-M. Lee, "Localised corrosion of friction stir welds in aluminium alloys, 5th:; international symposium, friction stir welding," in *Friction stir welding, 5th:; International Symposium, Friction stir welding*, TWI Ltd.,; 2004, P9, ISBN: 1903761042. [Online]. Available: https://www.tib.eu/de/suchen/id/BLCP%5C%3ACN057436486.

[30] M. Jariyaboon, A. Davenport, R. Ambat, B. Connolly, S. Williams, and D. Price, "The effect of welding parameters on the corrosion behaviour of friction stir welded aa2024–t351," *Corrosion Science*, vol. 49, no. 2, pp. 877–909, 2007, ISSN: 0010-938X. DOI: https://doi.org/10.1016/j.corsci.2006.05.038. [Online]. Available: https://www.sciencedirect.com/science/article/pii/S0010938X06001788.

[31] X. Zhou, Y. Younes, D. Wadeson, T. Hashimoto, and G. E. Thompson, "Corrosion control of friction stir welded aluminium airframe alloy," in *Corrosion in the Military II*, ser. Advanced Materials Research, vol. 38, Trans Tech Publications Ltd, Apr. 2008, pp. 298–305. DOI: 10.4028/www.scientific.net/AMR.38.298.

[32] E. Bousquet, A. Poulon-Quintin, M. Puiggali, O. Devos, and M. Touzet, "Relationship between microstructure, microhardness and corrosion sensitivity of an aa 2024-t3 friction stir welded joint," *Corrosion Science*, vol. 53, no. 9, pp. 3026–3034, 2011, ISSN: 0010-938X. DOI: https://doi.org/10.1016/j.corsci.2011.05.049. [Online]. Available: https://www.sciencedirect.com/science/article/pii/S0010938X1100271X.

[33] A. E. Hughes, N. Birbilis, J. M. Mol, S. J. Garcia, X. Zhou, and G. E. Thompson, "High strength al-alloys: Microstructure, corrosion and principles of protection," in *Recent Trends in Processing and Degradation of Aluminium Alloys*, Z. Ahmad, Ed., Rijeka: IntechOpen, 2011, ch. 10. DOI: 10.5772/18766. [Online]. Available: https://doi.org/10.5772/18766.

[34] A. E. Hughes, J. M. Mol, M. L. Zheludkevich, and R. G. Buchheit, Eds., *Active Protective Coatings*, 1st ed. Springer, Dordrecht, 2016, ISBN: 978-94-017-7538-0. DOI: https://doi.org/10.1007/978-94-017-7540-3. [Online]. Available: https://link.springer.com/book/10.1007/978-94-017-7540-3.

[35] F. Campbell, "Chapter 2 - aluminum," in *Manufacturing Technology for Aerospace Structural Materials*, F. Campbell, Ed., Oxford: Elsevier Science, 2006, pp. 15–92, ISBN: 978-1-85617-495-4. DOI: https://doi.org/10.1016/B978-185617495-4/50002-0. [Online]. Available: https://www.sciencedirect.com/science/article/pii/B9781856174954500020.

[36] C. Vargel, *Corrosion of Aluminium (Second Edition)*, Second Edition, C. Vargel, Ed. Amsterdam: Elsevier Science Ltd, 2020, ISBN: 978-0-08-099925-8. [Online]. Available: https://www.sciencedirect.com/book/9780080999258/corrosion-of-aluminium.

[37] Z. Zhang, B. L. Xiao, D. Wang, and Z. Y. Ma, "Effect of alclad layer on material flow and defect formation in friction-stir-welded 2024 aluminum alloy," *Metallurgical and Materials Transactions A*, vol. 42, no. 6, pp. 1717–1726, Jun. 2011, ISSN: 1543-1940. DOI: 10.1007/s11661-010-0545-3. [Online]. Available: https://doi.org/10.1007/s11661-010-0545-3.

[38] A. Drozdov, *Aluminium: The Thirteenth Element*, E. Shanina, Ed. The RUSAL Library, 2007, ISBN: 978-5-91523-002-5.

[39] I. Polmear, "3 - wrought aluminium alloys," in *Light Alloys (Fourth Edition)*, I. Polmear, Ed., Fourth Edition, Oxford: Butterworth-Heinemann, 2005, pp. 97–204, ISBN: 978-0-7506-6371-7. DOI: https://doi.org/10.1016/B978-075066371-7/50007-4. [Online]. Available: https://www.sciencedirect.com/science/article/pii/B9780750663717500074.

[40] R. S. Mishra and H. Sidhar, *Friction stir welding of 2xxx aluminum alloys including Al–Li alloys*. Butterworth-Heinemann, 2017, ISBN: 9780128053683.

[41] T. Dursun and C. Soutis, "Recent developments in advanced aircraft aluminium alloys," *Materials & Design (1980-2015)*, vol. 56, pp. 862–871, 2014, ISSN: 0261-3069. DOI: https://doi.org/10.1016/j.matdes.2013.12.002. [Online]. Available: https://www.sciencedirect.com/science/article/pii/S0261306913011357.

[42] H. Kvande, "3 - production of primary aluminium," in *Fundamentals of Aluminium Metallurgy*, ser. Woodhead Publishing Series in Metals and Surface Engineering, R. Lumley, Ed., Woodhead Publishing, 2011, pp. 49–69, ISBN: 978-1-84569-654-2. DOI: https://doi.org/10.1533/9780857090256.1.49. [Online]. Available: https://www.sciencedirect.com/science/article/pii/B9781845696542500031.

[43] J. Grandfield, "5 - ingot casting and casthouse metallurgy of aluminium and its alloys," in *Fundamentals of Aluminium Metallurgy*, ser. Woodhead Publishing Series in Metals and Surface Engineering, R. Lumley, Ed., Woodhead Publishing, 2011, pp. 83–140, ISBN: 978-1-84569-654-2. DOI: https://doi.org/10.1533/9780857090256.1.83. [Online]. Available: https://www.sciencedirect.com/science/article/pii/B9781845696542500055.

[44] The Aluminum Association, *International Alloy Designations and Chemical Composition Limits for Wrought Aluminum and Wrought Aluminum Alloys*, 1400 Crystal Drive, Suite 430, Arlington, VA 22209, Aug. 2018. [Online]. Available: https://www.aluminum.org/sites/default/files/Teal%5C%20Sheet.pdf.

[45] ASTM International, *ASTM B209 / B209M-21, Standard Specification for Aluminum and Aluminum-Alloy Sheet and Plate*, West Conshohocken, PA, 2021. [Online]. Available: http://www.astm.org/cgi-bin/resolver.cgi?B209B209M.

[46] R. G. Buchheit, R. P. Grant, P. F. Hlava, B. Mckenzie, and G. L. Zender, "Local dissolution phenomena associated with s phase (al2cumg) particles in aluminium alloy 2024-t3," *Journal of The Electrochemical Society*, vol. 144, no. 8, p. 2621, Aug. 1997. DOI: 10.1149/1.1837874. [Online]. Available: https://dx.doi.org/10.1149/1.1837874.

[47] Nederlands Normalisatie-instituut, *NEN-EN 515:2017 en, Aluminium and aluminium alloys - Wrought products - Temper designations*, Mar. 2017. [Online]. Available: https://www.nen.nl/nen-en-515-2017-en-231525.

[48] J. G. Kaufman, "Properties and Applications of Wrought Aluminum Alloys," in *Properties and Selection of Aluminum Alloys*, ASM International, Jun. 2019, ISBN: 978-1-62708-210-5. DOI: 10.31399/asm.hb.v02b.a0006543. [Online]. Available: https://doi.org/10.31399/asm.hb.v02b.a0006543.

[49] CEN, *NEN-EN 12258-1:2012 en;fr;de, Aluminium and aluminium alloys - Terms and definitions - Part 1: General terms*, Jun. 2012. [Online]. Available: https://www.nen.nl/nen-en-12258-1-2012-en-fr-de-172646.

[50] ASM International, *Aluminum: Properties and Physical Metallurgy*, J. E. Hatch, Ed. Aluminum Association Inc. and ASM International, 1984, ISBN: 978-0-87170-176-3. [Online]. Available: https://www.asminternational.org/home/-/journal_content/56/10192/06236G/PUBLICATION/.

[51] N. Saunders, "Phase diagram calculations for commercial al-alloys," in *Materials Science Forum*, Trans Tech Publ, vol. 217, 1996, pp. 667–672.

[52] T. Buhler, S. G. Fries, P. J. Spencer, and H. L. Lukas, "A thermodynamic assessment of the al-cu-mg ternary system," *Journal of Phase Equilibria*, vol. 19, no. 4, pp. 317–333, Aug. 1998, ISSN: 1054-9714. DOI: 10.1361/105497198770342058. [Online]. Available: https://doi.org/10.1361/105497198770342058.

[53] S. Ringer and K. Hono, "Microstructural evolution and age hardening in aluminium alloys: Atom probe field-ion microscopy and transmission electron microscopy studies," *Materials Characterization*, vol. 44, no. 1, pp. 101–131, 2000, ISSN: 1044-5803. DOI: https://doi.org/10.1016/S1044-5803(99)00051-0. [Online]. Available: https://www.sciencedirect.com/science/article/pii/S1044580399000510.

[54] R. C. Dorward and S. D. Kennedy, "Method of manufacturing aluminum aircraft sheet," English, U.S. Patent 5 938 867, Mar. 1997. [Online]. Available: https://patents.google.com/patent/US5938867A.

[55] G. Effenberg, A. Prince, O. A. Bieloborodova, L. Gulay, F. Hayes, M. Harmelin, H. Leo, and T. Yanson, "Aluminium - copper - magnesium," 2003. [Online]. Available: https://www.semanticscholar.org/paper/Aluminium-Copper-Magnesium-Effenberg-Prince/47dbbfd7fa971591793cbd0b63162713c36f32c1.

[56] N. A. Belov, D. G. Eskin, and A. A. Aksenov, "Chapter 5 - alloys of the al–cu–mn–(mg, fe, si) system," in *Multicomponent Phase Diagrams*, N. A. Belov, D. G. Eskin, and A. A. Aksenov, Eds., Oxford: Elsevier, 2005, pp. 159–192, ISBN: 978-0-08-044537-3. DOI: https://doi.org/10.1016/B978-008044537-3/50005-6. [Online]. Available: https://www.sciencedirect.com/science/article/pii/B9780080445373500056.

[57] V. Raghavan, "Al-cu-mg (aluminum-copper-magnesium)," *Journal of Phase Equilibria and Diffusion*, vol. 28, no. 2, pp. 174–179, Apr. 2007, ISSN: 1863-7345. DOI: 10.1007/s11669-007-9045-6. [Online]. Available: https://doi.org/10.1007/s11669-007-9045-6.

[58] N. A. Belov and N. N. Avksent'eva, "Quantitative analysis of the al – cu – mg – mn – si phase diagram as applied to commercial aluminum alloys of series 2xxx," *Metal Science and Heat Treatment*, vol. 55, no. 7, pp. 358–363, Nov. 2013, ISSN: 1573-8973. DOI: 10.1007/s11041-013-9635-3. [Online]. Available: https://doi.org/10.1007/s11041-013-9635-3.

[59] A. E. Hughes, R. Parvizi, and M. Forsyth, "Microstructure and corrosion of aa2024," *Corrosion Reviews*, vol. 33, no. 1-2, pp. 1–30, 2015. DOI: doi:10.1515/corrrev-2014-0039. [Online]. Available: https://doi.org/10.1515/corrrev-2014-0039.

[60] S. C. Wang and M. J. Starink, "Precipitates and intermetallic phases in precipitation hardening al–cu–mg–(li) based alloys," *International Materials Reviews*, vol. 50, no. 4, pp. 193–215, 2005. DOI: 10.1179/174328005X14357. [Online]. Available: https://doi.org/10.1179/174328005X14357.

[61] N. Birbilis, Y. Zhu, S. Kairy, M. Glenn, J.-F. Nie, A. Morton, Y. Gonzalez-Garcia, H. Terryn, J. Mol, and A. Hughes, "A closer look at constituent induced localised corrosion in al-cu-mg alloys," *Corrosion Science*, vol. 113, pp. 160–171, 2016, ISSN: 0010-938X. DOI: https://doi.org/10.1016/j.corsci.2016.10.018. [Online]. Available: https://www.sciencedirect.com/science/article/pii/S0010938X16310071.

[62] S. Wang and M. Starink, "Two types of s phase precipitates in al–cu–mg alloys," *Acta Materialia*, vol. 55, no. 3, pp. 933–941, 2007, ISSN: 1359-6454. DOI: https://doi.org/10.1016/j.actamat.2006.09.015. [Online]. Available: https://www.sciencedirect.com/science/article/pii/S1359645406006707.

[63] J. V. de Sousa Araujo, M. X. Milagre, R. O. Ferreira, C. de Souza Carvalho Machado, C. P. de Abreu, and I. Costa, "Microstructural characteristics of the al alloys: The dissimilarities among the 2xxx alloys series used in aircraft structures," *Metallography, Microstructure, and Analysis*, vol. 9, no. 5, pp. 744–758, Oct. 2020, ISSN: 2192-9270. DOI: 10.1007/s13632-020-00688-5. [Online]. Available: https://doi.org/10.1007/s13632-020-00688-5.

[64] C. Luo, "Role of microstructure on corrosion control of aa2024-t3 aluminium alloy," Ph.D. dissertation, The University of Manchester, Jul. 2011. [Online]. Available: https://www.research.manchester.ac.uk/portal/en/theses/role-of-microstructure-on-corrosion-control-of-aa2024t3-aluminium-alloy(6954f1a8-920e-4242-bfb4-437be7d27127).html.

[65] A. Kosari, F. Tichelaar, P. Visser, H. Zandbergen, H. Terryn, and J. Mol, "Dealloying-driven local corrosion by intermetallic constituent particles and dispersoids in aerospace aluminium alloys," *Corrosion Science*, vol. 177, p. 108 947, 2020, ISSN: 0010-938X. DOI: https://doi.org/10.1016/j.corsci.2020.108947. [Online]. Available: https://www.sciencedirect.com/science/article/pii/S0010938X20316097.

[66] A. Kosari, H. Zandbergen, F. Tichelaar, P. Visser, P. Taheri, H. Terryn, and J. Mol, "In-situ nanoscopic observations of dealloying-driven local corrosion from surface initiation to in-depth propagation," *Corrosion Science*, vol. 177, p. 108 912, 2020, ISSN: 0010-938X. DOI: https://doi.org/10.1016/j.corsci.2020.108912. [Online]. Available: https://www.sciencedirect.com/science/article/pii/S0010938X20315201.

[67] A. Boag, A. Hughes, N. Wilson, A. Torpy, C. MacRae, A. Glenn, and T. Muster, "How complex is the microstructure of aa2024-t3?" *Corrosion Science*, vol. 51, no. 8, pp. 1565–1568, 2009, ISSN: 0010-938X. DOI: https://doi.org/10.1016/j.corsci.2009.05.001. [Online]. Available: https://www.sciencedirect.com/science/article/pii/S0010938X0900184X.

[68] A. Staszczyk, J. Sawicki, and B. Adamczyk-Cieslak, "A study of second-phase precipitates and dispersoid particles in 2024 aluminum alloy after different aging treatments," *Materials*, vol. 12, no. 24, 2019, ISSN: 1996-1944. DOI: 10.3390/ma12244168. [Online]. Available: https://www.mdpi.com/1996-1944/12/24/4168.

[69] A. E. Hughes, A. M. Glenn, N. Wilson, A. Moffatt, A. J. Morton, and R. G. Buchheit, "A consistent description of intermetallic particle composition: An analysis of ten batches of aa2024-t3," *Surface and Interface Analysis*, vol. 45, no. 10, pp. 1558–1563, 2013. DOI: https://doi.org/10.1002/sia.5207. [Online]. Available: https://analyticalsciencejournals.onlinelibrary.wiley.com/doi/abs/10.1002/sia.5207.

[70] F. M. Queiroz, M. Terada, A. F. S. Bugarin, H. G. de Melo, and I. Costa, "Comparison of corrosion resistance of the aa2524-t3 and the aa2024-t3," *Metals*, vol. 11, no. 6, 2021, ISSN: 2075-4701. DOI: 10.3390/met11060980. [Online]. Available: https://www.mdpi.com/2075-4701/11/6/980.

[71] A. E. Hughes, C. MacRae, N. Wilson, A. Torpy, T. H. Muster, and A. M. Glenn, "Sheet aa2024-t3: A new investigation of microstructure and composition," *Surface and Interface Analysis*, vol. 42, no. 4,

pp. 334–338, 2010. DOI: https://doi.org/10.1002/sia.3163. [Online]. Available: https://analyticalsciencejournals.onlinelibrary.wiley.com/doi/abs/10.1002/sia.3163.

[72] A. Merati, "Corrosion Fatigue and Environmentally Assisted Cracking in Aging Military Vehicles," in M. Colavita, Ed., ser. RTO-AG-AVT-140. RTO/NATO, Mar. 2011, ch. Chapter 24 – Materials Replacement for Aging Aircraft, pp. 337–358, ISBN: 978-92-837-0125-5. DOI: 10.14339/RTO-AG-AVT-140-ALL-pdf. [Online]. Available: https://www.sto.nato.int/publications/STO%20Technical%20Reports/RTO-AG-AVT-140/$$AG-AVT-140-ALL.pdf.

[73] A. K. Shettigar and M. Manjaiah, "Friction stir welding—an overview," in *Advanced Manufacturing Technologies: Modern Machining, Advanced Joining, Sustainable Manufacturing*, K. Gupta, Ed. Cham: Springer International Publishing, 2017, pp. 161–184, ISBN: 978-3-319-56099-1. DOI: 10.1007/978-3-319-56099-1_7. [Online]. Available: https://doi.org/10.1007/978-3-319-56099-1_7.

[74] P. H. Shah and V. J. Badheka, "Friction stir welding of aluminium alloys: An overview of experimental findings – process, variables, development and applications," *Proceedings of the Institution of Mechanical Engineers, Part L: Journal of Materials: Design and Applications*, vol. 233, no. 6, pp. 1191–1226, 2019. DOI: 10.1177/1464420716689588. [Online]. Available: https://doi.org/10.1177/1464420716689588.

[75] M. H. El-Moayed, A. Y. Shash, M. A. Rabou, and M. G. El-Sherbiny, "A detailed process design for conventional friction stir welding of aluminum alloys and an overview of related knowledge," *Engineering Reports*, vol. 3, no. 2, e12270, 2021, e12270 ENG-2019-12-0874.R1. DOI: https://doi.org/10.1002/eng2.12270. [Online]. Available: https://onlinelibrary.wiley.com/doi/abs/10.1002/eng2.12270.

[76] M. M. El-Sayed, A. Shash, M. Abd-Rabou, and M. G. ElSherbiny, "Welding and processing of metallic materials by using friction stir technique: A review," *Journal of Advanced Joining Processes*, vol. 3, p. 100 059, 2021, ISSN: 2666-3309. DOI: https://doi.org/10.1016/j.jajp.2021.100059. [Online]. Available: https://www.sciencedirect.com/science/article/pii/S2666330921000194.

[77] D. F. Braga, S. Eslami, and P. Moreira, "Chapter 5 - friction stir welding," in *Advanced Joining Processes*, L. da Silva, M. El-Zein, and P. Martins, Eds., Elsevier, 2021, pp. 173–206, ISBN: 978-0-12-820787-1. DOI: https://doi.org/10.1016/B978-0-12-820787-1.00005-X. [Online]. Available: https://www.sciencedirect.com/science/article/pii/B978012820787100005X.

[78] R. S. Mishra, P. S. De, and N. Kumar, "Introduction," in *Friction Stir Welding and Processing: Science and Engineering*. Cham: Springer International Publishing, 2014, pp. 1–11, ISBN: 978-3-319-07043-8. DOI: 10.1007/978-3-319-07043-8_1. [Online]. Available: https://doi.org/10.1007/978-3-319-07043-8_1.

[79] R. Nandan, T. DebRoy, and H. Bhadeshia, "Recent advances in friction-stir welding – process, weldment structure and properties," *Progress in Materials Science*, vol. 53, no. 6, pp. 980–1023, 2008, ISSN: 0079-6425. DOI: https://doi.org/10.1016/j.pmatsci.2008.05.001. [Online]. Available: https://www.sciencedirect.com/science/article/pii/S007964250800039X.

[80] Z. Y. Ma, A. H. Feng, D. L. Chen, and J. Shen, "Recent advances in friction stir welding/processing of aluminum alloys: Microstructural evolution and mechanical properties," *Critical Reviews in Solid State and Materials Sciences*, vol. 43, no. 4, pp. 269–333, 2018. DOI: 10.1080/10408436.2017.1358145. [Online]. Available: https://doi.org/10.1080/10408436.2017.1358145.

[81] B. Meyghani and C. Wu, "Progress in thermomechanical analysis of friction stir welding," *Chinese Journal of Mechanical Engineering (English Edition)*, vol. 33, no. 1, 2020, ISSN: 10009345. DOI: 10.1186/s10033-020-0434-7.

[82] D. Jacquin and G. Guillemot, "A review of microstructural changes occurring during fsw in aluminium alloys and their modelling," *Journal of Materials Processing Technology*, vol. 288, p. 116 706, 2021, ISSN: 0924-0136. DOI: https://doi.org/10.1016/j.jmatprotec.2020.116706. [Online]. Available: https://www.sciencedirect.com/science/article/pii/S0924013620301205.

[83] J. You, Y. Zhao, C. Dong, Y. Yi, and Y. Su, "Numerical modeling of multiphysics field in conventional and stationary shoulder friction stir welding of al-cu alloy," *Journal of Materials Engineering and Performance*, vol. 30, no. 4, pp. 2751–2760, 2021, ISSN: 10599495. DOI: 10.1007/s11665-021-05642-2.

[84] I. Radisavljevic, A. Zivkovic, N. Radovic, and V. Grabulov, "Influence of fsw parameters on formation quality and mechanical properties of al 2024-t351 butt welded joints," *Transactions of Nonferrous Metals Society of China*, vol. 23, no. 12, pp. 3525–3539, 2013, ISSN: 1003-6326. DOI: https://doi.org/10.1016/S1003-6326(13)62897-6. [Online]. Available: https://www.sciencedirect.com/science/article/pii/S1003632613628976.

[85] D. Trimble, G. O'Donnell, and J. Monaghan, "Characterisation of tool shape and rotational speed for increased speed during friction stir welding of aa2024-t3," *Journal of Manufacturing Processes*, vol. 17, pp. 141–150, 2015, ISSN: 1526-6125. DOI: https://doi.org/10.1016/j.jmapro.2014.08.007. [Online]. Available: https://www.sciencedirect.com/science/article/pii/S1526612514000802.

[86] G. D'Urso, C. Giardini, S. Lorenzi, M. Cabrini, and T. Pastore, "The effects of process parameters on mechanical properties and corrosion behavior in friction stir welding of aluminum alloys," *Procedia Engineering*, vol. 183, pp. 270–276, 2017, 17th International Conference on Sheet Metal, SHEMET17, ISSN: 1877-7058. DOI: https://doi.org/10.1016/j.proeng.2017.04.038. [Online]. Available: https://www.sciencedirect.com/science/article/pii/S1877705817315436.

[87] N. Li, W. Li, Y. Xu, X. Yang, and N. D. Alexopoulos, "Influence of rotation speed on mechanical properties and corrosion sensitivity of friction stir welded aa2024-t3 joints," *Materials and Corrosion*, vol. 69, no. 8, pp. 1016–1024, 2018. DOI: https://doi.org/10.1002/maco.201709960. [Online]. Available: https://onlinelibrary.wiley.com/doi/abs/10.1002/maco.201709960.

[88] A. W. El-Morsy, M. Ghanem, and H. Bahaitham, "Effect of friction stir welding parameters on the microstructure and mechanical properties of aa2024-t4 aluminum alloy," *Engineering, Technology & Applied Science Research*, vol. 8, no. 1, pp. 2493–2498, Feb. 2018. DOI: 10.48084/etasr.1704. [Online]. Available: https://etasr.com/index.php/ETASR/article/view/1704.

[89] A. Heidarzadeh, S. Mironov, R. Kaibyshev, G. Çam, A. Simar, A. Gerlich, F. Khodabakhshi, A. Mostafaei, D. Field, J. Robson, A. Deschamps, and P. Withers, "Friction stir welding/processing of metals and alloys: A comprehensive review on microstructural evolution," *Progress in Materials Science*, vol. 117, p. 100 752, 2021, ISSN: 0079-6425. DOI: https://doi.org/10.1016/j.pmatsci.2020.100752. [Online]. Available: https://www.sciencedirect.com/science/article/pii/S007964252030116X.

[90] V. Legrand, "Modélisation des processus de précipitation et prédiction des propriétés mécaniques résultantes dans les alliages d'aluminium à durcissement structural : Application au soudage par Friction Malaxage (FSW)

de tôles AA2024," This PhD thesis was translated automatically to English using Google Translate., Phd Thesis, Ecole Nationale Supérieure des Mines de Paris, Dec. 2015. [Online]. Available: https://pastel.archives-ouvertes.fr/tel-01565304.

[91] N. Li, Y. Xu, W. Li, P. Niu, and A. Vairis, "Corrosion susceptibility and mechanical properties of friction-stir-welded aa2024-t3 joints," *Welding in the World*, vol. 66, no. 5, pp. 951–960, May 2022, ISSN: 1878-6669. DOI: 10.1007/s40194-022-01282-9. [Online]. Available: https://doi.org/10.1007/s40194-022-01282-9.

[92] Z. Zhang, B. Xiao, and Z. Ma, "Hardness recovery mechanism in the heat-affected zone during long-term natural aging and its influence on the mechanical properties and fracture behavior of friction stir welded 2024al–t351 joints," *Acta Materialia*, vol. 73, pp. 227–239, 2014, ISSN: 1359-6454. DOI: https://doi.org/10.1016/j.actamat.2014.04.021. [Online]. Available: https://www.sciencedirect.com/science/article/pii/S1359645414002602.

[93] S. Ji, Z. Li, Z. Zhou, and L. Zhang, "Microstructure and mechanical property differences between friction stir lap welded joints using rotating and stationary shoulders," *The International Journal of Advanced Manufacturing Technology*, vol. 90, no. 9, pp. 3045–3053, Jun. 2017, ISSN: 1433-3015. DOI: 10.1007/s00170-016-9640-y. [Online]. Available: https://doi.org/10.1007/s00170-016-9640-y.

[94] Z. Xu, Z. Li, Z. Lv, and L. Zhang, "Effect of welding speed on joint features and lap shear properties of stationary shoulder fslwed alclad 2024 al alloy," English, *Journal of Materials Engineering and Performance*, vol. 26, no. 3, pp. 1358–1364, 2017, ISSN: 10599495. DOI: 10.1007/s11665-017-2527-8.

[95] X. Meng, Y. Huang, J. Cao, J. Shen, and J. F. dos Santos, "Recent progress on control strategies for inherent issues in friction stir welding," *Progress in Materials Science*, vol. 115, p. 100 706, 2021, ISSN: 0079-6425. DOI: https://doi.org/10.1016/j.pmatsci.2020.100706. [Online]. Available: https://www.sciencedirect.com/science/article/pii/S0079642520300700.

[96] D. A. Jones, *Principles and prevention of corrosion*, 2nd, B. Stenquis, R. Kernan, and P. Daly, Eds. Upper Saddle River, NJ SE: Prentice Hall, Jan. 1996, p. 572, ISBN: 0-13-359993-0.

[97] N. L. Sukiman, X. Zhou, N. Birbilis, A. Hughes, J. M. C. Mol, S. J. Garcia, X. Zhou, and G. E. Thompson, "Durability and corrosion of aluminium and its alloys: Overview, property space, techniques and developments," in *Aluminium Alloys*, Z. Ahmad, Ed., Rijeka: IntechOpen, 2012, ch. 2. DOI: 10.5772/53752. [Online]. Available: https://doi.org/10.5772/53752.

[98] S. Sun, Q. Zheng, D. Li, and J. Wen, "Long-term atmospheric corrosion behaviour of aluminium alloys 2024 and 7075 in urban, coastal and industrial environments," *Corrosion Science*, vol. 51, no. 4, pp. 719–727, 2009, ISSN: 0010-938X. DOI: https://doi.org/10.1016/j.corsci.2009.01.016. [Online]. Available: https://www.sciencedirect.com/science/article/pii/S0010938X09000407.

[99] S. Pantelakis, A. Chamos, and A. Kermanidis, "A critical consideration for the use of al-cladding for protecting aircraft aluminum alloy 2024 against corrosion," *Theoretical and Applied Fracture Mechanics*, vol. 57, no. 1, pp. 36–42, 2012, ISSN: 0167-8442. DOI: https://doi.org/10.1016/j.tafmec.2011.12.006. [Online]. Available: https://www.sciencedirect.com/science/article/pii/S0167844211001236.

[100] K. Ghosh, M. Hilal, and S. Bose, "Corrosion behavior of 2024 al-cu-mg alloy of various tempers," *Transactions of Nonferrous Metals Society of China*, vol. 23, no. 11, pp. 3215–3227, 2013, ISSN: 1003-6326. DOI: https://doi.org/10.1016/S1003-6326(13)62856-3. [Online]. Available: https://www.sciencedirect.com/science/article/pii/S1003632613628563.

[101] J. Li and J. Dang, "A summary of corrosion properties of al-rich solid solution and secondary phase particles in al alloys," *Metals*, vol. 7, no. 3, 2017, ISSN: 2075-4701. DOI: 10.3390/met7030084. [Online]. Available: https://www.mdpi.com/2075-4701/7/3/84.

[102] S. L. Rodríguez R., J. H. Díaz A., L. S. Hernández H., F. G. Pérez-Gutiérrez, A. P. Zhilyaev, J. Calvo, and J.-M. Cabrera, "Enhancement of pitting corrosion resistance for aa1050 processed by continuous closed die forging," *Journal of Materials Research and Technology*, vol. 9, no. 6, pp. 13 185–13 195, 2020, ISSN: 2238-7854. DOI: https://doi.org/10.1016/j.jmrt.2020.09.065. [Online]. Available: https://www.sciencedirect.com/science/article/pii/S2238785420317907.

[103] M.-L. de Bonfils-Lahovary, L. Laffont, and C. Blanc, "Characterization of intergranular corrosion defects in a 2024 t351 aluminium alloy," *Corrosion Science*, vol. 119, pp. 60–67, 2017, ISSN: 0010-938X. DOI: https://doi.org/10.1016/j.corsci.2017.02.020. [Online]. Available: https://www.sciencedirect.com/science/article/pii/S0010938X16311891.

[104] S. Bocchi, M. Cabrini, G. D'Urso, C. Giardini, S. Lorenzi, and T. Pastore, "Stress enhanced intergranular corrosion of friction stir welded aa2024-t3," *Engineering Failure Analysis*, vol. 111, p. 104 483, 2020, ISSN: 1350-6307. DOI: https://doi.org/10.1016/j.engfailanal.2020.104483. [Online]. Available: https://www.sciencedirect.com/science/article/pii/S1350630719304406.

[105] M. Cabrini, S. Bocchi, G. D'Urso, C. Giardini, S. Lorenzi, C. Testa, and T. Pastore, "Stress corrosion cracking of friction stir-welded aa-2024 t3 alloy," *Materials*, vol. 13, no. 11, 2020, ISSN: 1996-1944. DOI: 10.3390/ma13112610. [Online]. Available: https://www.mdpi.com/1996-1944/13/11/2610.

[106] W. Wang, T. Li, K. Wang, J. Cai, and K. Qiao, "Effect of travel speed on the stress corrosion behavior of friction stir welded 2024-t4 aluminum alloy," *Journal of Materials Engineering and Performance*, vol. 25, no. 5, pp. 1820–1828, May 2016, ISSN: 1544-1024. DOI: 10.1007/s11665-016-1979-6. [Online]. Available: https://doi.org/10.1007/s11665-016-1979-6.

[107] ASTM International, *ASTM G110-92(R2003), Standard Practice for Evaluating Intergranular Corrosion Resistance of Heat Treatable Aluminum Alloys by Immersion in Sodium Chloride+Hydrogen Peroxide Solution*, West Conshohocken, PA, 2003. [Online]. Available: http://www.astm.org/cgi-bin/resolver.cgi?G110.

[108] ——, *ASTM G34-01, Standard Test Method for Exfoliation Corrosion Susceptibility in 2XXX and 7XXX Series Aluminum Alloys (EXCO Test)*, West Conshohocken, PA, 2001. [Online]. Available: http://www.astm.org/cgi-bin/resolver.cgi?G34.

[109] S. Sinhmar and D. K. Dwivedi, "Art of friction stir welding to produce weld joint without rotation of shoulder with narrow heat-affected zone and high corrosion resistance," *Science and Technology of Welding and Joining*, vol. 25, no. 6, pp. 490–495, 2020. DOI: 10.1080/13621718.2020.1746512. [Online]. Available: https://doi.org/10.1080/13621718.2020.1746512.

[110] ASTM International, *ASTM G69-20, Standard Test Method for Measurement of Corrosion Potentials of Aluminum Alloys*, West Conshohocken, PA, 2020. [Online]. Available: http://www.astm.org/cgi-bin/resolver.cgi?G69.

[111] P. Petroyiannis, S. Pantelakis, and G. Haidemenopoulos, "Protective role of local al cladding against corrosion damage and hydrogen embrittlement of 2024 aluminum alloy specimens," *Theoretical and Applied Fracture Mechanics*, vol. 44, no. 1, pp. 70–81, 2005, ISSN: 0167-8442. DOI: https://doi.org/10.1016/j.tafmec.2005.05.006. [Online]. Available: https://www.sciencedirect.com/science/article/pii/S0167844205000455.

[112] R. Lakshmi, G. Yoganandan, K. Kavya, and B. J. Basu, "Effective corrosion inhibition performance of ce3+ doped sol–gel nanocomposite coating on aluminum alloy," *Progress in Organic Coatings*, vol. 76, no. 2, pp. 367–374, 2013, ISSN: 0300-9440. DOI: https://doi.org/10.1016/j.porgcoat.2012.10.004. [Online]. Available: https://www.sciencedirect.com/science/article/pii/S0300944012002652.

[113] Z. Li, Y. Yue, S. Ji, P. Chai, and Z. Zhou, "Joint features and mechanical properties of friction stir lap welded alclad 2024 aluminum alloy assisted by external stationary shoulder," English, *Materials and Design*, vol. 90, pp. 238–247, 2016, ISSN: 02641275. DOI: 10.1016/j.matdes.2015.10.056.

[114] Z. Dong, K. Yang, R. Ren, G. Wang, L. Wang, and Z. Lv, "Friction stir lap welding 0.8-mm-thick 2024 aluminum alloy with the assistance of stationary shoulder," English, *Journal of Materials Engineering and Performance*, vol. 28, no. 11, pp. 6704–6713, 2019, ISSN: 10599495. DOI: 10.1007/s11665-019-04395-3.

[115] E. Ghali, "Testing of aluminum, magnesium, and their alloys," in *Uhlig's Corrosion Handbook*. John Wiley & Sons, Ltd, 2011, ch. 81, pp. 1103–1106, ISBN: 9780470872864. DOI: https://doi.org/10.1002/9780470872864.ch81. [Online]. Available: https://onlinelibrary.wiley.com/doi/abs/10.1002/9780470872864.ch81.

[116] N. H. Holroyd, J. Evans, and G. M. Scamans, "Pre-exposure embrittlement of an al-cu-mg alloy, aa2024-t351," *Corrosion Reviews*, vol. 33, no. 6, pp. 361–372, 2015. DOI: doi:10.1515/corrrev-2015-0037. [Online]. Available: https://doi.org/10.1515/corrrev-2015-0037.

[117] X. Liu, G. Frankel, B. Zoofan, and S. Rokhlin, "In-situ observation of intergranular stress corrosion cracking in aa2024-t3 under constant load conditions," *Corrosion Science*, vol. 49, no. 1, pp. 139–148, 2007, Progress in Corrosion Research in Commemoration of Centenary of Birth of Professor Go Okamoto, ISSN: 0010-938X. DOI: https://doi.org/10.1016/j.corsci.2006.05.013. [Online]. Available: https://www.sciencedirect.com/science/article/pii/S0010938X06001272.

[118] ASTM International, *ASTM G31-72(2004), Standard Guide for Laboratory Immersion Corrosion Testing of Metals*, West Conshohocken, PA, 2004. [Online]. Available: http://www.astm.org/cgi-bin/resolver.cgi?G31.

[119] ——, *ASTM G46-94(2018), Standard Guide for Examination and Evaluation of Pitting Corrosion*, West Conshohocken, PA, 2018. [Online]. Available: http://www.astm.org/cgi-bin/resolver.cgi?G46.

[120] F. Mansfeld, "Electrochemical methods of corrosion testing," in *Corrosion: Fundamentals, Testing, and Protection*, S. D. Cramer and B. S. J. Covino, Eds., 1st ed. Materials Park, Ohio, USA: ASM International,

2003, vol. 13A, pp. 446–462, ISBN: 0-87170-705-5. [Online]. Available: https://www.asminternational.org/search/-/journal_content/56/10192/06494G/PUBLICATION.

[121] R. K. Franklin, "In vivo electrochemical sensors," Ph.D. dissertation, University of Michigan, Horace H. Rackham School of Graduate Studies, 2010. [Online]. Available: http://deepblue.lib.umich.edu/bitstream/2027.42/77688/1/rkfrankl_1.pdf.

[122] ASTM International, *ASTM G3-14(2019), Standard Practice for Conventions Applicable to Electrochemical Measurements in Corrosion Testing*, West Conshohocken, PA, 2019. [Online]. Available: http://www.astm.org/cgi-bin/resolver.cgi?G3.

[123] ——, *ASTM E8/E8M-22 Standard Test Methods for Tension Testing of Metallic Materials*, West Conshohocken, PA, 2022. [Online]. Available: http://www.astm.org/cgi-bin/resolver.cgi?E8.

[124] ——, *ASTM E407-07 (Reapproved 2015) Standard Practice for Microetching Metals and Alloys*, West Conshohocken, PA, 2015. [Online]. Available: http://www.astm.org/cgi-bin/resolver.cgi?E407.

[125] M. Janssen, J. Zuidema, and R. J. H. Wanhill, *Fracture mechanics*, Engels, 2nd ed. London: Spon Press, 2004, ISBN: 90-407-2221-8. DOI: 10.1201/9781482265583. [Online]. Available: https://doi.org/10.1201/9781482265583.

[126] R. Seetharaman, M. Seeman, D. Kanagarajan, P. Sivaraj, and I. Saravanan, "A statistical evaluation of the corrosion behaviour of friction stir welded aa2024 aluminium alloy," *Materials Today: Proceedings*, vol. 22, pp. 673–680, 2020, International Conference on Materials Engineering and Characterization 2019, ISSN: 2214-7853. DOI: https://doi.org/10.1016/j.matpr.2019.09.066. [Online]. Available: https://www.sciencedirect.com/science/article/pii/S2214785319333097.

[127] N. Birbilis and B. Hinton, "19 - corrosion and corrosion protection of aluminium," in *Fundamentals of Aluminium Metallurgy*, ser. Woodhead Publishing Series in Metals and Surface Engineering, R. Lumley, Ed., Woodhead Publishing, 2011, pp. 574–604, ISBN: 978-1-84569-654-2. DOI: https://doi.org/10.1533/9780857090256.2.574. [Online]. Available: https://www.sciencedirect.com/science/article/pii/B9781845696542500195.

A Appendices

A.1 Oxidation of aluminium in alkaline environment

The anodic oxidation (Ox) of aluminium and cathodic reduction (Red) of oxygen in aerated alkaline aqueous solutions is given by [96]:

$$Ox : Al + 2H_2O \rightarrow AlO_2^- + 4H^+ + 3e^- \tag{10}$$

$$Red : O_2 + 2H_2O + 4e^- \rightarrow 4OH^- \tag{11}$$

The reduction of hydrogen or dissolved oxygen in water depends on pH and kinetics, an overview of the possible reactions is given below [36], [96]:

$$\textit{pH<7 without } O_2\textit{:}\ 2H^+ + 2e^- \rightarrow H_2 \tag{12}$$

$$\textit{pH<7 with } O_2\textit{:}\ 4H^+ + 4e^- + O_2 \rightarrow 2H_2O \tag{13}$$

$$\textit{pH}\geq 7\textit{ without } O_2\textit{:}\ 2H_2O + 2e^- \rightarrow 2OH^- + H_2 \tag{14}$$

$$\textit{pH}\geq 7\textit{ with } O_2\textit{:}\ O_2 + 2H_2O + 4e^- \rightarrow 4OH^- \tag{15}$$

A.2 Dimensions of tensile test specimens

The dimensions of the produced sheet-type tensile test specimens and subsize tensile test specimens according to ASTM-E8/E8M are shown in Figure 46.

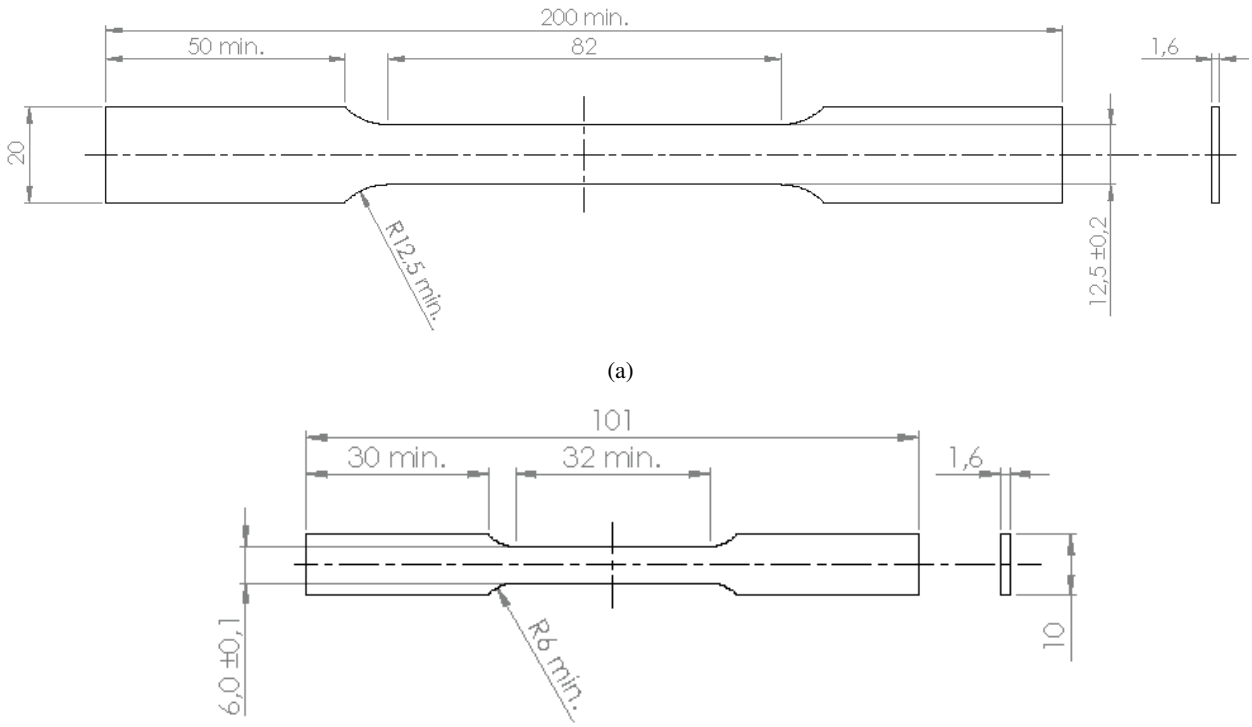

Figure 46: *Dimensions of rectangular tension test specimens according to ASTM-E8/E8M. The dimensions are presented in millimetres. Specimens produced from the 3.2 mm thick sheets have a thickness of 3.2 mm. (a) Sheet-type tension test specimen (for the welds). (b) Subsize tension test specimen (for BM only).*

A.3 Other surface roughness parameters

The complete set of surface roughness parameters of the uncorroded and corroded rectangular specimens are presented in Table 8. The surface roughness parameters include the arithmetic mean roughness (Sa), skewness (Ssk), area texture kurtosis (Sku), maximum peak height (Sp) and maximum valley depth (Sv). Sa is the average deviation from the mean surface, Ssk is the symmetry between peaks and valleys, Sku is the sharpness of the peaks and valleys, and Sp and Sv are the maximum positive and negative deviation from the mean surface, respectively.

All skewness values became lower after corrosion, indicating a shift towards more valleys than peaks (or deeper valleys than high peaks). A large decrease in skewness is observed in both the face and root surfaces of the 1.6 mm bare specimen: The Ssk value of the face decreases from 0.18 to 0.07, whereas the Ssk value of the root further decreases from -0.42 to -1.88. This decrease is attributed to the formation of pits on these surfaces, which is also evident in the large increase in maximum valley depth (Sv) for these surfaces. Overall, all surfaces showed a decrease in maximum peak height (Sp) and an increase in maximum valley depth (Sv) values after 24 hours of immersion in 3.5% NaCl solution.

WLI surface maps in Figure 34 show that the flash on both the RS and AS of the face of all specimens is much higher than the middle of the weld, which explains the corresponding large Sa and Sp values.

A.4 Spread of LPR data

The raw data obtained from the LPR measurements performed over 3 rounds on the HAZ on the RS of the 1.6 mm Alclad specimen is shown in Figure 47. The spread of the data can possibly explained by unstable open circuit potential, since the data are spread around three different potentials (about -420, -550, -700 mV/SCE). Furthermore, large differences in current density can be observed between rounds, which may be explained by phenomena occurring during testing: The green tape may have come loose during testing, exposing a larger surface and therefore increasing the current density and therefore lowering the polarisation resistance. Vice versa, hydrogen bubbles may have been trapped under the tape as well, blocking the exposed area from the test solution and thus increasing corrosion resistance (in this case of the solution, as mentioned by Vargel [36]). Either way, the resulting slopes (and thus resulting polarisation resistance) between the anodic and cathodic curves are vastly different between the rounds, which creates the large spread of the averaged data.

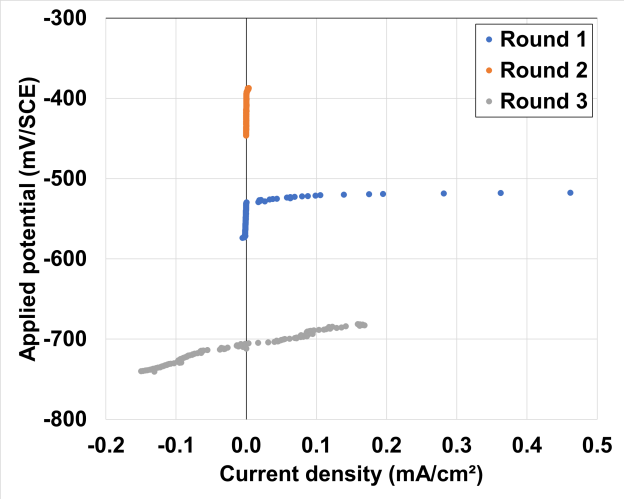

Figure 47: *Raw data of 3 rounds of LPR measurements performed on the HAZ on the RS of the 1.6 mm Alclad specimen.*